Radio Observations of PKS 2155−304 with the 100−m Effelsberg radio telescope

Bachelorarbeit

vorgelegt von
Tobias Beuchert

Erlangen Centre for Astroparticle Physics
Dr. Remeis Sternwarte Bamberg
Friedrich-Alexander-Universität
Erlangen-Nürnberg

1. Gutachter: Prof. Dr. Jörn Wilms
2. Gutachter: Prof. Dr. Ulrich Heber

Tag der Abgabe: 30. 07. 2010

Contents

1 Introduction to Active Galactic Nuclei

Abstract

"Astronomy makes use of more than 20 decades of the electromagnetic spectrum, from radio to gamma rays. The observing techniques vary so much over this enormous range that there are distinct disciplines of gamma-ray, X-ray, ultraviolett, optical, infrared, millimetre and radio astronomy. [Starting with the attempt of just listening to the space with simple earphones, modern] radio astronomy today takes account of the phase as well as the intensity of incoming radio waves, allowing the developement of interferometers of astonishingly high angular resolution and sensitivity." - (Burke & Graham-Smith, 2009)

1.1 General Characteristics including a brief history

AGN (Active Galactic Nuclei) has been a quite demanding task for a long time. It was always challenging to understand why these extragalactic sources are among the most luminous in universe, although the actual radiation source scales only with few parsecs. In comparison, the Andromeda galaxy has a diameter of $\approx 46\,\mathrm{kpc}$.
In addition, it was found that the emission that covers a huge range in frequency from Radio to gamma rays, is not powered by starlight.
In 1908 E.A. Fath measured strong emission lines from the Seyfert 2 galaxy NGC 1068.
Fath saw parallelisms to planetary nebulae concerning the spectral shape. However, Doppler broadening yielded velocities of several hundred km/s for the emitting source, which can not be explained by relatively steady nebulae. Later, in 1918, Curtis discovered a "curious straight ray" springing from M87 (Curtis, 1918). That was the first detection of a jet in the optical wavebands.
Two years earlier, the theory of general relativity was postulated by Einstein. This was the foundation for Hubble's postulation of some galaxies as extragalactic objects in 1926. Carl Seyfert discovered many spirals in 1943, whose optical "emission lines [are all] broadened, presumably by Doppler motion" with values up to 8500 km/s, and which have a highly luminous core region (Seyfert, 1943). So he introduced a new category of AGN, the so called "Seyfert Galaxies". 1955 one detected radio emission from NGC 1068 and NGC 1275 for the first time. Woltjer (1959) catched up all that knowledge and went further into detail. He claims a huge mass for the central 100 parsecs, if the high luminosity is linked to nuclear emission and a typical mass-to-light ratio holds. He also points out the high degree of doppler broadening of

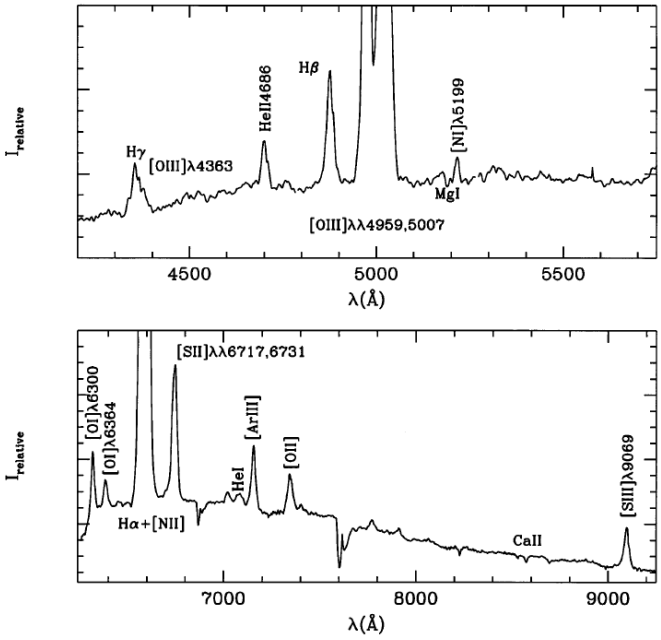

Figure 1.1: *Optical spectrum of NGC 1068, García-Lorenzo et al. (1999)*

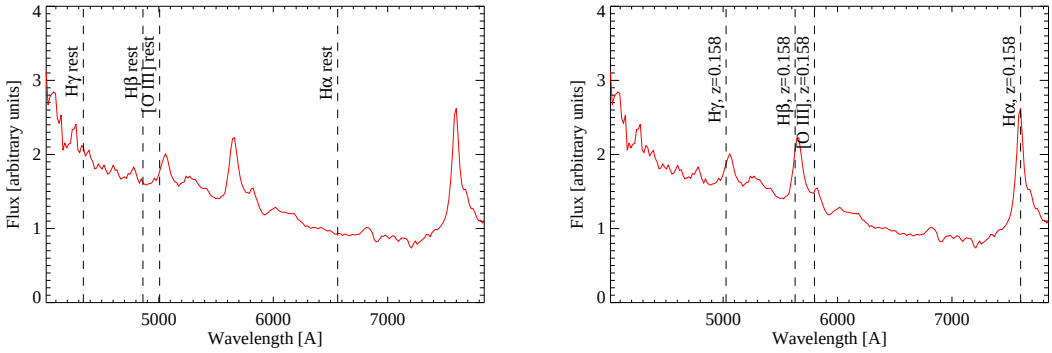

Figure 1.2: *Redshifted spectrum of 3C 273 (Wilms & Kadler, 2010)*

emission lines, but is not sure, if it is due to random or circular motions. A possible source of excitation seems to be a nucleus with a high dense accumulation of stars.
In the 1950's the first extended radio surveys were made. After mapping the position and extension of many strong radio emitting quasars, one tried to match them with other optical surveys. The only problem was that the position could not be measured with high accuracy because of the too wide telescope beams. So, matching these radio sources with the optical ones was also very difficult. Afterwards some more precise measurements were made, and Maarten Schmidt could measure the spectrum of 3C273 in 1962.

The results were quite breaking through, as the emission lines were uniformly redshifted.

Having the redshift z, one can evaluate the distance from Earth using

$$z = \frac{\lambda_{\mathrm{obs}} - \lambda_{\mathrm{em}}}{\lambda_{\mathrm{em}}} = \frac{\nu_{\mathrm{em}}}{\nu_{\mathrm{obs}}} - 1 \approx \frac{v}{c} \tag{1.1}$$

$$z + 1 = \frac{\nu_{\mathrm{em}}}{\nu_{\mathrm{obs}}} = \frac{1}{a(t)_{\mathrm{em}}} = \frac{R(t_0)}{R(t)}. \tag{1.2}$$

Here, $R(t) = D(t)/d$ is the scale factor, d the comoving distance, and $D(t)$ the proper distance between two observers in universe. For not too distant AGN, one can use Hubble's Law $v = H_0 D(t)$ with the Hubble constant H_0 to derive the proper distance between us and the emitting source. The Hubble constant is time dependent and linked with the redshift as $H = \dot{a} = \dot{R(t)}/R(t_0)$. As one now knows the discance to the extragalactic source and the apparent magnitude, m, use the distance modulus

$$m - M_{\mathrm{q}} = 5 \log D(t) - 5 \tag{1.3}$$

in order to yield the absolute magnitude M_{q}. For more distant AGN, one has to use the so called luminosity distance instead of the proper distance $D(t)$ from Hubble's law. Now one can compare the calculated absolute magnitude M_{q} with the solar one $M_{\odot}$ via

$$M_{\mathrm{q}} - M_{\odot} = -2.5 \log \frac{L_{\mathrm{q}}}{L_{\odot}} \tag{1.4}$$

and derive a overall luminosity of 3C 273 of $L_{\mathrm{q}} \approx 4.8 \cdot 10^{12}\, L_{\odot} \approx 1.84 \cdot 10^{46}\,\mathrm{erg/s}$ (≈ 50 times the luminosity of the brightest galaxy yet measured). This huge amount of luminosity originates just in the central region of an AGN (see Fig. 1.3 and Fig. 1.4).

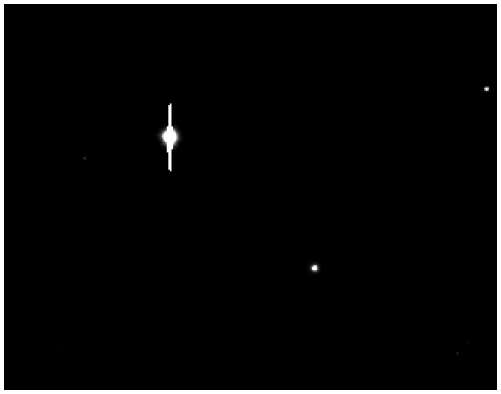

Figure 1.3: *NGC 3783, linear intensity scale (Wilms in private communication)*

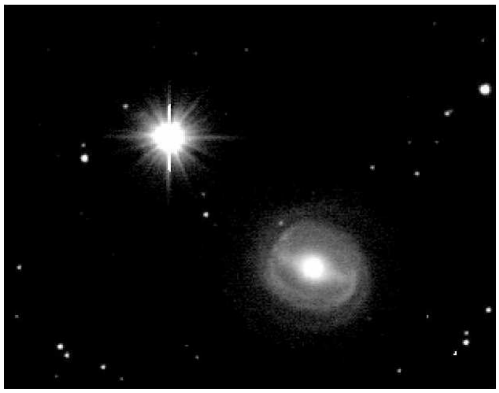

Figure 1.4: *NGC 3783, logarithmic intensity scale (Wilms in private communication)*

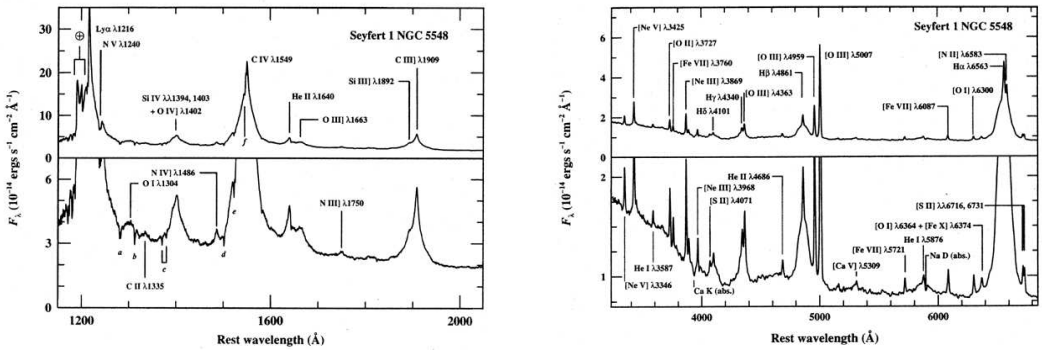

Figure 1.5: *Seyfert 1 (UV-) spectrum of NGC 5548 (Filippenko 1993, Korista 1993)*

1.2 Classification

1.2.1 Seyfert galaxies

The spiral galaxies Carl Seyfert detected show high redshifts and strong, broad emission lines due to many ionization stages, plus a highly luminous central region. These phenomenons are representative for so called active galaxies. In case of Seyfert galaxies, the so called host galaxies that contain the active nuclei, are all spirals.
Even though, these so called Seyfert galaxies are less luminous compared to the other types of AGN following later. Their absolute magnitude is limited by $M_b > -21.5 + 5 \log H_0$ (Peterson, 2009). There are two subclasses, namely Seyfert 1 and Seyfert 2 (Sy1, Sy2) types.
Seyfert 1 types show very broad emission lines from allowed transitions, and thin lines from forbidden ones (see Fig. 1.5).
For the allowed transitions, one finds velocities of $\approx 10^4\,\mathrm{km/s}$ due to the effect of Doppler line broadening. This is much faster than matter moving in our milky way. Rotation curves, also from other typical spiral galaxies, show velocities of just several hundred km/s. Additionally, narrow, forbidden lines are also characteristics for Sy 1 galaxies. These lines provide velocities of only several hundred km/s.
The broad allowed lines, furthermore, have to come from very dense regions, narrow forbidden lines on the other hand from less dense matter. This is because forbidden emission lines are due to very rarely multipole transitions with an Einstein coefficient of $A_{21} \sim 10\,\mathrm{s}^{-1}$ for spontaneous emission. These coefficients signify the number of transitions per time. One can only observe those forbidden lines in less dense medium, as in dense regions the "forbidden" excited states are collisional deexcited before photons can be emitted. Allowed lines in opposite occur mainly in dense regions, as their Einstein coefficients tend to be around $10^8\,\mathrm{s}^{-1}$. The overall electron density of the so called broad line region (BLR) is estimated to be $\approx 10^9\,\mathrm{cm}^{-3}$. The BLR is thought to be just a few parsecs away from the central supermassive black hole. The also occuring narrow forbidden lines from the narrow line region (NLR) represent electron densities of $\approx 10^3 - 10^6\,\mathrm{cm}^{-3}$. The NLR is, in opposite to the BLR, located in regions up to 10 pc away from the central region. So, because of the occurance of broad and nallow lines, the emission of these can not originate in the same region.
Seyfert 2 types on the other hand show permitted as well as forbidden lines, but both with a

line width according to $v \leq 10^3\,\mathrm{km/s}$, which means that both have to originate in the same region, namely the NLR. There are no broad lines. A typical Seyfert 2 spectrum is shown in Fig. 1.1. One can also see absorption lines due to the host galaxy. Introducing the unified model, which claims a dusty torus around the central black hole with its accretion disc, one can explain why Sy 1 and Sy 2 typed often blend into each other. This could be due to spatial seperated dense clouds in the torus, moving over the line of sight, causing a change of dense into less dense regions and vise versa (Goodrich, 1995).

1.2.2 Quasars

Quasars are the most luminious sources known. Their bolometric magnitude has to be $M_b < -21.5 + 5\log H_0$ (Peterson, 2009).
All sources that could not be identified with Seyfert galaxies in the 1950's radio survey of the Mullard Radio Astronomy Laboratory at Cambridge were classified as quasars first. The diameter of Seyfert galaxies varies between 2 and 8 arcmin. Quasars in comparison are more compact, and show diameters of less than 1 arcmin. That means that for the 1950's radio survey, these sources appeared to be point like, as the beam width of a typical not too large radio telescope in comparison is a few arcmins. So, a source of less than $1'$ in diameter, scanned by a beam of more than $1'$ in width, can not be resolved. In addition one has to consider that the diameter of 1' for quasars is due to optical observations. Radio (jet) structures and the active nuclei in the centre often have diameters of less than a few arcseconds.
So, it was quite challenging to find counterparts to these radio pointsources in existing optical sourveys, just because the source's position could not be determined precisely enough.
In order to do so, the 250 ft Lovell radio telescope at the Jodrell Bank Observatory (JBO) was adapted. They used the occultation of 3C 273 by the moon, whose position was well known. The diameter was determined to be around 6 arcseconds by analyzing at the fringe patterns of the source covered by the edge of the moon. Later, Rudolph Minkowski could identify 3C 273 with a galaxy. Maarten Schmidt was now able to take his famous redshifted spectra at Mount Palomar observatory, which clearly showed the extragalactic character of AGN.
Furthermore, two subclasses have been found: radioloud quasars (just called quasars) and radioquiet quasars (Quasi Stellar Objects, QSOs). The border between Sy1 types (see Sec. 1.2.1) and QSOs is not clear. One simple property to distinguish them is the higher luminosity of QSOs. Fig. 1.3 and Fig. 1.4 show that the term "quasi stellar object" is historically grown, as an AGN looks like a star under a linear intensity scale.

1.2.3 Blazars: BL Lacs and OVV's

BL Lacs are characterized through flat radio spectra due to their high compactness, as one will see later in Sec. 2.3. Their optical spectrum is featureless due to the extreme presence of a radio jet, whose radio emission overshines the entire spectrum from radio to UV. The continuum emission follows a powerlaw like $S_\nu \sim \nu^\alpha$. The radio emission has a high degree of linear polarization, which supports the conclusion of synchrotron emission being responsible for the measured radio flux. BL Lacs are in addition very variable due to relativistic beaming effects of the jet emission. In a fainter phase of the radio jet, some optical features occur in the

Table 1.1: *Classification (Wilms & Kadler, 2010)*

	optical emission lines	luminosity	radio (jets)	radio morphology
Sy1	broad + narrow	low	quiet	-
Sy2	narrow	low	quiet	-
radioquiet QSO	broad + narrow	high	quiet	-
QSO II	narrow only	high	quiet	-
BLRG, quasar	broad + narrow	low	loud	FR 1
(radioloud QSO)	broad + narrow	high	loud	FR 2
NLRG	narrow	low	loud	FR 1
	narrow	high	loud	FR 2
Blazars	-	high	loud	compact sources

spectra due to the hot corona above the accretion disc radiating thermally, and due to emission lines from excited disc regions. In this case, a BL Lac object could be classified as an optically violently variable quasar (OVV). OVVs lie on the border to quasars. Both BL Lacs and quasars are radioloud sources. The difference is that quasars also show optical features, as the line os sight allows a view on the central active region of an AGN. On the other side, BL Lacs are expected to occur, if the line of sight is pointed directly towards one jet. They got the name "quasar", because of the optical features, which are not seen in BL Lacs.
All in all, the covering name **blazar** is formed out of **BL** Lac and qu**azar**.

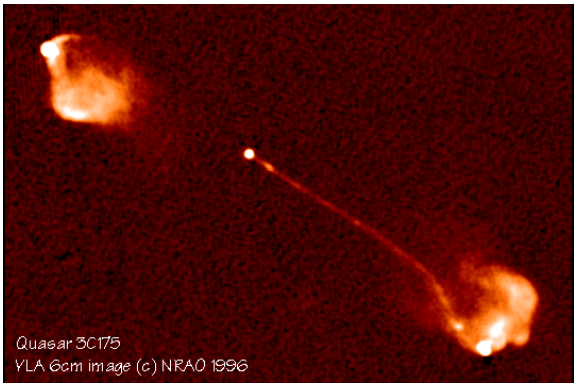

Figure 1.6: *FR II Type, Quasar 3C 175, VLA image at 6cm, (Bridle et al., 1994)*

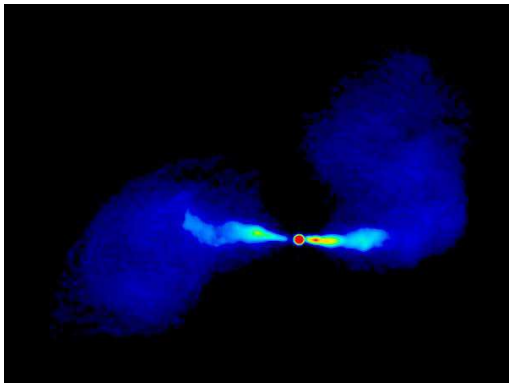

Figure 1.7: *FR I Type, 3C 271.1, M84, (Leahy, 2003)*

Tab. 1.1 shows the clear difference between radioloud and radioquiet sources. Thereby radioquiet does not mean that there are no radio features. They are just quite weak.
On the radioloud side one additionally finds Broad/Narrow Line Radio Galaxies (BLRG/NLRG). The classification is self-explanatory if one looks at their features. The radio loud types further split into Fanaroff Rilay (FR) types I and II (Fig. 1.6 and Fig. 1.7). FR II types have compact

radio lobes with so called hot spots at the outer end of a jet, where lots of energy is dissipated. The jet itself is quite collimated and thin. The counterjet is often not visible due to relativistic boosting (see Sec. 2.2.4). FR I types, however, have huge extended radio lobes. The highest amount of radiation comes from the central regions of the jets.
Anyway, the borders between all these different classes are not clear and vary from textbook to textbook. The unified model hence tries to refer all types to one model.

1.3 Unified Model

The unified model is a quite successful attempt to lead all the different types of AGN back to one model of an AGN, which is just observed from different lines of sight. Therefore one has to differ generally between radioquiet and radioloud AGN. Radioloud AGNs show strong influence by a radio jet, radioquiet ones do not. The basic model is shown in Fig. 1.8.

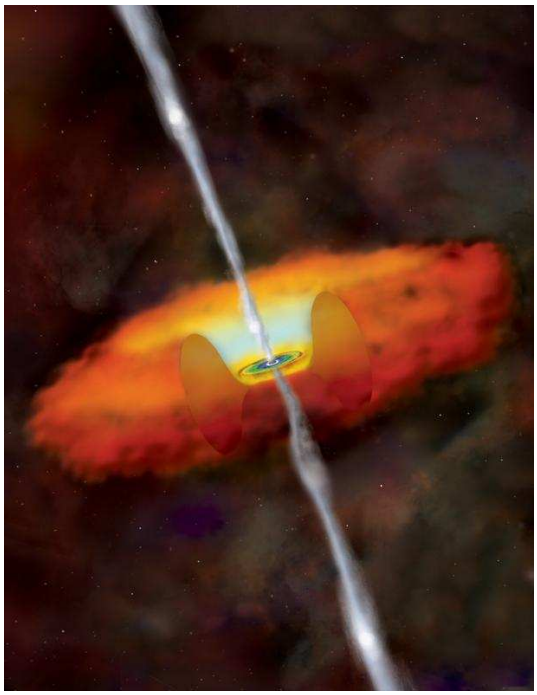

Figure 1.8: *Unified model for AGN*[1]

This model includes a supermassive black hole with masses around $10^6 - 10^7\,M_\odot$, surrounded by an accretion disc, which transports matter onto the black hole. Somehow one part of the matter is turned into energy, the other part is feeding the jet (see section 2.1). How the jet is formed is still object of research. King et al. (2005) show that an antiparallel spin of the accretion disc and the central black hole ("negative" spin of the black hole) as well as a parallel spin of both can form a stable system. After Dauser et al., 2010, "misaligned discs will evolve to one of them". Furthermore Reynolds et al. (2006) and Garofalo (2009) argue that radioloud jets might develop preferential in attendance of a configuration of antiparallel rotating accretion discs and black holes.
The accretion disc in turn is surrounded by a dusty torus. Now it depends from witch side one looks at this prototype of an AGN. Fig. 1.9 shows a sketch of a radioquiet AGN. In the very centre, the black hole is drawn as a black dot, surrounded by the accretion disc in direct vicinity, and further around the torus, drawn like an infinity sign. The small sized blobs signify the BLR in the environment up to $\sim 1\,\mathrm{pc}$ away from the black hole, the larger sized ones in contrast the NRL up to ~ 10 pc distance from the centre. Sy 1 types show broad and narrow lines from the BLR in vicinity of the black hole, where matter is naturally strong accumulated, and the less dense NLR farther away from the centre, respectively. The unified model for radioloud AGN is sketched in Fig. 1.10. Jets can be used synonymous for synchrotron radio emission due to accelerated electrons around the magnetic field lines of the jet. So, radioloud AGN types must have strong radio jets. A radio quiet quasar, or QSO in turn, is a quasar without strong radio jet features.
BL Lac objects, where the line of sight equals the jet direction towards the observer, appear very compact. Their IR to UV spectral features are overshadowed by radio emission.
The same difference in line widths as between Sy 1 and Sy 2, can also be found between Broad Line Radio Galaxies (BLRG) and Narrow Line Radio Galaxies (NLRG), respectively. The latter ones behave like the radio loud representatives of Seyfert galaxies.

[1] `http://www.obspm.fr/actual/nouvelle/jul04/nls1-f1.jpg`

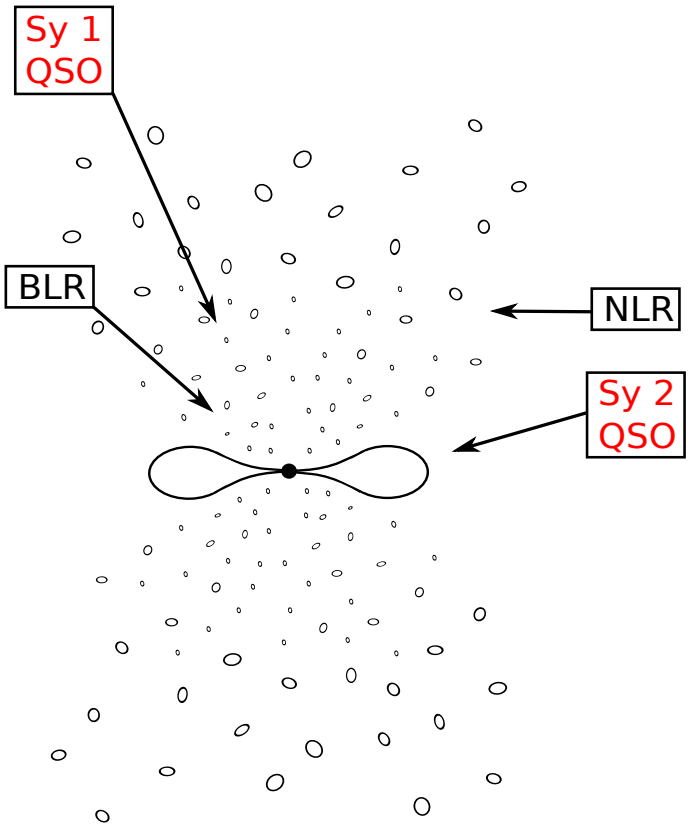

Figure 1.9: *Unified model for radioquiet AGN*

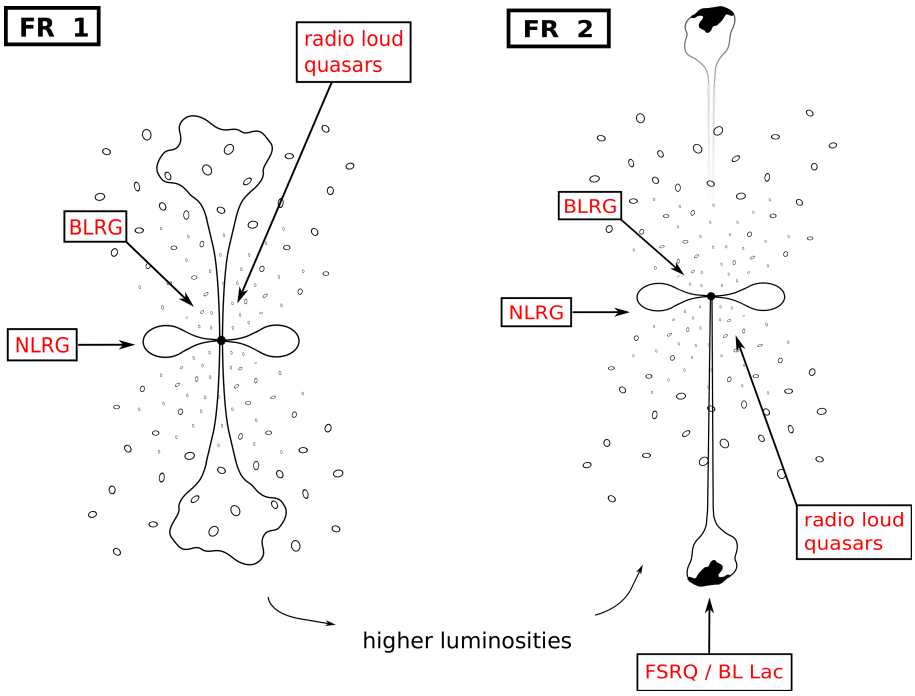

Figure 1.10: *Unified model for radioloud AGN*

2 AGN Physics

2.1 Energy Gain, Accretion Processes, Eddington Luminosity

The following section about accretion processes is based on Schneider (2007), Wilms & Kadler (2010) and Kembhavi & Narlika Jayant (1999), as well as to Przybilla & Drechsel (2009) and Rybicki (2004) concerning the details in radiation physics.
As we have seen in Sec. 1.1, the integrated luminosity of one AGN can easily exceed $10^{46}\,\mathrm{erg/s}$. One can calculate, how much mass has to be burned in order to yield these energies through nuclear fusion (Schneider 2007, Wilms & Kadler 2010).
Therefore, use Einstein's formula $E = \epsilon mc^2$ including an efficiency ϵ that states, which fraction of the available mass is turned into energy. One finds the according mass to be $m = E/\epsilon c^2$. Assume an integrated luminosity of $L = 10^{47}\,\mathrm{erg/s}$. The energy that will be dissipated after $10^7\,\mathrm{yr}$ can be calculated to be $E = 3.2 \cdot 10^{61}\,\mathrm{erg}$. This demands a mass of $m = 2.2 \cdot 10^9\,\mathrm{M}_\odot$ with an efficiency of $\epsilon_{\mathrm{Fusion}} = 0.008$. After a fration of ϵm has been turned into energy, the remainder, namely $(1-\epsilon)m$, will be left. The Schwarzschildradius of this mass is $r_\mathrm{s} = 2Gm/c^2 \approx 6.6 \cdot 10^{12}\,\mathrm{m}$. This, however, resembles approximately the diameters of the actual measured central region of AGN today. So, gravitation has to be very important, anyway. In addition, one yields an energy gain of $\approx 10^{20}\,\mathrm{erg/g}$ for a gravitational efficiency of $\epsilon \approx 0.1$ compared to just $\approx 7.2 \cdot 10^{18}\,\mathrm{erg/g}$ for nuclear fusion. So, accreting matter is the most efficient way of gaining energy in AGN (Schneider, 2007).
If one thinks about planets moving on Kepler orbits around the sun, the planets will not fall on the sun in foreseeable time. Stratificated accretion discs, however, have different layers rotating with different speeds around the central black hole. This is called differential rotation, which leads to a heating of the disc, and outwards loss of angular momentum. Now, matter can be accreted, although experiencing a resistance from the radiation, generated by the infalling matter, as we assume an optically thick disc. The virial theorem tells that half of the released gravitational energy will be turned into the amount of kinetic energy, the other half into internal energy. In formulae: $E_\mathrm{kin} = -E_\mathrm{pot}/2 = -\Delta E/2$ and $\Delta E - E_\mathrm{kin} = E_\mathrm{i}$, where

$$\Delta E = \frac{GM_\bullet m}{r} - \frac{GM_\bullet m}{r + \Delta r} \approx \frac{GM_\bullet m}{r^2}\Delta r \tag{2.1}$$

is the released potential energy due to the accretion of the mass m from the distance $r + \Delta r$ to r from the black hole.
The change in luminosity ΔL

$$\Delta L = \frac{GM_\bullet \dot{m}}{2r^2}\Delta r \tag{2.2}$$

is due to a gravitational energy gain of ΔE with an accretion rate of $\dot{m}$, assuming that the internal energy E_i is translated into thermal radiation (Wilms & Kadler, 2010). The condition for matter to be accreted is that the pressure gradient due to gravitation has to exceed the gradient due to radiation pressure:

$$\frac{dp_{\mathrm{grav}}}{dr} \overset{!}{>} \frac{dp_{\mathrm{rad}}}{dr} \tag{2.3}$$

This equation can be derived from the assumption of hydrostatic equilibrium, where a balance between pressure gradients due to inward gravitation and outward radiation is maintained (Przybilla & Drechsel, 2009):

$$g_{\mathrm{grav}} \rightarrow \frac{dp_{\mathrm{grav}}}{dr} = -g_{\mathrm{grav}}\rho = -G\frac{M_\bullet}{r^2}\rho \sim -G\frac{M_\bullet}{r^2}m_{\mathrm{H}} \tag{2.4}$$

$$g_{\mathrm{rad}} \rightarrow \frac{dp_{\mathrm{rad}}}{dr} = -g_{\mathrm{rad}}\rho = ? \tag{2.5}$$

The radiation pressure itself can be expressed via the second momentum of intensity $K_\nu = \frac{1}{2}\int_{-1}^{1} I_\nu(\mu)\mu^2 d\mu$ with $\mu = \cos\theta$ and a viewing angle of θ:

$$p_{rad} = \frac{4\pi}{c}K_\nu \tag{2.6}$$

Inserting the optical depth $\tau = -\int_{r_0}^{r} \kappa_\nu dr \Rightarrow d\tau = -\kappa_\nu dr$, where dr is the geometric depth pointing in opposite direction to the optical depth, one finds an expression for the Eddington flux H_ν:

$$\frac{dK_\nu}{d\tau} = H_\nu \tag{2.7}$$

Using $d\tau = -\kappa_\nu dr$ one finds

$$\frac{dp(\nu)_\nu}{d\tau} = \frac{4\pi}{c}H_\nu \tag{2.8}$$

$$\frac{dp(\nu)_\nu}{dr} = \frac{4\pi}{c}\kappa_\nu H_\nu \tag{2.9}$$

$$\frac{dp}{dr} = \frac{4\pi}{c}\int \kappa_\nu H_\nu \, d\nu \tag{2.10}$$

$$= \frac{4\pi}{c}\int \sigma_{\mathrm{T}} n_e H_\nu \, d\nu \tag{2.11}$$

$$= \frac{4\pi}{c}\sigma_{\mathrm{T}} n_e H. \tag{2.12}$$

We have decided the opacity $\kappa_\nu = \sigma_\nu n_e$ to be due to Thomson scattering (scattering of photons with electrons) with the Thomson cross section σ_{T}. The integrated Eddington flux corresponds

to a luminosity per surface $H = L/4\pi r^2$. The condition for bound matter was

$$\frac{dp_{\mathrm{grav}}}{dr} \overset{!}{>} \frac{dp_{\mathrm{rad}}}{dr} \tag{2.13}$$

$$G\frac{M_\bullet}{r^2} m_{\mathrm{H}} \overset{!}{>} \frac{4\pi}{c}\sigma_{\mathrm{T}} n_e \frac{L}{4\pi r^2} \tag{2.14}$$

$$L \overset{!}{<} L_{\mathrm{Edd}} = G\frac{M_\bullet c m_{\mathrm{H}}}{\sigma_{\mathrm{T}}}. \tag{2.15}$$

Inserting typical values, one finds an Eddington luminosity of $L_{\mathrm{Edd}} \approx 1.3 \cdot 10^{38}$ erg/s $\cdot \frac{M_\bullet}{M_\odot}$ (Robson, 1996).
For the maximal accretion rate due to the Eddington luminosity

$$L_{\mathrm{Edd}} = \eta \dot{M}_{\mathrm{Edd}} c^2 \tag{2.16}$$

one finds

$$\dot{M}_{\mathrm{Edd}} = \frac{L_{\mathrm{Edd}}}{\eta c^2} \approx 2\ M_\odot/\mathrm{yr} \tag{2.17}$$

with an efficiency η of ≥ 0.12 due to high optical depth as "resistance" for photons.
Using Equ. 2.2, and the Stefan Boltzmann law $\Delta L = 4\pi r \Delta r \sigma T^4$ assuming thermal black body radiation from the accretion disc due to its calculated change in luminosity ΔL (Schneider, 2007), one finds

$$T(r) = \left(\frac{\Delta L}{4\pi r^3 \sigma_{\mathrm{SB}}}\right)^{-1/4} = \left(\frac{G M_\bullet \dot{m}}{8\pi r^3 \sigma_{\mathrm{SB}}}\right)^{-1/4} \overset{r_s = 2GM_\bullet/c^2}{=} \left(\frac{c^6}{64\pi\sigma_{\mathrm{SB}} G^2}\right)^{1/4} \dot{m}^{1/4} M_\bullet^{-1/2} \left(\frac{r}{r_s}\right)^{-3/4}. \tag{2.18}$$

Futhermore, assuming the model of spatial thin accretion discs, one can neglect the radiation pressure as a balancing mechanism. In this case, the decisive counterbalance to the gravitational force is the pressure gradient of the disc. One can now use different assumptions regarding the vertical density in the disc, mass conservation, outward transport of angular momentum and at last optical thickness. The resulting final temperature profile (Krolik, 1999) is

$$T(r) = \left[\frac{3GM\dot{M}}{8\pi r^3 \sigma_{\mathrm{SB}}}\left(1 - \frac{{r_*}^{1/2}}{r}\right)\right]^{1/4}. \tag{2.19}$$

For both a spatial thick and thin disc, the resulting temperature behaves like $T(r) \sim r^{-3/4}$.

2.2 Radiative Processes

2.2.1 Synchrotron Radiation

The following explanations are refered to Kembhavi & Narlika Jayant (1999), Rybicki (2004), and Pankratov (2008).

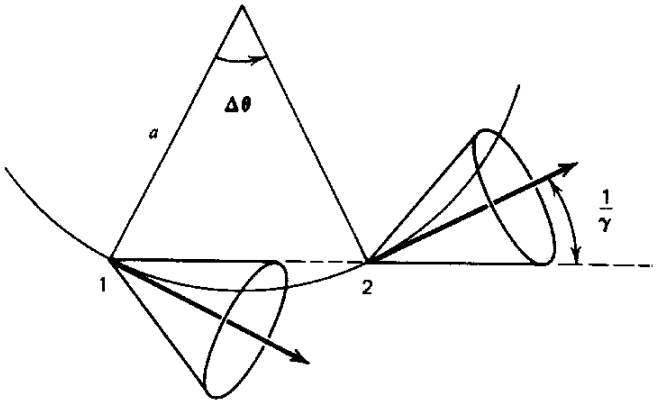

Figure 2.1: *Synchrotron emission from a circular accelerated electron, Rybicki (2004, Fig. 6.2)*

Accelerated electrons emit electromagnetic radiation with an intensity of

$$I = \frac{2}{3}\frac{e^2}{c^3}\dot{\mathbf{v}}^2. \tag{2.20}$$

First, imagine circular accelerated electrons. In the electrons frame of rest one finds radial symmetric emission, in the lab frame forward directed radiation in a cone with an opening angle of $1/\gamma$. Looking from the side on a circular accelerated electron, it seems just to move up and down, which explains the high degree of linear polarization. The whole emitted power is

$$I = \frac{dE}{dt} = \frac{2}{3}\frac{e^4}{m_\mathrm{e}^2 c^5}H^2\frac{v^2}{\left(1-\frac{v^2}{c^2}\right)}\dot{\mathbf{v}}^2 \;\Rightarrow\; I = \frac{4}{3}\sigma_\mathrm{T} c\gamma^2 U_\mathrm{mag} \tag{2.21}$$

(Pankratov, 2008). With the energy density $U_\mathrm{mag} = H^2/8\pi$ one can evaluate the cooling time

$$t = \frac{3}{2}\frac{m^4c^7}{e^4B^2E_0} \tag{2.22}$$

during which the energy decreases by factor 2. To be more realistic (Kembhavi & Narlika Jayant 1999, Rybicki 2004), helical trajectories of electrons around the jet's magnetic field have to be taken into account (Fig. 2.2). The intensity due to a pitch angle α can be calculated starting with the basic equation $I = \frac{2}{3}\frac{e^2}{c^3}\mathbf{a}^2$. Because of the helical trajectory, one has to divide the acceleration $\mathbf{a} = \sqrt{a_\perp^2 + a_\parallel^2}$ into a component perpendicular and parallel to the magnetic field. For relativistic particles, a transformation to the frame of rest K' is required, using

$$a_\perp^{'} = \gamma^2 a_\perp \text{ and } a_\parallel^{'} = \gamma^3 a_\parallel. \tag{2.23}$$

So, the total emitted power can be written as

$$I = \frac{2}{3}\frac{e^2}{c^3}\gamma^4\left(a_\perp^2 + \gamma^2 a_\parallel^2\right). \tag{2.24}$$

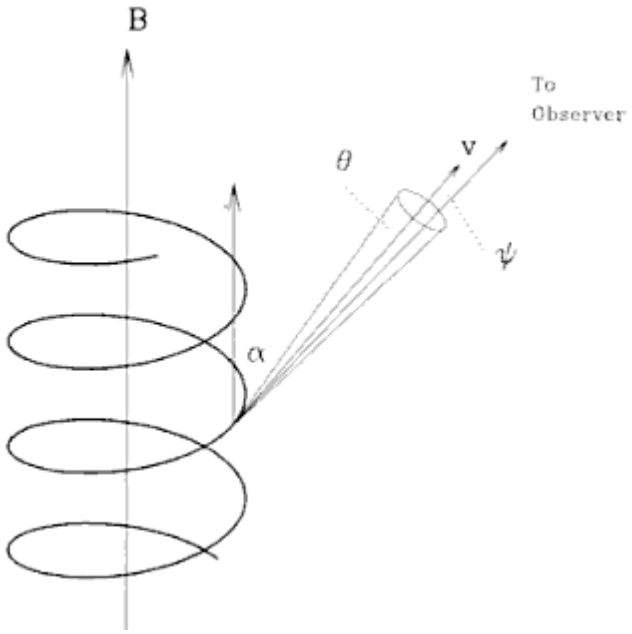

Figure 2.2: *Synchrotron emission from a electron on helical trajectories, Kembhavi & Narlika Jayant (1999, Fig. 3.1)*

The acceleration components can be expressed as $a_{\parallel} = 0$ and $a_{\perp} = 2\pi\nu_g v \sin\alpha$ with the gyration frequency $\nu_{\rm g} = \nu_{\rm cyc}/\gamma = eB/2\pi m\gamma c$. One finds the released energy per time to be

$$I = \frac{dE}{dt} = \frac{2}{3}\frac{e^4\gamma^2 H^2 v^2}{m^2c^5}(\sin\alpha)^2. \tag{2.25}$$

In the non relativistic case, electrons radiate with the cyclotron frequency only. After averaging over all pitch angles α one yields again $I = \frac{4}{3}\sigma_{\rm T} c\gamma^2 U_{\rm mag}$.
As the lightcone of synchrotron radiation flashes by an observer (Kembhavi & Narlika Jayant, 1999), its angular width is $\theta \sim \frac{1}{\gamma}$.
The time for one flash-by is found through Lorentz transformation from the accelerated to the lab system: $\delta t \sim 1/\gamma^3\nu_{\rm gyr}\sin\alpha$.
So, the spectrum is concentrated around a characteristic frequency $\nu_0 \sim \gamma^3\nu_{\rm gyr}\sin\alpha$.
Because of frequency broadening due to a distributing γ and pitch angle α, one yields a frequency spectrum of one electron with a maximum at a critical frequency $\nu_c \sim \nu_0$ of

$$I(\nu) = \sqrt{3}\frac{e^3 H\sin\alpha}{mc^2}F(x) \tag{2.26}$$

with $x = \nu_0/\nu_c$ and $F(x) = x\int_x^\infty K_{5/3}(\zeta)d\zeta$.
As the radiation has a strong degree of linear polarization, one has to differ between components $\parallel$ and $\perp$ to the magnetic fild. That involves another function $G(x) = x\int_x^\infty K_{2/3}(\zeta)d\zeta$.

Therewith the intensity can be written as

$$I_{\parallel,\perp}(\nu) = \frac{\sqrt{3}}{2}\frac{e^3 H \sin\alpha}{mc^2}\begin{cases} F(x)+G(x) \text{ for } \perp H \\ F(x)-G(x) \text{ for } \parallel H. \end{cases} \tag{2.27}$$

The degree of linear polarization (maximum degree of polarization for a $I_\perp$-component only) can be found via

$$\Pi(\nu) = \frac{I_\perp\ (\nu) - I_\parallel(\nu)}{I_\perp(\nu) + I_\parallel(\nu)} = \frac{G(x)}{F(x)}. \tag{2.28}$$

2.2.2 Compton Scattering

In detail (Kembhavi & Narlika Jayant 1999, Robson 1996, Wilms & Kadler 2010), Compton scattering is the excitation of an electron by a photon, which reradiates another photon itself like a dipol. This can be described by electrodynamics. At some point the electron adepts a recoil. If we assume the initial mean photon power to be $\langle S\rangle$, and the differential power of the reradiated photon per steradian $dP/d\Omega$, we can connect them with the differential cross section $d\sigma/d\Omega$ to

$$\frac{dP}{d\Omega} = \frac{d\sigma}{d\Omega}\langle S\rangle. \tag{2.29}$$

The **Klein Nishina formula** describes the differential cross section with

$$\frac{d\sigma}{d\Omega} = \frac{3}{16\pi}\sigma_T \left(\frac{E'}{E}\right)^2 \left(\frac{E}{E'} + \frac{E'}{E} - (\sin\theta)^2\right), \tag{2.30}$$

which indicates the "Klein Nishina regime". If there is no recoil of the electron, and if $E'/E \approx 1$, the photons will do Thomson scattering. As the scattering occurs in the electron's frame of rest, one has to adapt a Lorentz transform into this system and back:

$$E_{\text{Lab}}^{\text{scattered}} = \gamma^2 E_{\text{Lab}}. \tag{2.31}$$

Thus, Compton scattering is a very efficient way of transfering energy for relativistic electrons. If the electron is at rest initially, the common Compton formulae are valid:

$$\lambda' - \lambda = \frac{h}{m_e c}(1-\cos\theta) \tag{2.32}$$

$$E_e' = \frac{E}{1+\frac{E}{m_e c^2}(1-\cos\theta)} \tag{2.33}$$

$$\frac{\Delta E}{E} \approx -\frac{E}{m_e c^2} \quad (E \ll m_e c^2) \tag{2.34}$$

For many scattering events, one finds

$$I = \frac{dE}{dt} = \frac{4}{3}\sigma_{\text{T}} c \gamma^2 U_{\text{rad}} \tag{2.35}$$

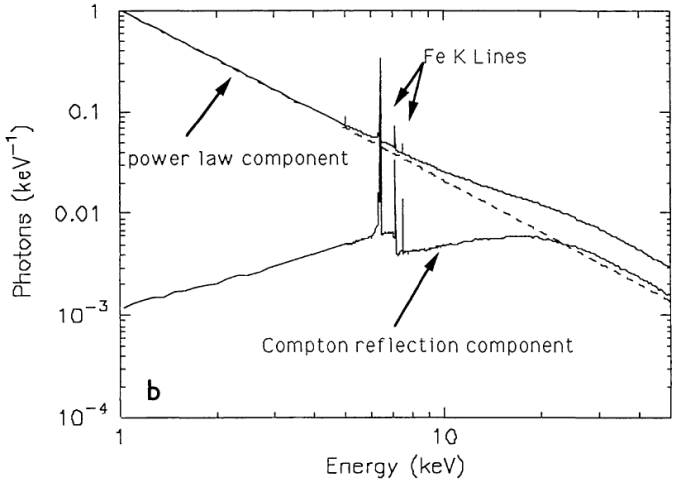

Figure 2.3: *Theoretical X-ray spectrum, (George & Fabian, 1991) and (Mushotzky et al., 1993)*

with the energy density of the radiation field $U_{\rm rad}$.
If the electron is not at rest initially, one defines an amplification factor with $\Delta E/E \approx -E/m_e c^2$ or

$$\frac{\Delta E}{E} = \frac{4kT_e - E}{m_e c^2} = A \tag{2.36}$$

and concludes:
if $E \lesssim 4kT_e$ (**inverse Compton scattering**), energy will be transfered from electrons to photons, and the electon-gas cools down.
In the opposite case (**Compton scattering**) with $E \gtrsim 4kT_e$, energy is transfered from photons to electrons. The electon-gas heats up. By now, only one electron was treated. For an accumulation of them, the photons are scattering multiple times. Hence, the final energy is $E_{\rm end} = E_{\rm init} A^k$ after k scattering events. The resulting photon rate at the energy E_k will in turn be $N(E_{\rm end}) \sim N(E_{\rm initial})(1+A)^k \sim N(E_{\rm initial})\,(E_{\rm end}/E_{\rm initial})^{-\alpha}$, which corresponds to a powerlaw. Fig. 2.3 shows a typical X-ray spectrum that results from this equation, but also showing some more effects. The slope at lower frequencies for example is due to absorption of the radiation on its way to Earth, especially while going through the accretion disc. The so called Compton reflection hump derives from X-rays passing accretion disc again. There, hydrogen and helium are fully ionized, which also leads to Thomson scattering of the X-ray and gamma-rays out of line of sight. Another reason for the hump is the photoionization of heavy elements and Compton downscattering of X-ray photons. The iron line is a very important feature, proving the presence of heavier, only partially ionized elements in the accretion flow. The shape of this line tells something about many issues concerning general relativistics and black hole physics.

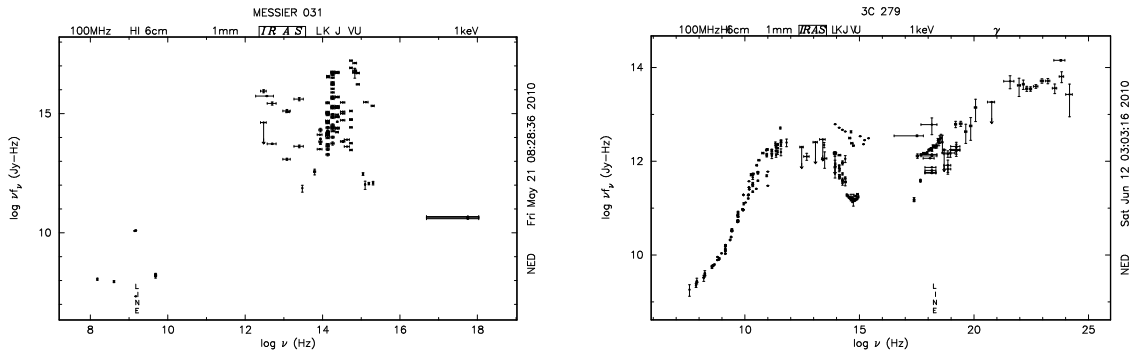

Figure 2.4: *Comparison between the SEDs of Andromeda, M31 and the QSO type 3C 279* [2]

2.2.3 The SED

The Spectral Energy Distribution (SED) of AGN equals an frequency spectrum, which is spread over the entire electromagnetic spectrum from the radio over infrared, optical and ultraviolett to X-ray and gamma wavebands. The SED of 3C 279 stretches from the radio to gamma wavebands, while the one from M 31 just covers IR to UV bands. Measuring one source simultaneously in all wavebands requires lots of international effords. However, this is very crucial, as these sources are mostly highly variable. 3C 279 thereby is one of the best studied and measured AGN.
Besides the more concentrated SED in case of M 31, which is due to thermal emission from stars and dust, 3C 279 does mainly exhibit non thermal synchrotron and inverse Compton emission from the jet. The line of sight, however, also admits a view onto the hot corona above the disc and the warm dust of the host galaxy, which causes thermal emission. The more a jet is pointed towards us, the more it is overshining this thermal emission with radio to gamma emission from synchrotron and inverse Compton mechanisms.
Furthermore, the integrated luminosity from the entire Andromeda galaxy M 31, which has a maximal diameter of 43 kpc, is just $\approx 10^{44}$ erg/s, whereas typical AGN exhibit luminosities around $\approx 10^{42} - 10^{48}$ erg/s from a region that covers just a few parsecs. Another source, whose SED shows perfect coverage of all wavebands is 3C 273 (Fig. 2.5). The underlying data is derived from 30 years of multi-wavelength observations of 3C 273 (Türler et al., 1999). This QSO shows even stronger thermal features in the SED compared to 3C 279, which is manifested in the double humped structure in the νF_ν-plot from IR to UV frequencies. The slopes on the left and right side, again correspond to radio synchrotron jet emission, and to inverse Compton emission, respectively.
In typical blazar SEDs, the underlying host galaxy do not contribute much compared to the strong jet emission. To give an example, Fig. 2.6 shows many average blazar SEDs (Donato et al., 2001). PKS 2155−304, the actual source of this thesis, is one of those blazars. Aharonian et al. (2009) published a SED for this source, covering the X-ray (*Chandra*) to gamma (H.E.S.S.) over the optical bands (Fig. 2.7).

[2] `http://nedwww.ipac.caltech.edu/`

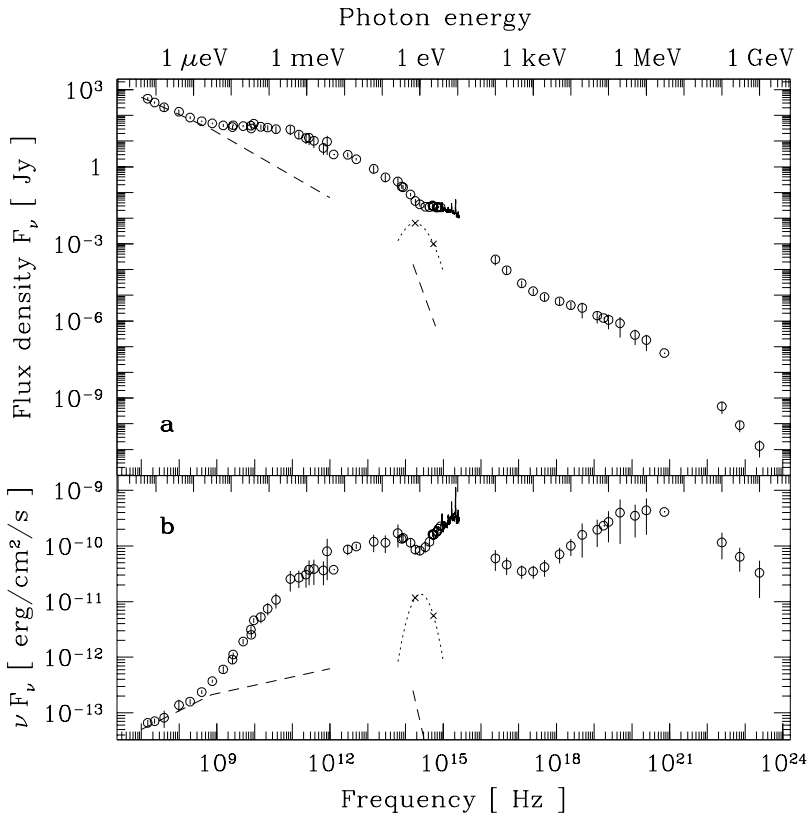

Figure 2.5: *SED of 3C 273: **(a)** F_ν, **(b)** νF_ν plot; the dashed line is the contribution from the jet (3C273A), the parabola corresponds to the thermal emission from the host galaxy (dotted line), (Türler et al., 1999)*

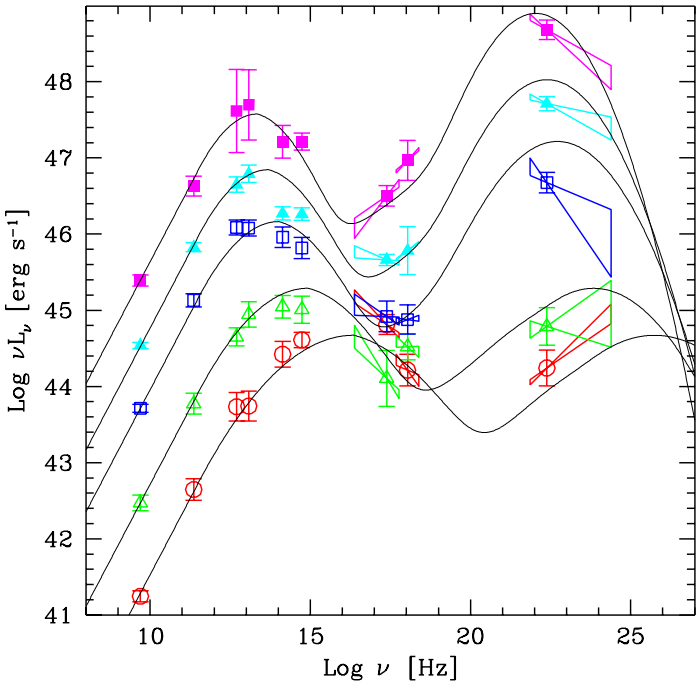

Figure 2.6: *Average SEDs from many blazars (Fossati et al. 1998, Donato et al. 2001); the solid lines correspond to a one–parameter-model fit to the data*

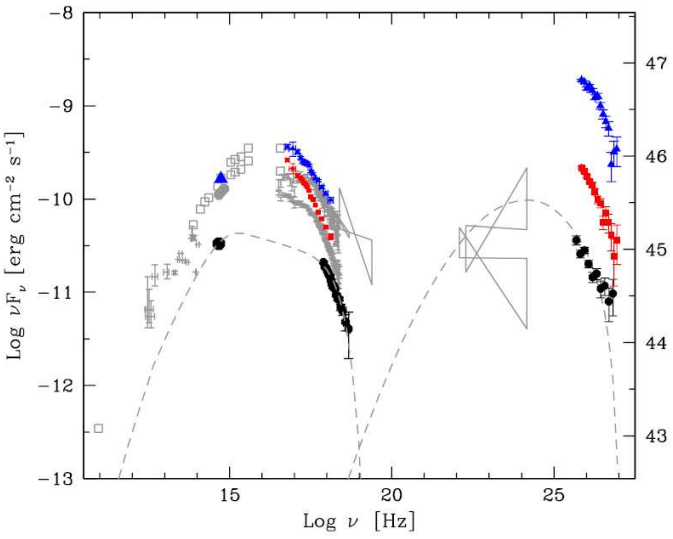

Figure 2.7: *Multifrequency campaign by the H.E.S.S. collaboration, observing the γ-ray flare of PKS 2155−304 in July 2006. Gaining this SED, a wide range in wave bands was covered, starting with X-ray (Chandra, RXTE) over optical data (Bronberg Obs.) to gamma (H.E.S.S.). The gray data points are historic ones. The highest state of the SED is labeled with blue triangles, the lowest state with red squares. The black circles correspond to a 2003 multiwavelength campaign (Aharonian et al., 2009)*

2.2.4 Relativistic Boosting

For many quasars, only one jet, but two radio lobes are observed (see Fig. 1.6). But there does exist a jet on the opposed side, which is just not observable due to the effect of relativistic beaming. The *classical* Doppler factor (Rybicki 2004) is

$$\mathcal{D} = \frac{1}{1 - \frac{v}{c}\cos\theta}. \tag{2.37}$$

which can be derived from assuming emission of light from two spatial separated points. It describes the change in frequency between the frame of rest and the laboratory frame with

$$\nu_{\mathrm{obs}} = \mathcal{D}\nu_{\mathrm{em}} = \frac{\nu_{\mathrm{em}}}{1 - \frac{v}{c}\cos\theta}. \tag{2.38}$$

As the particles in a jet are accelerated to highly relativistical speeds, one has to take time dilatation into account: $\Delta t_{\mathrm{obs}} = \gamma \Delta t_{\mathrm{em}}$ with $\gamma = 1/\sqrt{1-(v/c)^2} > 1$. Using $\nu \sim 1/\Delta t$ one finds that in addition to the Doppler factor $\mathcal{D}$, the relativistic factor γ has to be taken into account:

$$\nu_{\mathrm{obs}} = \frac{\nu_{\mathrm{em}}}{\gamma(1 - \frac{v}{c}\cos\theta)}. \tag{2.39}$$

Hence, the *relativistic* Doppler factor is

$$\mathcal{D} = \frac{1}{\gamma(1 - \frac{v}{c}\cos\theta)} = \frac{\sqrt{1-\beta^2}}{1 - \beta\cos\theta}. \tag{2.40}$$

If one plots $\mathcal{D}$ against the angle θ (Fig. 2.8), one finds a strong dependence of $\mathcal{D}$ at lower viewing angles between the jet and the line of sight. Furthermore, one can prove that $I_\nu^{\mathrm{obs}}/\nu_{\mathrm{obs}}^3 =$

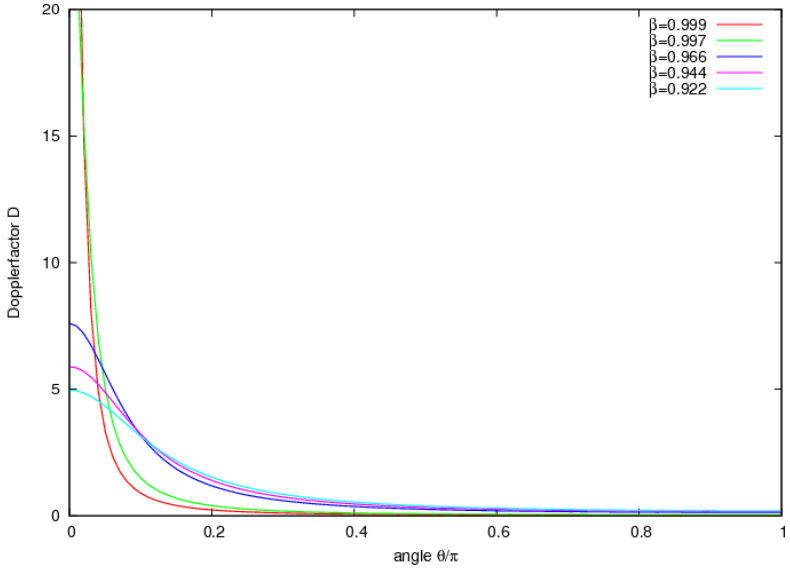

Figure 2.8: *The relativistic Doppler factor for different β in dependence of the viewing angle θ. The highest values are achieved towards smallest viewing angles.*

$I_\nu^{\mathrm{em}}/\nu_{\mathrm{em}}^3$ (Rybicki, 2004). Using Equ. 2.38, one can express the relationship between the observed and emitted intensity to be $I_\nu^{\mathrm{obs}} = \mathcal{D}^3 I_\nu^{\mathrm{em}}$. Additionally assuming a powerlaw $I_\nu \sim A\nu^\alpha$, this yields $I_\nu^{\mathrm{obs}} = \mathcal{D}^{3-\alpha} I_\nu^{\mathrm{em}}$.
For two blobs, one on the jet-, and one on the counterjet-side (Fig. 2.9), the ratio of the emitted intensities can be expressed via

$$\frac{I_1}{I_2} = \left(\frac{1+\beta\cos\theta}{1-\beta\cos\theta}\right)^{3-\alpha}. \tag{2.41}$$

This leads to the so called "jet one sideness".

2.3 Jet Modelling

This section will treat the origin and behaviour of the observed (radio) lightcurves and spectras of AGN.
Blandford & Konigl (1979) designed the first model of relativistic jets, the "blob in jet" model, giving answers on the basic processes in them. They claim an outer jet, in which a steady flow takes place. Inside this outer jet, dense clouds can be formed being in pressure equilibrium with it. These "blobs" are accelerated by the jet flow, and expand adiabatically on their way down the jet. These rapidly moving knots can be tracked with Very Large Baseline Interferometry (VLBI), giving a clue on their velocity, their formation, and growth. For the observed radio flux through synchrotron emission, one needs persistent acceleration of the electrons in the jet, which are distributed by an energy powerlaw. This can be explaned by shock waves propagating

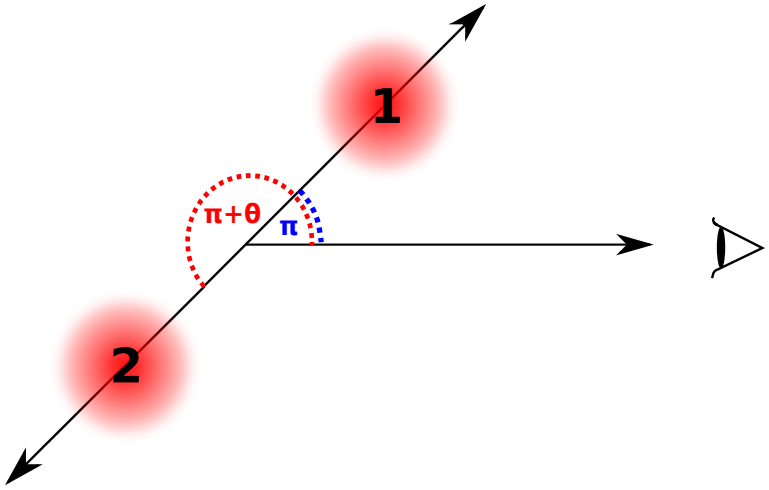

Figure 2.9: *Two jet components or blobs are moving with an angle θ towards the line of sight while emitting the intensities I_1 and I_2*

onto such a bunch of electrons, which was ejected into the jet at some time. So, these shocks are thought to be formed behind the dense clouds that are accelerated by the steady jet flow. Marscher & Gear (1985) built on the model of Blandford & Königl. Explaining the flares, or maxima in flux density in lightcurves, they talk more about shock waves than dense clouds that are formed in the base of the jet and move downwards a conical jet with small opening angle ("shock-in-jet model").
The electrons needed to do synchrotron emission are ejected at irregular time-intervals in the jet with an energy distribution $N(E) \sim N_0 E^{-s}$ for each bunch of those. This distribution yields the typical frequency specrum for synchrotron radiation (Equ. 2.26). The authors suggest the shocks to be engendered by a variating injection of electrons into the jet. If there were no variations but a steady ongoing injection, these electrons would flow outside continuously. With those variations, however, pressure fluctuations of the electron plasma – the shocks – can be created. Electrons crossing such a shock can be highly accelerated, which is the basic requirement for synchrotron and inverse Compton energy losses of the electrons. The acceleration is thought to take place behind the shock front (Marscher, 1996), where one finds electrons at different velocities. Therefore they radiate at different frequencies through synchrotron emission. Marscher & Gear also give a first hint on how radio spectras evolve with the lifetime of a shock propagating in an adiabatic, conical and relativistic jet. They name three stages of evolution. In the first stage, which corresponds to a growth state of a shock (Valtaoja et al., 1992), inverse Compton losses dominate the enery loss of the recently injected electrons. With time, electrons begin to loose their energy more and more through synchrotron radiation, which causes the measured radio flux. So, remembering the first hump in blazar SEDs to be due to synchrotron emission, the synchrotron peak flux will increase during the growing state of a shock.
Later, the synchrotron peak flux remains nearly constant. This is the second stage, where synchrotron losses of the electrons dominate. Following Valtaoja et al. (1992), this stage will be named the "plateau stage", where energy gain and loss are approximately balanced.
The third and last stage in the evolution of a shock is dominated by "adiabatic" losses, as Marscher & Gear call it. Actually the whole jet is adiabatic at all times. What is meant, is

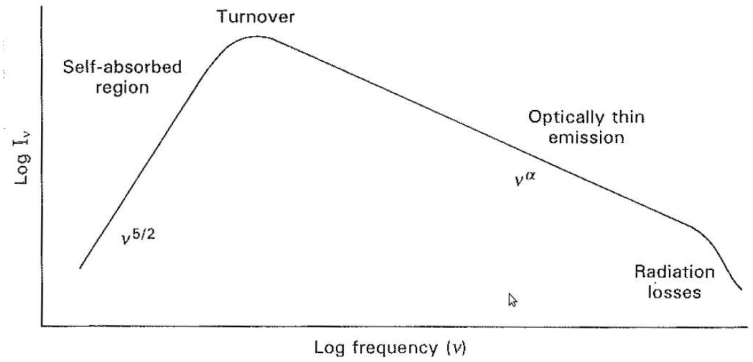

Figure 2.10: *synchrotron spectrum of a powerlaw energy distribution (Robson, 1996)*

the energy loss due to the final expansion and diminishing of the shock. There, synchrotron emission gets more and more unimportant, as the order of the B-field lines diminish.
Overall this is a model of an accelerated jet (Marscher, 1996). There are also decelerated models, which are less supported, though. One argument is exposed by Celotti & Fabian (1993): if a jet was decelerated, there would not be enough energy left to explain the bright radiolobes in FR II radio galaxies - sometimes hundrets of kiloparsecs away from the central engine. Finally Valtaoja et al. (1992) designed the "generalized shock model". It builds up the jet theory by Marscher & Gear (1985), which fails in claiming too steep optically thin synchrotron spectra. The most difficult thing is to model the early evolutionary stages. Now, again imagine one shock or "blob" moving down the jet. This corresponds to one bunch of electrons following a powerlaw energy distribution $N(E) \sim N_0 E^{-s}$, which causes one simple synchrotron specrum as shown in Fig. 2.10: as the shock propagates in the jet, the synchrotron peak flux at the turnover frequency moves towards lower frequencies. This is because the shock - or blob - expands while moving in the jet. If the plasma density decreases, less electrons can absorb their own radiated sychrotron photons. As this synchrotron self absorption only occurs at lower frequencies, the synchrotron peak will shift to lower frequencies. The medium thus gets optically thinner towards lower frequencies. This phenomenon can be best understood in Fig. 2.11.
The amount of flux will also change with time and frequency. In the growth stage, the radio synchrotron flux increases as the shock component emerges, which is gradually feeded with electrons from accretion processes. After that, the flux will remain nearly constant due to the shock moving downwards the jet, which is steadily emitting synchrotron radiation. Thereby is has to be emphasized again that the acceleration of the electron plasma - taking leptonic jets into account - has to take place inside the jet, namely behind the according propagating shock fronts. In the last stage, the decaying stage, the flux decreases due to a diminishing shock and thereby less accelerated electrons. These three stages of different energy losses can also be described by the flux they produce:

$$\begin{aligned} \text{growth stage } S_m &\sim \nu_m^a \\ \text{plateau stage } S_m &\sim \text{const} \\ \text{decaying stage } S_m &\sim \nu_m^b \end{aligned}$$

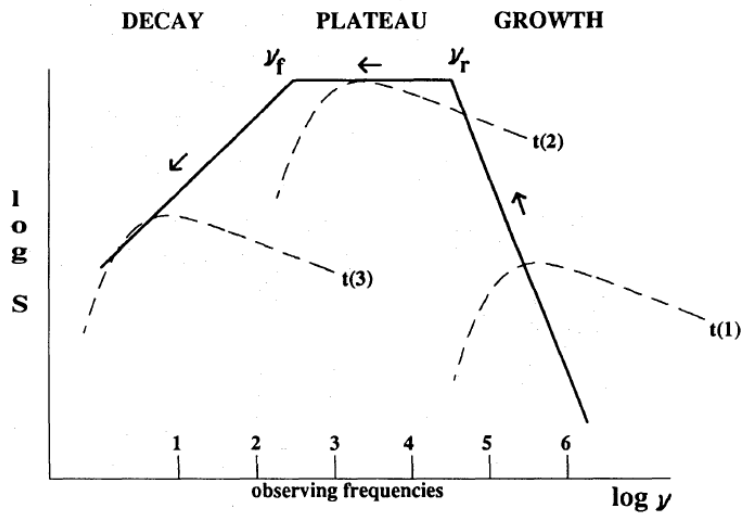

Figure 2.11: *Generalzed Shock Model (Valtaoja et al., 1992)*

Table 2.1: *summary of the generalized shock model*

high peaking flare	$\nu_{\rm obs} < \nu_{\rm f}$	steep radio spectra
low peaking flare	$\nu_{\rm obs} > \nu_{\rm f}$	flat radio spectra
intermediate flares	$\nu_{\rm f} < \nu_{\rm obs} < \nu_{\rm r}$	both flat and steep radio spectra

Additionally there is a classification of more or less energetic flares (see Fig. 2.11). If the observed frequency is smaller than the turnover frequency from the plateau stage to the decaying stage ($\nu_{\rm obs} < \nu_{\rm f}$), or in other words, if the flare reaches its maximum developement - the plateau stage - at frequencies higher than $\nu_{\rm obs}$, the flare is called a *high peaking flare*. If on the other hand $\nu_{\rm obs} > \nu_{\rm f}$, it is called a *low peaking flare*. With these terms, it can be expressed, whether a flare is just developing, or already diminishing.
So, if one observes at some frequencies below $\nu_{\rm f}$, this in turn means that the flare has already been in his stage of maximal development (plateau stage), and is now diminishing. A *low peaking flare* on the other side, is still growing, as one observes it at frequencies higher than the turnover to the decaying stage $\nu_{\rm f}$ (Tab. 2.1).
In one jet there can be found shocks at many different of these stages of development. So the actual measured spectrum consists of a superposition of many synchrotron spectra as seen in Fig. 2.10 at different turnover frequencies (ν_m). A superposition of several individual synchrotron spectra due to several shocks passing through the plateau phase, will lead to a flat radio spectrum.
As the flare develops and expands adiabatically, the flare is in the decaying stage, and the emerging radio spectra steepen. These steeper spectra are thought again by the superposition of many individual synchrotron spectra along the line due to the decaying stage in Fig. 2.11. The optical thin part of the superposed spectrum will show some negative slope.
Marscher (1996) emphasizes the importance of the inner jet region for the non-thermal emission and the flat radio spectra (Fig. 2.12). The inner jet region is assumed to be the region,

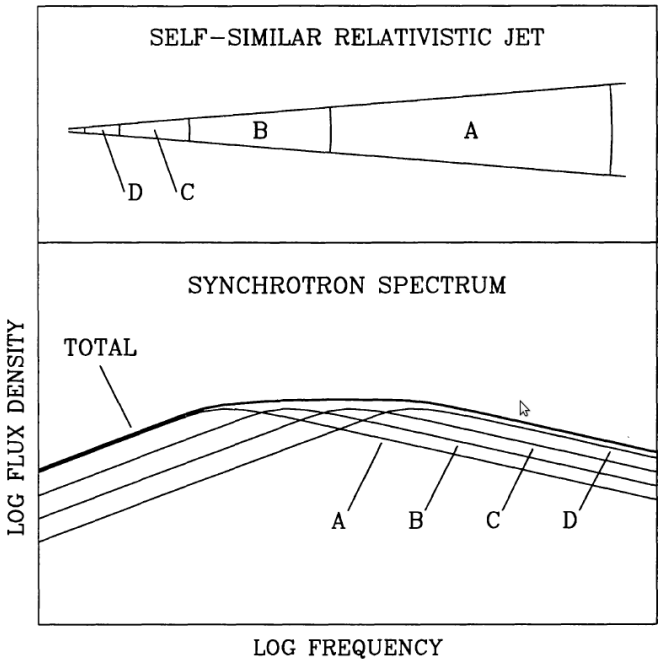

Figure 2.12: *superposition of the synchrotron radio emission of different propagating shocks (Marscher, 1996)*

where the jet is formed and accelerated. High opacities at the foot point of the inner jet and lower opacities further downstream lead to a higher synchrotron self absorption for lower frequencies at the denser regions. This process is also shown in Fig. 2.14 for emitting blobs at different evolutionary stages in the inner jet, and was described above as the generalized shock model.
The inner jet is more precisely defined by Marscher (2006b) as the part "between the injection point near the black hole and the most upstream feature in the radio jet - the core". The core is defined as the emerging- or foot-point of new jet components, or the point, where matter gets first optically thin and thus visible in the appropriate observed frequency.

Fig. 2.13 shows a sketch of an accelerated jet model. The electron plasma is thought to be accelerated just behing the propagating shock. Near the origin of the jet, where the BLR is located, the SSC effect mainly leads to X-ray emission. Farther down the jet, leaving the BLR, the remaining electrons do synchrotron emission.

This is now a good explanation of the flat radio spectra of compact sources, especially blazars, where one images shocks in different plateau stages at radio frequencies. At quasars, one can see the jets from the side under a quite sharp angle. Hence, one can look directly on different shocks propagating in the inner jet towards the observer. These are also getting optically thin at different frequencies at one time, as there are several shocks at different evolutionary stages. A really good example for that is the source 3C 111, monitored with the Very Long Baseline Array (VLBA) within the MOJAVE 2 cm survey over 18 epochs by Kadler et al. (2008). The radio lightcurves shown in Fig. 2.15 are measured with the University of Michigan Radio As-

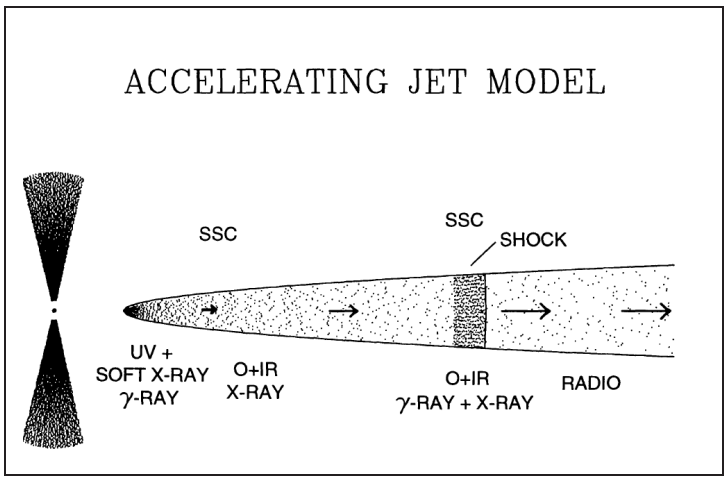

Figure 2.13: *model of an accelerated jet (Marscher, 1996)*

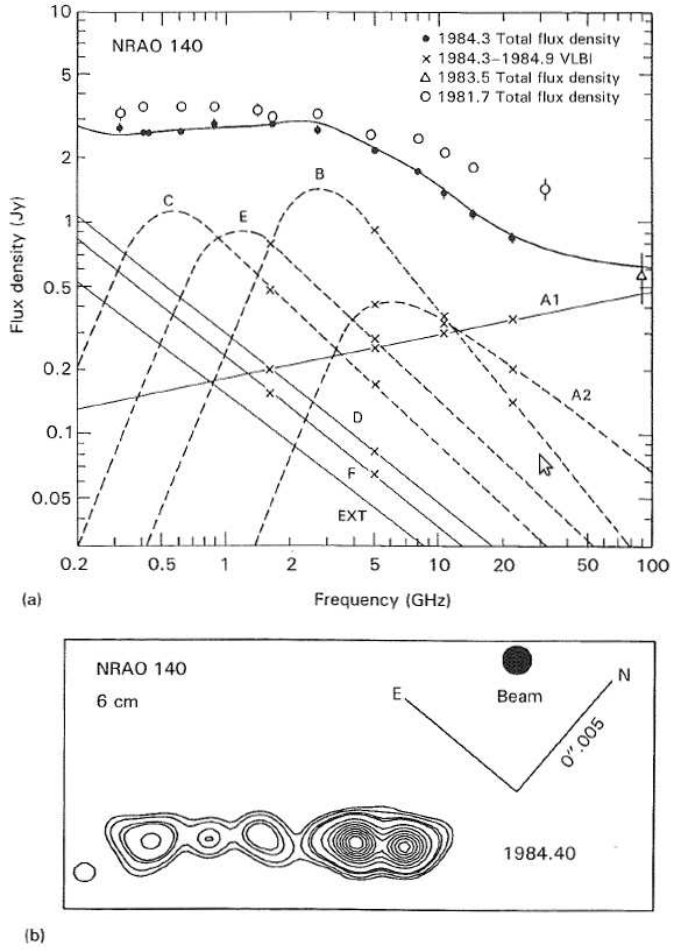

Figure 2.14: *Superposition of the synchrotron radio emission of different propagating shocks (Valtaoja et al., 1992)*

tronomy Observatory (UMRAO) at 4.8, 8, and 14.5 GHz.

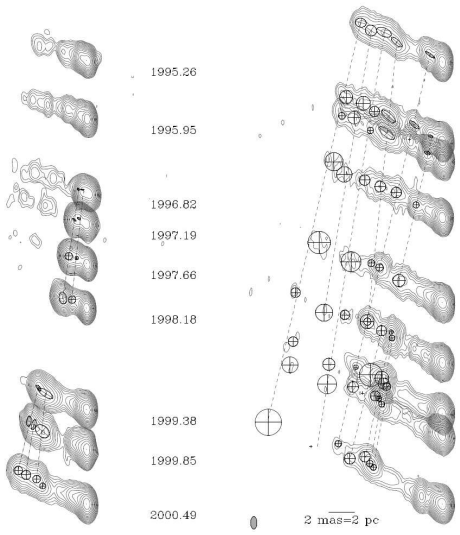

Figure 2.15: *VLBI Images of 3C111 at 2 cm (Kadler et al., 2008)*

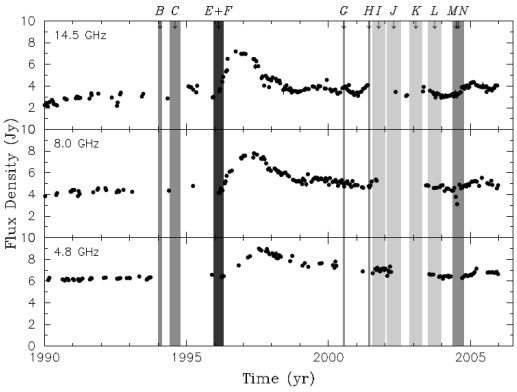

Figure 2.16: *UMRAO Lightcurves of 3C111 (Kadler et al., 2008)*

The gray vertical bars represent the different tracked blobs. At all three frequencies, the growth stage of the flare seems to start at the same time. In Fig. 2.15, the first ejected "blob" starts to form new jet components. After some time later, one can image several knots. The first component for example is measured at the highest frequency in the lightcurve first, because it is still very dense and compact, and so highly self absorbed at lower frequencies. At some time later, the lightcurve at 4.8 GHz reaches its maximum, as the jet components - or shocks - having initially been in their plateau stage, begin to decay and loose density. Hence, there are less electrons that can do synchrotron self absorption, and the components get gradually visible at lower frequencies with time. This effect gets even more significant, the longer the time proceeds. If one cuts the lightcurves at several times, one yields frequency spectra. At the beginning of the flare, these spectra are more or less flat. With time they get steeper. This is redolent of the above described generalized shock model. The spectra follow power laws like $E(\nu) \sim \nu^{\alpha}$ with the spectral index α that is shown in Fig. 2.17. Again, after Marscher (1996), the region behind the shock/ flare is important. This is the region, where electrons are accelerated to different velocities. Hence, there will be a stratifaction of synchrotron sources at as many different frequencies, as one has velocities.

As jets are broad band emitters, not only the radio bands are important for the understanding of jets.

Looking at at Fig. 2.6 again, this is a typical blazar like SED for PKS 2155−304. The left peak in the νF_{ν}-plot is due to synchrotron radiation, mostly in radio bands, the second peak towards higher frequencies - namely X-rays and gamma-rays - corresponds to inverse Compton upscattering of so called seed photons.

There are several mechanisms of doing so. On the one hand, soft X-rays mostly occur due to an upscattering of photons from the inner accretion disc by nonrelativistic electrons. On the other hand harder X-rays get emitted by either the synchrotron self Compton effect (SSC), that

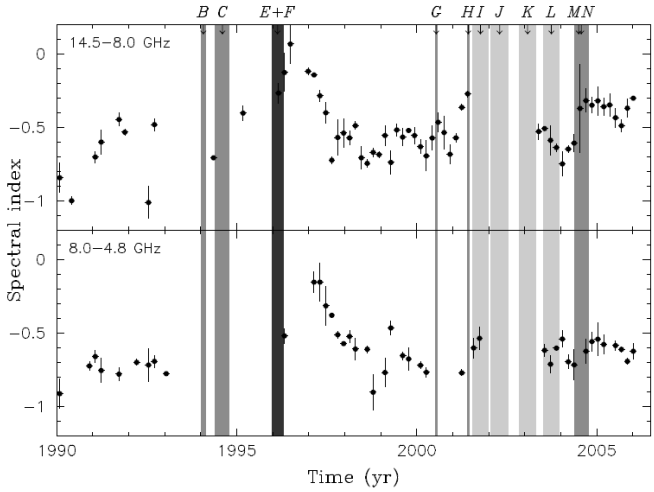

Figure 2.17: *Spectral indices of 3C 111 between 14.5 and 8.9 Ghz as well as 8.0 and 4.8 GHz, Kadler et al. (2008)*

describes the upscattering of synchrotron photons inside the jet by highly relativistic electrons accelerated in the inner jet, or the upscattering of coronal photons by the hot electron gas, that is accelerated by chaotic magnetic fields in the corona (Marscher et al. 2002, Marscher 2006b, Marscher 2006a). In the SSC case, the generated X-ray spectra have to look quite the same as sychrotron spectra, just shifted up to higher energies (Robson, 1996). There is also the possibility of inverse Compton upscattering of external photons from the CMB.
Despite most jets emit their synchrotron jet radiation in the radio waveband, there are also so called "blue blazars", whose jet emission is shifted up to X-ray energies (Bai & Lee, 2001). PKS 2155−304 is one good example for such ja blue blazar. In Fig. 2.7, the synchrotron jet emission with its data points on the right slope of the first SED-peak is located in the X-ray. A simple explanation would be that in the inner jet, the photon density due to photons from the accretion disc or synchrotron emission is quite low. Thus, these high energetic electrons can not be properly cooled down by the inverse Compton effect and keep most of their energy until reaching upper regions of the jet, where they can loose their energy producing synchrotron photons at higher energies like X-rays. In opposite, if the photon density in the inner jet is higher, more intense inverse Compton cooling lets the electrons loose higher amounts of energy untill they can at last only do synchrotron radiation at lower energetic radio wavelengths. Those blazars are calles "red blazars".
Fossati et al. (1998) and Donato et al. (2001) observed that a collection of blazars follow a so called "blazar sequence" (Fig. 2.6). One of the key findings is that the SED peaks shift to lower frequencies as the bolometric luminosity increases. The ratio between the synchrotron and invserse Compton peak frequencies, as well as the power ratio between the two peaks are constant.
Bai & Lee (2001) give one simple explanation for the increasing inverse Compton flux and the decrease of the synchrotron peak frequency. They claim that in red blazars the Compton peak is fed with photons from inverse Compton upscattering of the dense photon field in the inner jet by relativistic electrons. This will lead to lower electron energies, and thus to lower frequencies

for the SED synchrotron peak. In the model an increasing flux in the Compton peak is correlated with higher luminosities in emission lines, and a overall higher bolometric luminosity. This in turn could be responsible for a higher photon density in the inner jet, which would at the end lead to synchrotron peaks at lower frequencies. Fossati et al. (1998) thereby introduce the so called high-energy peak BL Lacs (HBL) and the low-energy peak BL Lacs (LBL), whose synchrotron emission takes place at higher energies and synchrotron peak frequencies (UV to soft X-rays), and at lower frequencies (far-IR to near-IR) respectively. A HBL/LBL in turn is the same as a high/low peaking flare, as stated by the generalized shock model. The classification with blue- and red blazars is also analogous to the one with HBL and LBL (Guetta, 2002). Another key finding regarding the blazar sequence is that all phycical and radiative characteristica can be modeled with just one parameter - the bolimetric luminosity. Guetta (2002) reproduced many SEDs by assuming an *internal shock scenario*, confirming the blazar sequence. Internal shocks are created by the black hole emitting energy on shells at different speeds. Some of these shells can interfere in turn and give rise to shocks, which cause the observed non-thermal emission by accelerating electrons and therewith giving rise to synchrotron and also inverse Compton cooling of these electrons. This process was also mentioned at the beginning of this section due to Marscher (1996). The key parameters used here are the jet power, which is proportional to the bolometric luminosity, and the intensity of the broad lines. The latter parameter is important, as the Compton cooling of electrons is mainly thought to take place in the BLR. The higher the intensity of the broad lines, the higher in turn the photon density due to the BLR.

The three main types of emission, namely synchrotron and inverse Compton for non thermal, jet based emission, and thermal emission from the disc at the infrared to ultraviolet are in turn highly correlated. Valtaoja et al. (1992) found a connection between the accreted matter, noticeable through thermal emission around optical wavelengths, and radio flares.

They measure strong time delays in order of years between the lightcurves of the optical and radio bands, which means that there is a delay in time between accretion and emission into the jet.

But also correlations between radio and gamma flux were found by Valtaoja & Teräsranta (1996), who compared the radio bands in 22 GHz and 37 GHz at Metsähovi observatory with the gamma band from *EGRET*. They found that the radio flux occurs several month after the X-ray by again identifying time delays between the appropriate lightcurves. The clue seems to be the accelerated jet model (Fig. 2.13). After the accreted matter was somehow injected into the jet, it suffers inverse Compton cooling before emitting synchrotron radiation. In between, a timelag is measured. Pushkarev et al. (2010) also detected a time delay between the radio and gamma emission. The radio data was obtained by the VLBA at 15.4 GHz, the gamma data from the Large Area Telescope (LAT) on the *Fermi* satellite. For that, 183 sources were analyzed. But this is just one part of the strong collaboration between *Fermi*/LAT and radio astronomers (Giroletti et al., 2010). Since *Fermi* has been launched, the correlation between gamma- and radio sources has been studied. Although just 10% of the known AGN are radio loud AGN, and in turn mostly strong gamma emitters, *Fermi* and its wide field of view was able to detect huge amounts of those. In the LAT Bright AGN Sample (LBAS), there were already 125 sources after three month of observation. After 1 year, the LAT First Year catalog (1LAC) contained more than 1400 sources (Giroletti et al., 2010). With this data, the assumption of a

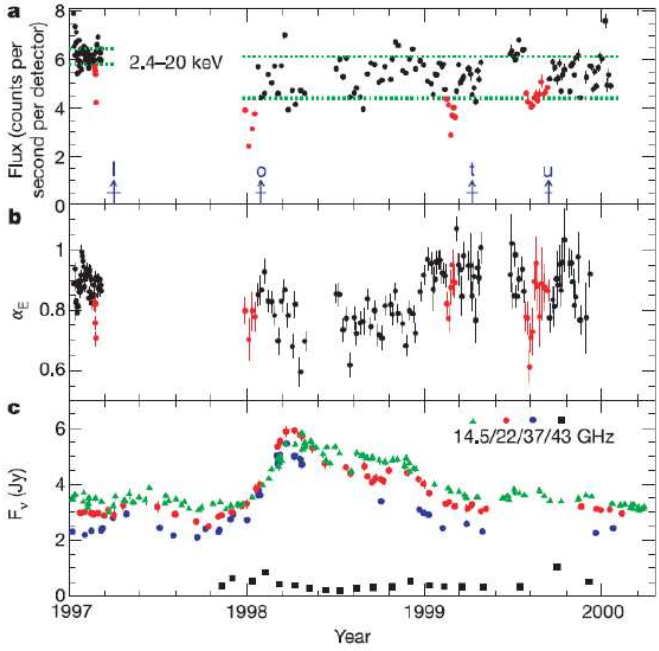

Figure 2.18: ***a:*** *X-ray lightcurve with statistically significant dips (red),* ***b:*** *X-ray energy spectral index,* ***c:*** *radio lightcurves at different frequencies (Marscher et al., 2002)*

correlation in the radio and gamma could be manifested. There are observations that at least prove that the accreted matter has to be somehow ejected into the jet. Marscher et al. (2002) and Marscher (2006b) observe dips in the soft X-ray lightcurves of 3C 120 shortly followed by a rise in radio lightcurves and the appearance of a superluminal radio component in the jet (Fig. 2.18). The current opinion of the authors is that the inner part of the accretion disc gets unstable, breaks off and falls onto the central black hole (Marscher et al. 2002, Marscher 2006b). A part of this matter will fall behind the event horizon of the black hole, but the majority is thought to be ejected into the jet - "tunneled" by dense magnetic fields around the accretion disc. There are two origins for X-rays emerging from the injected jet plasma. The first one is either the inverse Compton upscattering of synchrotron seed photons (SSC) by electrons, being accelerated to highly relativistic velocities inside the jet, or the upscattering of coronal photons by the hot coronal electron gas, as mentioned above, or both. This causes an overall powerlaw with decreasing countrates to higher energies and frequencies. The second source of softer X-rays is the inner disc. The according electrons are getting less accelerated, as the magnetic field is more polodial than chaotic in this region (Marscher, 2006a). So, photons get upscattered by them to lower X-ray energies. As one part of the inner disc breaks off, the upscattering electrons as well as the seed photons get lost, and the soft X-ray flux decreases. This is measured as dips in soft X-ray lightcurves and as hardening or steepening of the whole X-ray spectrum (see the spectral indices in Fig. 2.18 (b) coincidently decreasing with the appearance of soft X-ray dips), as it is the superposition of the soft and hard parts. As it is unlikely for the electrons of the infalling inner disc to be accelerated into the jet, because of the constancy of the hard X-ray flux, they have either to fall behind the event horizon of the black hole, or may be accelerated into the outer jet.

In addition, an increasing radio flux was measured shortly after the X-ray dips (see Fig. 2.18 (c)). The 43 GHz radio lightcurve is quite flat and less luminous compared to the other frequencies. The reason is that for this frequency, the Very Large Baseline Array (VLBA) was used, which technically can not see extended structures because of smaller beamwidths. Thus, single dish radio telescopes are measuring higher luminosities in average, as their beam width is larger.

3 Radio Observations of PKS 2155−304 with the 100m Effelsberg Telescope

3.1 Introduction to PKS 2155−304

First of all, some useful information about this source are stated in Tab. 3.1. The equatorial coordinates show that the source is best visible in the Southern Hemisphere. It can also be observed by the Effelsberg radio telescope and few other radio telescopes on the Northern Hemishere, but only at a very low elevation. Fortunately, the horizon of Effelsberg allows observations at such low elevations regaring to the position of the source in azimuth. Remarkable is the overall high luminosity from radio to TeV energies. Looking especially at the synchrotron peak at $\approx 10^{16}\,\mathrm{Hz}$ (Aharonian et al., 2009), and including the distance of the source, one still finds a flux of $\approx 5 \cdot 10^{-10}\,\mathrm{erg\,cm^{-2}\,s^{-1}}$ arriving at Earth, which corresponds to $\approx 1 \cdot 10^{-3}\ \mathrm{J\,cm^{-2}\,s^{-1}}$, which makes clear how extremely luminous the source has to be in order to guarantee such a high flux at the position of the Earth. As those blazars are variable over the whole electromagnetic spectrum from radio to gamma frequencies, multiwavelegth campaigns have to be organized. The big task of these observations is, to do them preferably simultanious because of the high source variability, which is due to relativistic beaming, as the jet is believed to point directly towards us (see Sec. 2.2.4). Using Very Long Baseline Interferometry (VLBI) techniques with the TANAMI array of radio telescopes on the Southern Hemisphere, a contour map of PKS 2155−304 was made in the first epoch of observations at 8.4 GHz. This map is shown in Fig. 3.1. Monitoring the environment of PKS 2155−304, it was found to be part of a physical group of four galaxies, which is shown by Falomo et al. (1993). The observed field of view in this survey around the central source of PKS 2155−304 coveres $3.7' \times 3.7'$.

Table 3.1: *Some properties of PKS 2155−304 (NED database, luminosity from Aharonian et al., 2009)*

galactic coordinates	~ 17.7 longitude	~ -52.2 latitude
equatorial coordinates	21h55m58.3533s RA	-30d27m54.566s DEC
redshift	0.116	
distance	472 Mpc from Hubble's law	
synchrotron peak luminosity	$\approx 10^{46}\,erg/s$	

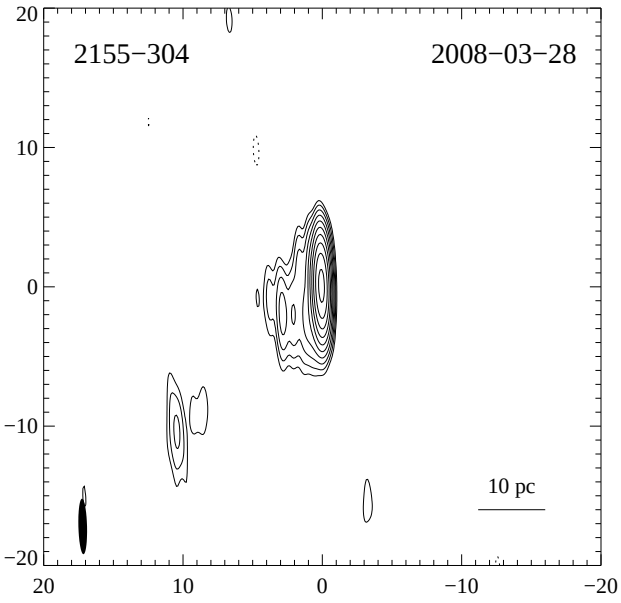

Figure 3.1: *TANAMI map of PKS 2155−304 from the first epoch of observations at* 8.4 *GHz (Ojha et al., 2010)*

3.2 Multiwavelength campaigns

3.2.1 Multiwavelength monitoring 1994

There have been several multiwavelegth campaigns regarding PKS 2155−304. One of them was done in the year of 1991, including three sessions: the first one was due to ultraviolett obsevaions with the *IUE* satellite throughout November 1991 (Urry et al., 1993). This campaign was followed up by *ROSAT* X-ray observations, also in November 1991 (Brinkmann et al., 1994). In order to complete the multiwavelength observations, at the same time, ground based radio and optical observations habe been undertoken (Courvoisier et al., 1995). The collected data were analyzed afterwards with the aim of yielding a better understanding of the physical mechanisms in blazars (Edelson et al., 1995). Fig. 3.2 shows the outcome of this multiwavelength campaign. The four data points roughly near 10^{10} Hz correspond to the radio data, while the X-ray measurements are above 10^{14} Hz (see Sec. 2.2.3). PKS 2155−304 is one of the brightest BL Lac objects known. It also shows strong variability over all wavelengths of the SED. The main results from the multiwavelength analysis are generally strong correlated variations in all wavebands. That implies that the different components, namely the jet, the accretion flow, and the supermassive black hole, have to couple in some way, which is not entirely understood yet. Soft X-ray variations are leading the ones from lower frequencies. This is in conflict with the SSC model of synchrotron photons being upscattered by accelerated electrons in the inner jet to higher energies. The accretion disc model implies that some variation should be visible first at lower frequencies, namely optical to UV, as the matter has to be accreted before doing SSC upscattering in the inner jet. As no timelags between ultraviolet and soft X-rays are detected, Edelson et al. (1995) state that SSC is unlikely to happen. However, considering Sec. 2.3 it was pointed out that soft X-rays are mostly produced by upscattering of the photon field around

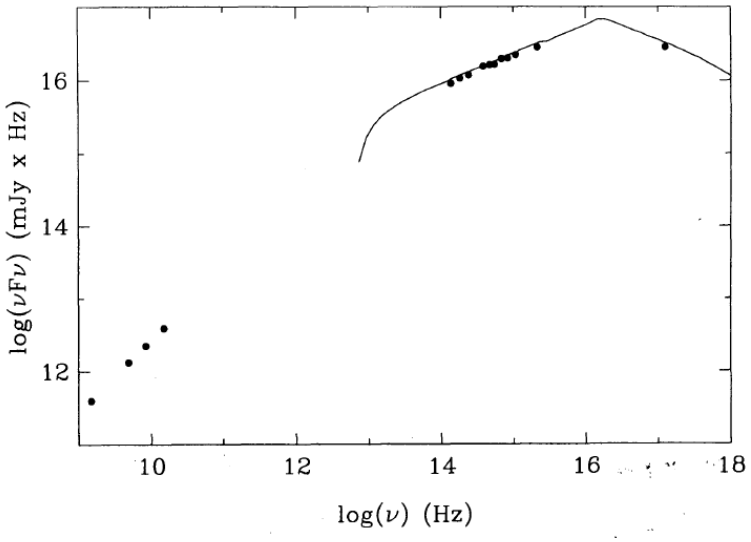

Figure 3.2: *SED of PKS 2155−304 from the 1991 multiwavelegth monitoring (Edelson et al., 1995)*

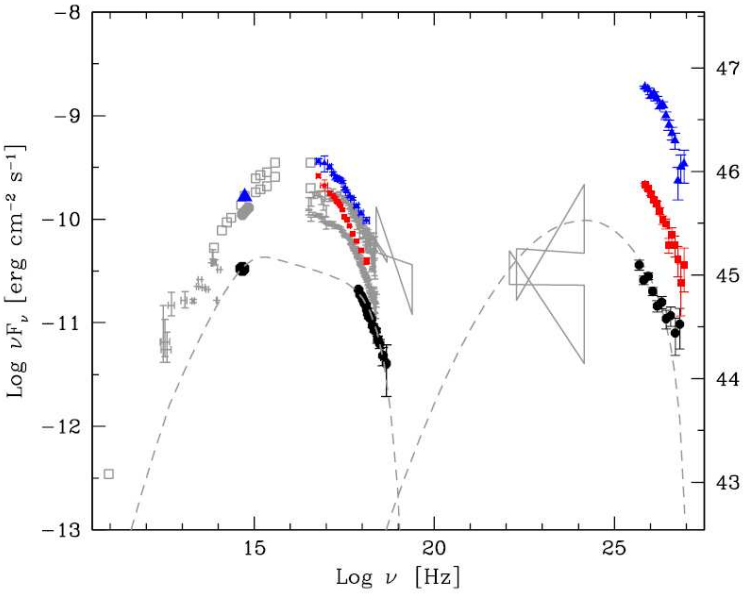

Figure 3.3: *SED of PKS 2155−304 from the 2006 multiwavelegth campaign (Aharonian et al., 2009); it also shows the strong variability at frequencies with a non-thermal origin: blue triangles correspond to the highest state, the red squares to the lowest state. The dashed line is a fit due to a one-zone SSC model*

the inner disc by surrounding electrons. Usually, only harder X-rays are produced with the SSC effect. In this case, the soft X-rays would show no timelags to the ultraviolet photons, as they originate from nearly the same region of the accretion disc.

3.2.2 Multiwavelength monitoring of the flare in July 2006

Aharonian et al. (2009) monitored PKS 2155−304 during a flare in July 2006, which was visible over the whole electromagnetic spectrum. For the gamma rays, the H.E.S.S. instrument was used, containing four ground based Cherenkov telescopes. The *Chandra* satellite together with *RossiXTE* provided the X-ray data. The optical wavebands were covered by the 32 cm Schmidt-Cassegrain telescope at Bronberg Observatory. The resulting SED is shown in Fig. 3.3. One again sees two peaks in the νF_ν-plot. Here, PKS 2155−304 is classified as a High energy

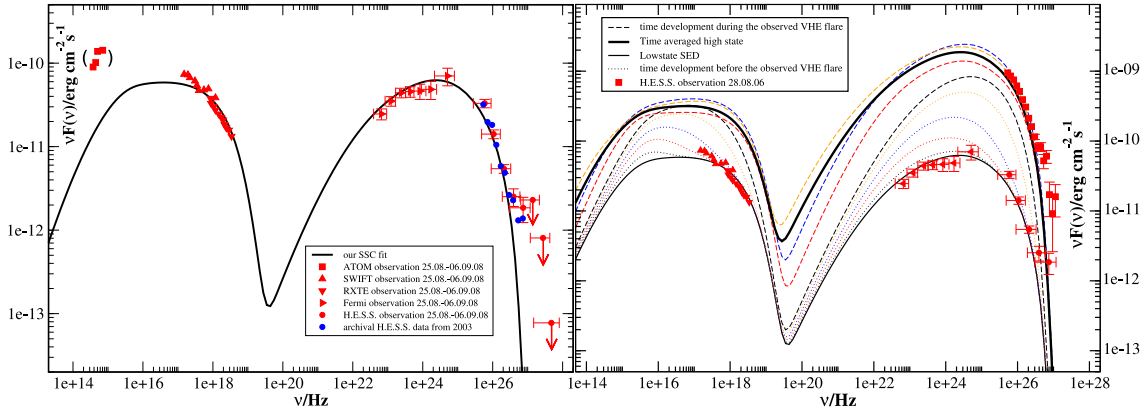

Figure 3.4: *SED of PKS 2155−304 with data from (Aharonian et al. (2009)) and FermiGST; left: low state, right: time averaged SED at the low and high state as well as the time evolution of the SED model during the flare (Weidinger & Spanier, 2010)*

peaked BL Lac object (see Sec. 2.3), as i.e. the first peak, which is due to synchrotron emission, is found at higher energies around UV to X-ray frequencies. The second peak is claimed to be due to inverse Compton upscattering of synchrotron seed photons inside the inner jet by highly relativistic accelerated electrons.
It was found, that the flare in 2006 did not move through the spectrum with time. Additionally, a strong (cubic) relation between the X-ray and gamma-ray flux was detected. This is redolent of the the well established jet model of matter being accelerated in shock fronts in the inner jet and hence doing synchrotron emission, here in X-rays. After that, the synchrotron produced (seed-) photons can be upscattered to GeV energies by (the same) high relativistic electrons in the inner jet. As these processes are highly correlated, the outcoming radiation should also be. In detail, the cubic correlation of the X-ray flux (F_{X}) and the gamma-ray flux (F_{γ}) results to behave like $F_{\gamma} \sim F_{\mathrm{X}}^{3}$. Aharonian et al. (2009) claim that it would not be possible for a one-zone SSC scenario to explain the observed SED and its variability. A one-zone SSC scenario means that one flaring jet component, which consists of one energy distribution of electrons is responsible for the observed two humped SED due to synchrotron self Compton upscattering of internal synchrotron seed photons. A two-zone scenario, however, is assumed to be a better model to explain the two humps in the SED and their variability. The first jet component shall be responsible for the "persistent" shape of the SED, especially the first synchrotron peak and its long-term variability. A second, very compact component in turn shall explain the heavy variability of the second hump in the SED and the actual flaring activity in July 2006. Hence, it has to be highly dominated by inverse Compton losses instead of synchrotron radiation. This means that the energy density of the external photon field has to be higher for the second component in order to guarantee a larger power emitted by inverse Compton processes than by synchroton radiation, which follows from the relationship of $P_{\mathrm{Compton}}/P_{\mathrm{synchrotron}} = U_{\mathrm{rad}}/U_{\mathrm{mag}}$. Here, U_{rad} and U_{mag} are the energy densities due to the radiation- and the magnetic field.
After combining the above discussed H.E.S.S. data with new *Fermi*/LAT data,
Weidinger & Spanier (2010) were able to model the observed variable SEDs (Fig. 3.4) with only a one-zone model. They assumed a different energy distribution of the injected electrons.

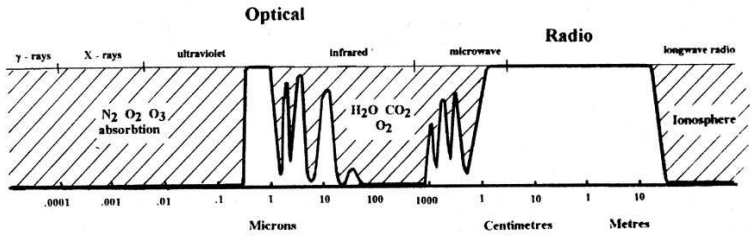

Figure 3.5: *Electromagnetic spectrum, showing the atmospheric absorption at the different wavebands (Burke & Graham-Smith, 2009)*

By now it was usual to assume a simple power law for the electrons in one jet component. Weidinger & Spanier (2010) changed this model by just injecting more electrons into the acceleration zone for certain amounts of time, which will help explaining variations in the jet's electron density. This is enough to model the observations with just a single jet component, in which a Fermi-I/II acceleration and also the inverse Compton cooling of the electrons takes place.
One general feature of all shown SEDs of PKS 2155−304 is the lacking variability and lacking flux at intermediate wavelengths between the humps, covering the infrared to ultraviolet bands. This is due to the high relativistic boosting of the jet, that is pointed towards us. Hence, the non-thermal jet emission overshines the thermal emission from the disc.

3.3 Introduction to Radio Astronomy

There is no doubt about Karl G. Jansky being the key person in radio astronomy's history. He discovered the radio noise from the Milky Way in 1933. As in these times no one expected that radio emission could give a clue on physical processes in universe, and as the signal to noise ratio was quite low, also technical problems caused a slow developement of radio astronomy. In the beginnings, observations in the infrared, optical, ultraviolett and X-ray wavelength were more common, as the results were more satisfying. Imaging in these wavebands brought wide improvements in understanding what is going on in the universe. AGN, or other radio sources, just couldn't be observed with the radio techniques that are possible today. The singe dish telescopes were quite small and no interferometry was used so far. It was challenging to receive signals from radio sources, and not from electrons inside the receivers, which cause most of the detected noise. But with time, one could improve the receivers, and concentrate more on the mechanisms in universe that cause radio emission. The main sources are electrons, that get accelerated following helical trajectories around magnetic field lines in sources like X-ray binaries, so called microquasars, active galactic nuclei, the galactic plane of our Milky Way itself and so on. Despite the receiving problems, radio rays are useful to explore the most distant sources. This is because most of the matter between the source and the ground based radio telescopes are optically thin for longer wavelengths, escpecially radio waves. Fig. 3.5 shows the absorption according to the different wavebands. Radio photons experience no absorption due to the Earth's atmosphere. Therefore - in opposite to X-ray astronomy - astronomers are able to work on ground based telescopes, which are large radio dishes. Fig. 3.3 shows a sketch

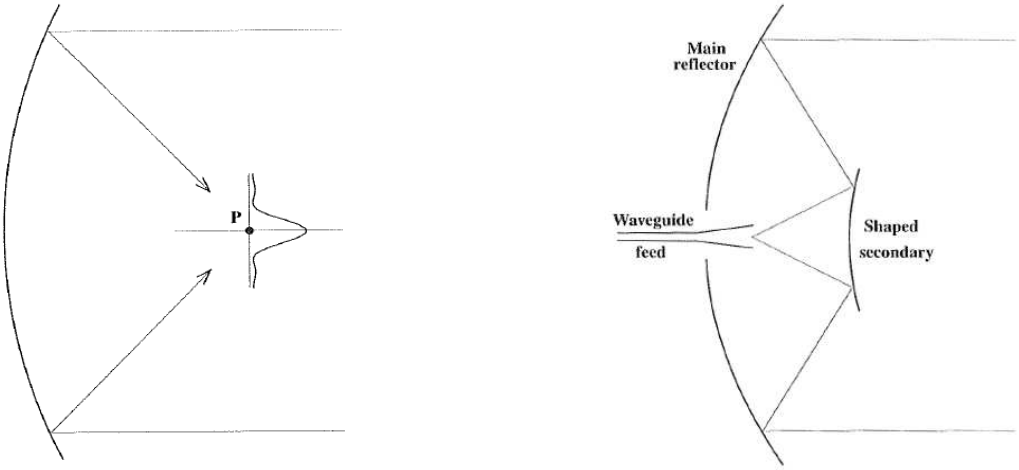

Figure 3.6: *left: airy shape of the focal point on the secondary reflector, right: reflector feed system (Burke & Graham-Smith, 2009)*

of the focal point at the secondary mirror with the typical Airy shape of a point source in the focal plane. The Full Width Half Maximum (FWHM) of this Airy function equals the angular resolution or beam width, which is proportional to $f\lambda/D$, where D is the diameter of the telescope, and f the focal length. As the radio wavelengths are quite long ranging from centimeters to meters, the diameter of radio telescopes have to be very high in order to yield small beams and good resolution. The instrument of interest in this thesis is the Effelsberg radio telescope. It works like shown in the second sketch. It consists of a parabolic collecting area, which focuses the infalling radiation beam on the secondary mirror. This reflects the light towards the centre of the collecting plane again. There, it is captured by a so called feed, a waveguide to the receiver. The diameter of the Effelsberg main reflector is 100 m, the one of the secondary reflector 6.5 m. The whole aperture area is 7854 m^2. The telescope's reflection area is covered with 2352 surface elements. It is constructed to remain always a paraboloid with a surface accuracy of just 0.5 mm. The focal length in the primary focus is 30 m. At 21 cm or 1.4 GHz, the angular resolution accounts 9.4′ (arcminutes), at 3 cm / 10 GHz, 1.15′ and at 3.5 mm / 86 GHz just 10″. For comparison - the average Seyfert galaxy has a few arcminutes in diameter. While the QSO 3C 273 has an angular diameter of only 6″. So even with the best resolution, this source remains pointlike for a single dish radio telescope.
Imaging is not possible for single dish radio telescopes, as they are operated with just one receiver for one frequency at one time. However, it is possible for an array of telescopes with long baselines, i.e. the Very Long Baseline Array (VLBA). The whole system then behaves like a new radio telescope with a much larger opening diameter. Using the technique of Very Long Baseline Interferometry (VLBI), it is possible to image a source at a given frequency.

3.4 The F-GAMMA project

The data for PKS2155−304 used in this thesis arise from the F-GAMMA project (Angelakis et al., 2008), a collaboration of the Fermi Gamma ray Space Telescope (*Fermi-GST*) and the Effels-

Table 3.2: *Used frequencies for the data reduction of PKS 2155−304*

frequency [GHz]	wavelength [mm]
23	13
15	20
10.7	28
8.3	36
5	60
2.7	110

berg 100 m radio telescope since 2007.
As we have seen in Sec. 2.3, gamma-ray and radio emission processes are highly correlated. So the aim of this collaboration is to gain better multifrequency data for further understanding. In addition SEDs can be understood even better regarding for example the variability, which is only possible with the high data quality achieved by *Fermi* and the Effelsberg radio observatory. Two other radio telescopes IRAM (30 m) and the 40 m Owens Valley telescope are also involved in this project, but their data are not used here.
Fermi-GST covers the high energy band between 20 MeV and > 300 GeV, wich corresponds to span of $\sim 10^{21}$ Hz to $\sim 10^{25}$ Hz. Its huge field of view allowes to observe the whole high energy sky within 3 hours. The sample of radio sources that are monthly observed with Effelsberg, overlap with the MOJAVE survey at 2 cm that uses the VLBI technique.
The Effelsberg monitoring programm operates at frequencies between 2.64 GHz and 42 GHz. The used frequencies in this thesis are shown in Tab. 3.2.

3.5 The Effelsberg Single Dish Radio Telescope - physics and data reduction

In this section I will concentrate on the physics and techniques of single dish radio telescopes, expecially the Effelsberg 100 m radio telescope.

The following subsections will basically follow Burke & Graham-Smith (2009), Fuhrmann (2004), and Angelakis (2007).

3.5.1 Beaming pattern, antenna temperature

The Effelsberg single dish radio telescope has a parabolic reflection area with a diameter of 100 m. The radiation is led into the feed lying in the centre of the main dish, by being reflected at a secondary mirror (see Fig. 4.3). The "feed" is feeding the signal to the receiving unit. First, it is important to understand the radiation itself. The incoming radiation consists of electromagnetic waves having some degree of polarization (see Sec. 2.2.1). Further, there is a difference between flux and power: the "flux" always describes the energy per surface. The energy flux per solid angle, B, is also called the *brightness*, whereas the *specific brightness* B_ν equals the energy flux per solid angle and frequency. Thus, the total flux is yielded by

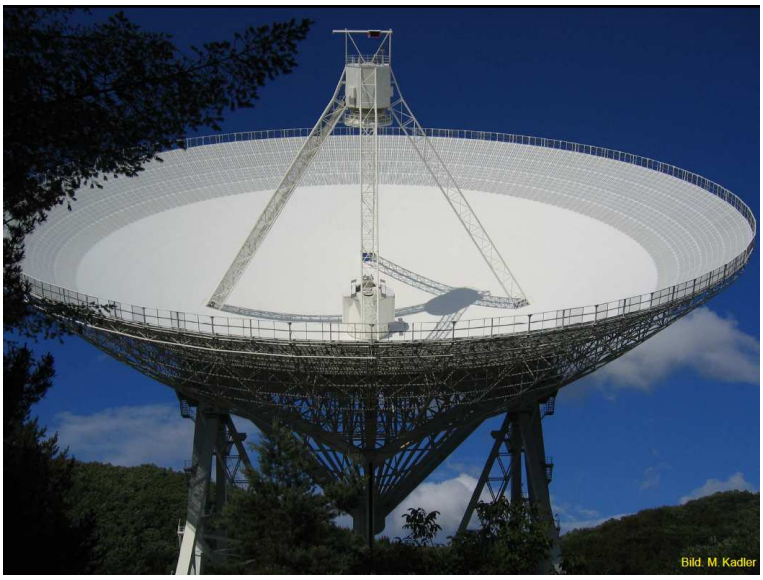

Figure 3.7: *Effelsberg 100m radio telescope (M. Kadler)*

Table 3.3: *Notations for measuring the energy of radiation*

	sign	units
specific power/ power density	P_ν	W/Hz
specific flux/ flux density	S_ν	W/Hz/m^2

integrating the specific flux: $S = \int\int\int B_\nu(\theta,\phi) d^2\Omega d\nu$. The unit for measuring the flux density is one *Jansky* with 1Jy $= 10^{-26}$ W/m^{2}Hz, because of the low energy density arriving on Earth from extragalactic radio sources.
However, if the incoming radiation is not due to a black body, but to a power law, one will find an equivalent antenna temperature. This is the flux an antenna would measure, if it was enclosed by a black body radiator. The energy density of black body radiation follows the Planck distribution with

$$u_\nu d\nu = \frac{8\pi h\nu^3}{c^3} \frac{1}{e^{\frac{h\nu}{kT}} - 1} d\nu. \tag{3.1}$$

The radiation density emitted from the surface of a black body into a solid angle $d\Omega$ is

$$S_\nu d\nu d\Omega = \frac{2h\nu^3}{c^2} \frac{1}{e^{\frac{h\nu}{kT}} - 1} d\nu\, d\Omega. \tag{3.2}$$

For high temperatures, $h\nu \ll kT$, the Rayleigh-Jeans approximation (Fig. 4.4) holds with

$$S_\nu d\nu = \frac{2kT}{\lambda^2} d\nu. \tag{3.3}$$

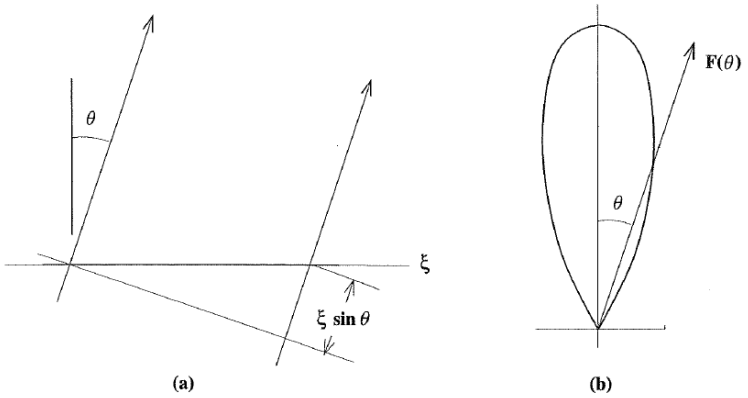

Figure 3.8: ***a)*** *linear current distribution with a phase between two emission points of* $\xi \sin\theta$, ***b)*** *radiation pattern* $F(\theta)$ *of the one-dimensional current distribution (Burke & Graham-Smith, 2009)*

Using the Planck distribution applied to the mean energy per mode inside a black body $P_\nu = h\nu/(\exp h\nu/kT - 1)$ with the units of W/Hz (see Tab. 3.3), one finds

$$P_\nu d\nu = kT d\nu. \tag{3.4}$$

The specific power for an antenna as reveiver is

$$P_\nu d\nu = \frac{1}{2}\int_{4\pi} S_\nu A_{\text{eff}} d\Omega d\nu = 2\pi A_{\text{eff}} \left(\frac{2kT}{\lambda^2}\right) d\nu. \tag{3.5}$$

The factor 1/2 is necessary, as only one direction of polarization is measured here. Applying Equ. 3.4, one finds

$$kT d\nu = \frac{4\pi}{\lambda^2} kT d\nu A_{\text{eff}} \tag{3.6}$$

$$A_{\text{eff}} = \frac{\lambda^2}{4\pi} G. \tag{3.7}$$

$$\tag{3.8}$$

Equ. 3.7 combines the receiving and transmitting mode of a radio telescope. In the *receiving mode*, the received power as a function of the effective surface is $P_\nu = A_{\text{eff}} S_\nu$. For an antenna in the *transmitting mode* however, the *gain* G describes the ratio of the energy flux $S(\mathbf{a})$ in the direction $\mathbf{a}$ and the energy flux for an isotropic radiating source.
In order to describe, how this radiation is captured by the radio telescope, imagine a single dipole emitting electromagnetic waves into the surrounding space. Inside the dipole, electrons are getting accelerated by some alternating voltage. The same mechanism would be infalling waves, that accelerate the electrons in the dipole, which causes an alterning voltage in the same. The surface of a radio telescope is a two-dimensional accumulation of many of those dipoles. Now, again, imagine a single dipole with a linear current density $g(\xi)$. Following the Fraunhofer approximation for the far-field, and integrating over all currents, one finds the radiation pattern

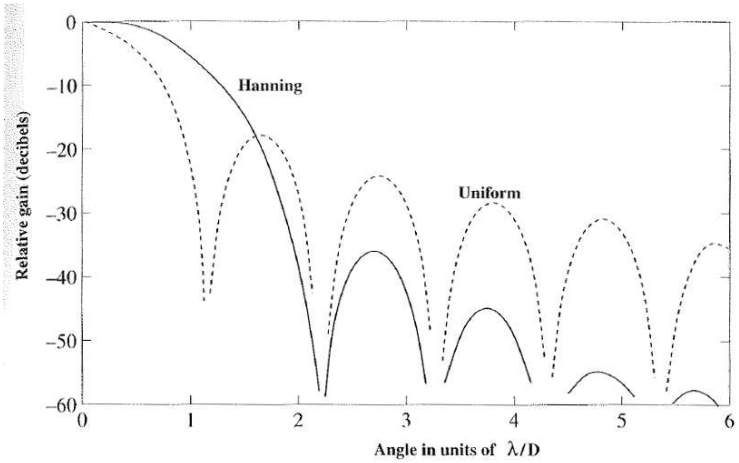

Figure 3.9: *Power beaming pattern for a circular aperture with an uniform and tapered surface (Hanning), (Burke & Graham-Smith, 2009)*

to be

$$F(\theta) = \int g(\xi) e^{-i(2\pi \frac{\xi\theta}{\lambda})} d\xi. \tag{3.9}$$

Analogous, the radiation pattern of a two-dimensional current distribution (Burke & Graham-Smith, 2009) is

$$F(\theta, \phi) = F_e(\theta, \phi) \int \int g(\xi, \phi) e^{-i(2\pi(\xi\theta + \eta\phi)} d\xi d\eta. \tag{3.10}$$

This now should be compared to the illuminating of a single slit and the resulting far-field radiation pattern in Fraunhofer approximation (Peschel, 2009), which is

$$u(x, y, z) = \int d\alpha \int d\beta \bar{u}_o(\alpha, \beta) e^{i\sqrt{k^2 - \alpha^2 - \beta^2} z} e^{i\alpha x} e^{i\beta y} \tag{3.11}$$

with the vector $\mathbf{k} = 2\pi/\lambda = (\alpha, \beta, \gamma)$ that describes the propagation of a wave. $\bar{u}_o(\alpha, \beta)$ is the Fourier transform of the initial homogenic radiation distribution in the plane of the slit, which is translated in spatial coordinates x, y, z by some Fourier transform in the far-field.
So, analogous, the radiation pattern $F(\theta, \phi)$ in the far field of the telescope dish, is just the Fourier transform of the initial current distribution in the plane of the telescope's main reflector. Further calculations lead to a more intuitive formula for the radiation pattern

$$F(\theta) = \frac{J_1[\pi(D/\lambda)\sin\theta]}{\pi(D/\lambda)\sin\theta} \tag{3.12}$$

that is just dependent on θ due to symmetry, where J_1 is a Bessel function (Burke & Graham-Smith, 2009). Fig. 3.9 shows the relative power gain, which equals the Fourier transform of the auto-correlation of the current density distributions. The shape is quite the same as the radiation pattern from Equ. 3.12.

[3] `http://helene.ethz.ch/rapp/praktikum/pics/keule3d.gif`

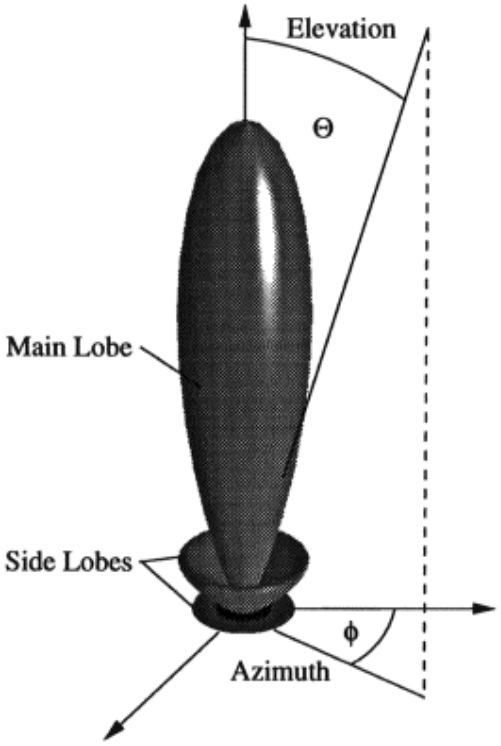

Figure 3.10: *Radiation pattern $F(\theta, \phi)$ for a parabolic radio telescope with the main and side lobes* [3]

The untapered surface yields an uniform Airy function, which reminds of the far-field radiation pattern of a illuminated circular aperture in Fraunhofer approximation. The problem about a radio telescope with an untapered, uniform surface is, though that the sidelobes are quite strong in this case, as one can see in Fig. **??**. The aim however is the measurement of an extragalactic radio source with an angular diameter of less than the width of the central "coil" of the beaming pattern. Sidelobes would just collect unwanted radiation from Earth or other strong radio sources in the projected vicinity of the actual source. The solution is a tapered parabolic telescope surface, which leads to the "Hanning pattern" in Fig. **??**. Here, the sidelobes are still exsisting, but not as strong because of the smaller effective area of the telescope. The angular resolution λ/D of a radio telescope in turn equals the width of the main maximum of the radiation pattern, which collects the main amount of radiation. For optical, imaging instruments though, the angular resolution is also proportional to λ/D, but there, the field of view is much wider than the one of radio telescopes. So, it is crucial to have large collecting areas, in order to yield an as narrow beam width as possible.
To define the antenna's output, have a look at the flux power in Equ. 3.5, which corresponds to isotropic radiation and a detection with a spherical collection surface of 4π. Here, the effective surface of the radio telescope can not be integrated over the whole solid angle $d\Theta$. The power therefore is

$$P = \int_{4\pi} S_\nu A_{\text{eff}}\, d\Omega \tag{3.13}$$

with the lacking factor of 1/2, as the Effelsberg telescope is able to detect both polarization

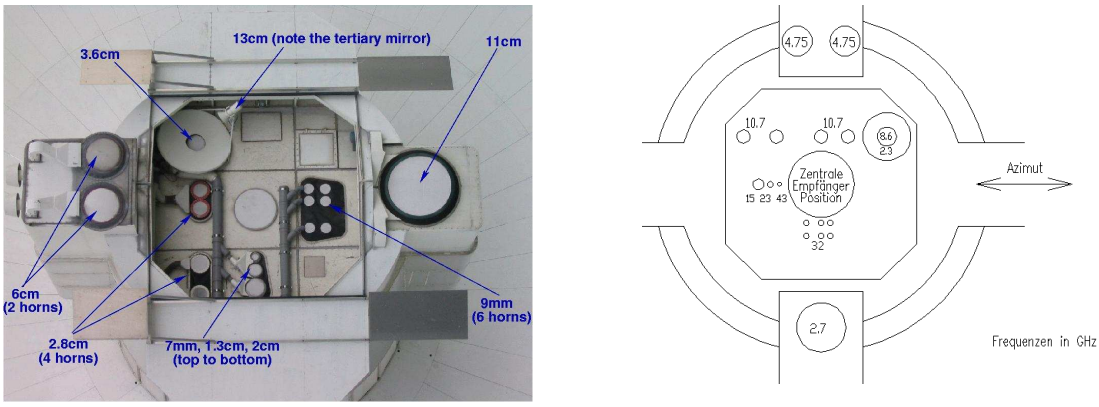

Figure 3.11: *Location of the frequency specific receivers in the primary focus (left) and the secondary focus (right)* [4]

directions. The antenna temperature then will be

$$T_\mathrm{a} = \lambda^{-2} \int_{4\pi} T_\mathrm{b}(\theta,\phi) A_\mathrm{eff}(\theta,\phi)\, d\Omega \tag{3.14}$$

with the flux density replaced by the brightness temperature T_b (Burke & Graham-Smith, 2009). Fig. 3.10 shows the main lobe that catches up most of the source-radiation. One can now make the following distinctions comparing the angular width of the antenna's main lobe, θ_a, with the one of the source, θ_s:

$$\begin{aligned} \theta_\mathrm{s} > \theta_\mathrm{a} &\Rightarrow T_\mathrm{a} \leq T_\mathrm{b} \\ \theta_\mathrm{b} < \theta_\mathrm{a} &\Rightarrow T_\mathrm{a} > T_\mathrm{b} \end{aligned} \tag{3.15}$$

In the latter case, when the source is smaller than the width of the main lobe, the telescope will detect radiation from the vicinity through its side lobes. The detected antenna temperature will then extend the brightness temperature of the source.

3.5.2 Receivers

The frequency specific receivers of the Effelsberg radio telescope are located both in the primary and secondary focus (Fig. 3.5.2). Each reveiver is locked to a feed, a corrugated, circular horn, which catches up the radiation and transmits it to the receiver itself (Fig. 3.12).
After the signal has passed the feed, it will be divided into two new signals: one left and one right hand circular polarized signal. Both will take equal ways inside the receiver. First, they pass a linear receiver, which amplifies the signal and trims it to a bandwidth $\mathcal{B}$ in frequency. This aplifying receiver "transports" the incoming signal with a *transfer function*. It can be shown that a $\delta(t)$-peak pulse will diminish with time of the order $1/\mathcal{B}$ after passing the linear

[4] `http://www.mpifr-bonn.mpg.de/div/electronic/content/receivers/english_overview.html`
[5] `http://www.mpifr-bonn.mpg.de/div/electronic/content/receivers/0_7-1_3-2cm.html`

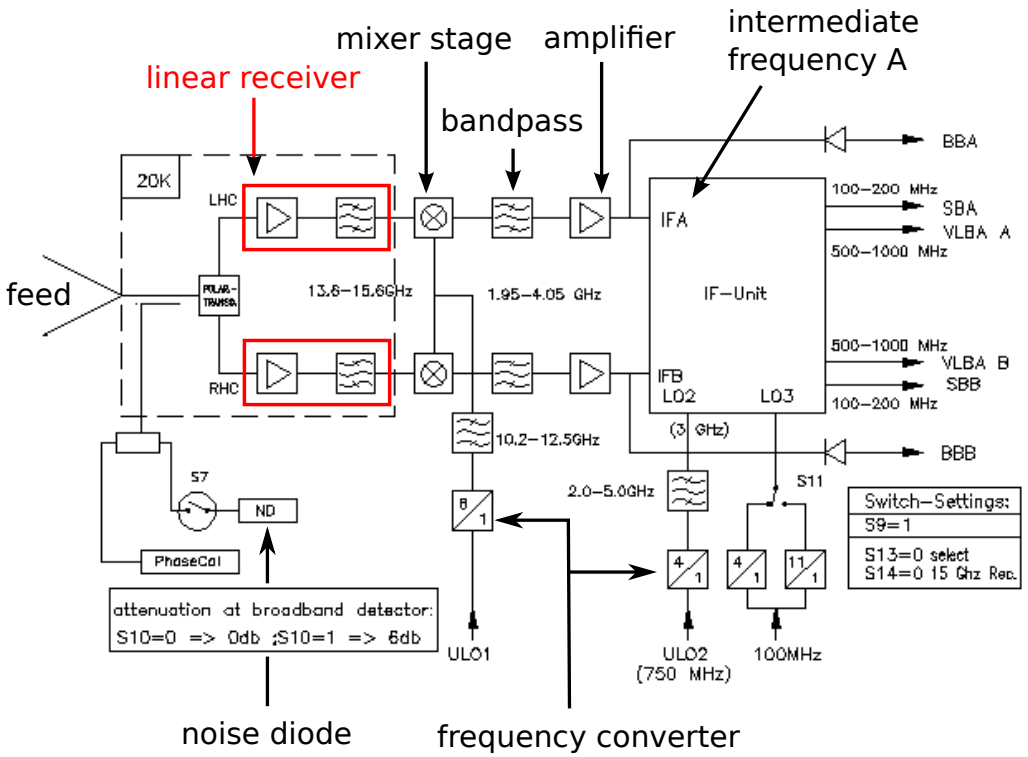

Figure 3.12: *Effelsberg 15 GHz reveiver* [5]

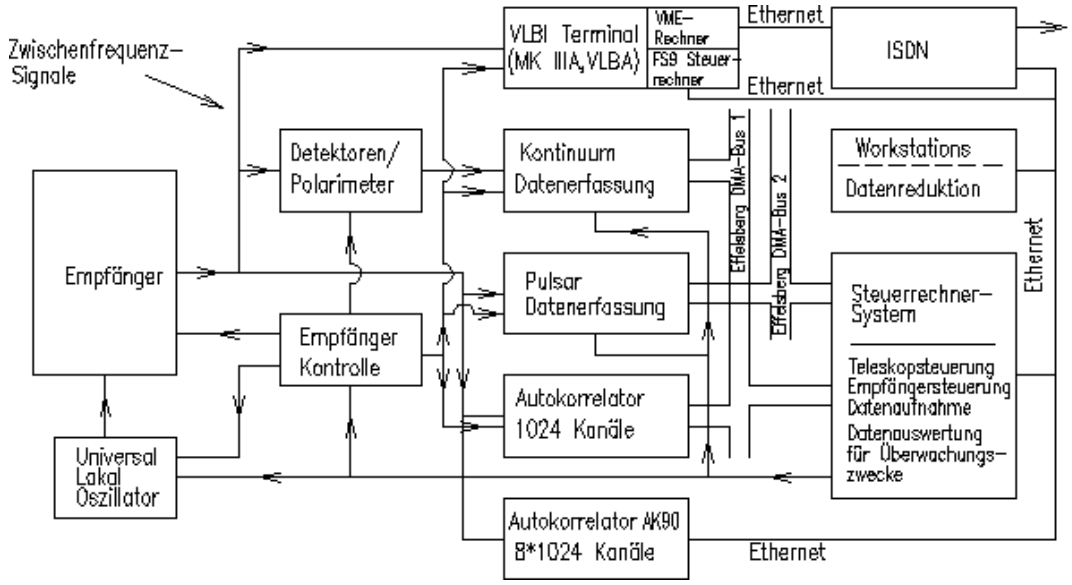

Figure 3.13: *Effelsberg reveiving system* [5]

receiver. This effect, which also applies for other signal types, is called *ringing*. So, also the random noise of the receiver itself will ring out after $1/\mathcal{B}$. This is one way of filtering the unwanted noise (Burke & Graham-Smith, 2009).
Because of technical advantages, the signal has to be converted down in frequency to a so called intermediate frequency. This is done by mixing the signal with a local oscillator. The outcome are frequency-differences, which represent smaller frequencies than the original ones. Now, the signal will pass the autocorrelator (Fig. 3.13). If there is a timelag between two signals with the voltages $u(t)$ and $u(t+\tau)$, the autocorrelation function $R(\tau)$ will multiply these two signals, and integrates them over the time t in an interval of $[-T/2, T/2]$:

$$R(\tau) = \int_{t-T/2}^{t+T/2} u(t')u(t'+\tau)dt' \tag{3.16}$$

Now, after the Wiener-Khinchin theorem (Burke & Graham-Smith, 2009), the Fourier transform of this autocorrelation will give the wanted power density:

$$S(\nu) \overset{\text{FT}}{\Leftrightarrow} R(\tau) \tag{3.17}$$

If there are no timelags between the signals it will be sufficient just to integrate over the square of the voltage signal:

$$\langle P \rangle = \int_{t-T/2}^{t+T/2} u(t)^2 dt \tag{3.18}$$

This corresponds to an average value of a noise-afflicted signal in the time interval $-T/2$ and $T/2$, which of course just can be an estimate value.
This makes sense, as the power of some current is defined as $P = UI = U^2/R$. Now, after the autocorrelation, the receiver's output has units of power. In order to cancel out influences of (bad) weather, there is a second horn, the so called *weather horn*, which can be subtracted from the measured system temperature. This is worthwhile, especially at lower wavelengths, whose data is most affected by atmospheric disturbances.

3.5.3 Scanning method

The Effelsberg radio telescope is doing so called cross scans, where the main beam pattern is driven twice orthogonally in azimuth elevation over the source. The best angular resolution is achieved for a wavelength of 3.5 mm or 86 GHz with $10''$. But because of a highly dusturbing influence of weather at such small wavelength, my raduced data for PKS 2155−304 will start at 13 mm. Here, the angular resolution will be approximately below $1'$. As most compact BL Lac sources, as well as PKS 2155−304, will have extensions of only a few milliarcseconds, these sources appear pointlike for the Effelsberg telescope. Therefore the measured system temperature in the cross scans have Gaussian shapes, as one can see in Fig. 3.14. But before these "good" scans are made, there are in most cases two prior scans:

- *pointing scan:* first raw scan, as immediatly after the telescope was moved, especially the pointing can vary untill the telescope calmed in deforming itself;
- *focus scan:* also the focus has to be adjusted, as the deformed dish always remains in a

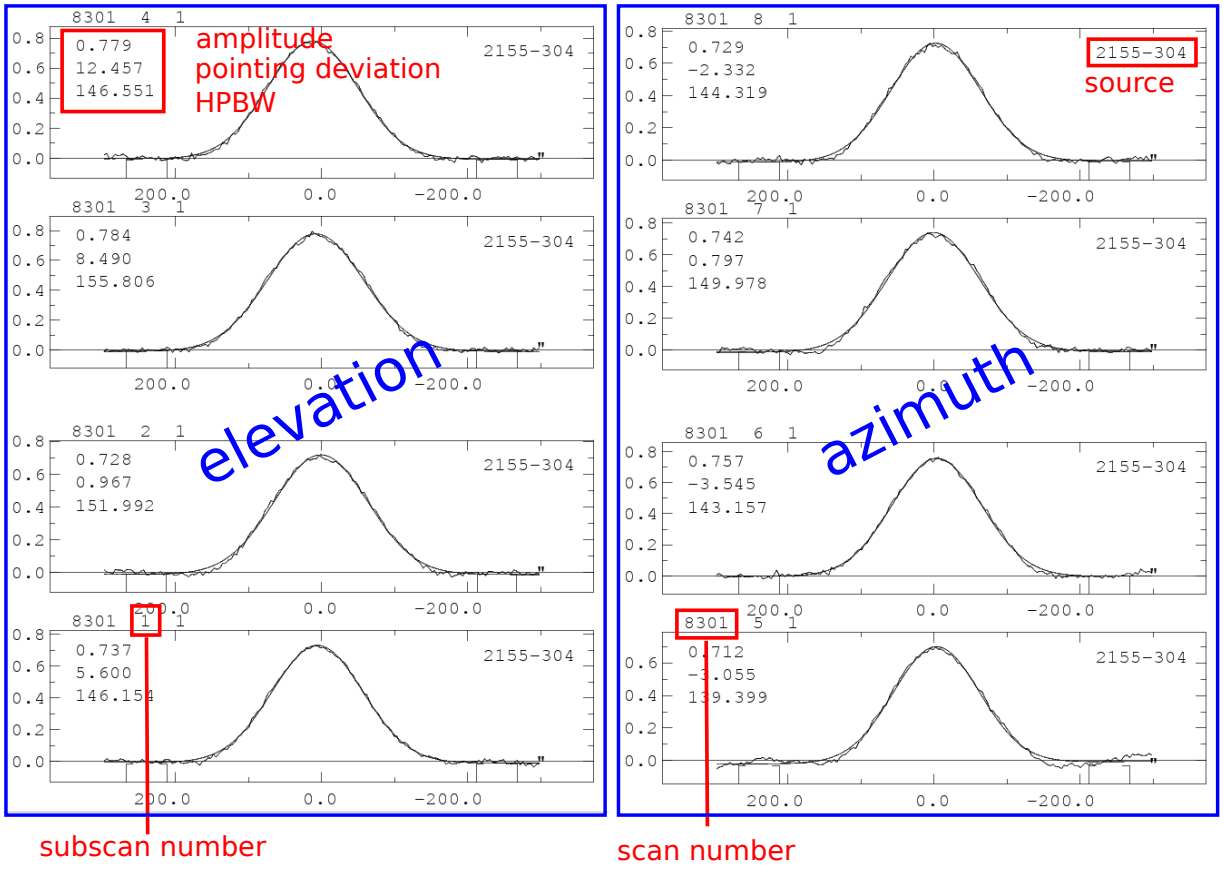

Figure 3.14: *Eight subscans in azimuth and elevation for PKS 2155−304 with the scan number 6569. As described in the figure, these subscans give information about the character of the Gaussian profiles, namely the amplitude, the pointing deviation of the telescope's main lobe from the source's centre, and the Half Peak Beam Width (HPBW)*

parabolic shape after construction;

- *scan itself:* scan in azimuth and elevation containing two subscans each (back and forth). These subscans are numbered from 1 to 8;

3.5.4 Gaussian fits, diode calibration, opacity-correction

As already pointed out, the cross scans give Gaussian distributed data points. These have to be fitted with a Gaussian curve, which can be seen in Fig. 3.14. The outcoming data has units of power, as the received voltage has already been autocorrelated. Better would, however, be the unit of antenna temperature. Hence, instead of the feed input, a noise diode is switched into the receiving system. Its signal will take the same way through the receiver as the source's signal. The equivalent temperature of the diode's noise is well known. Thus, it can be used as a (secondary) calibrator (Angelakis, 2007). After switching on the diode, one has two power signals: one antenna signal, and one of the diode. In detail, this process takes place in four phases, each 16 ms in duration. In each interval, the received photons are integrated in order to get the resulting power signal. In the last two phases, the noise diode is switched on. All these four individual measurements are combined to the final signal, called *sig*

$$sig = F1 + F2 + (F3 + D3) + (F4 + D4) \tag{3.19}$$

where F is due to the feed signal, and D due to the diode signal. One can assume that the signal power from the feed and diode will not change during these 64 ms. Therefore Equ. 3.19 becomes

$$sig = 4F + 2D. \tag{3.20}$$

Now, one has four phases, where the source itself is measured with the antenna, and at two phases, in which the diode is switched on.
One can further generate a second calibration signal called *cal* with

$$cal = -(F1 + F2) + (F3 + D3) + (F4 + D4) = 2D \tag{3.21}$$

which is the same signal as *sig*, with the only difference that $F1$ and $F2$ are substracted.
Now, one can build the ratio of the signal *sig*, containing the diode plus the sky, and the signal *cal*, containing the diode only. This ratio is the factor, which allows to calculate the antenna temperature T_a from the well known noise diode temperature T_cal (Angelakis, 2007). Note: in order to have equal numbers of phases in both signals, one has to multiply the two remaining diode phases ($2D$) by two. This is possible as the diode's power should not change with time:

$$T_\mathrm{a} = \frac{sig}{2cal} T_\mathrm{cal} = \left(\frac{F}{D} + \frac{1}{2}\right) T_\mathrm{cal} \tag{3.22}$$

The uncertainty ΔT of this antenna temperature (Burke & Graham-Smith, 2009) is dependent on the bandwidth $\mathcal{B}$ of the receiver, and the integration time T of the outcoming signal in the autocorrelator:

$$\Delta T_\mathrm{a} = \frac{T_\mathrm{a}}{\sqrt{\mathcal{B}T}} \tag{3.23}$$

As we have seen in Subsec. 3.5.1, the beaming pattern of the telescope consists not only of one main lobe, but also of several sidelobes. Although these are highly suppressed by the parabolic shape of the main reflector, they still gather unwanted radiation from ground or other disturbing sources. This can be expressed by T_{sl}. In addition, some of the equivalent signal temperature can get lost in the receiving system (T_{loss}). Some noise from the receiver (T_{noise}), which could not be filtered, can also be a part of the final system temperature. Only small contributions are expected to derive from the cosmic microwave background, T_{CMB} or bright celestial sources, T_{cs}. The most important part, though, is the lacking flux due to athmospheric absorption (T_{atm}). All in all, the received system temperature can be written as the contribution from

$$T_{\mathrm{sys}} = T_{\mathrm{source}} + T_{\mathrm{atm}} + T_{\mathrm{sl}} + T_{\mathrm{loss}} + T_{\mathrm{noise}} + T_{\mathrm{CMB}} + T_{\mathrm{cs}}. \tag{3.24}$$

One can constrain on atmospheric absorption and summarize all other disturbing contributions to T_{dis}:

$$T_{\mathrm{sys}} = T_{\mathrm{source}} + T_{\mathrm{atm}} + T_{\mathrm{dis}} \tag{3.25}$$

Applying some calculations regarding the radiative transfer, one can try to gain control over the part due to absorption.
The equation for radiative transport, expressed with the specific opacity κ_ν and emissivity ϵ_ν, is

$$\frac{dI_\nu}{ds} = -\kappa_\nu I_\nu + \epsilon_\nu. \tag{3.26}$$

Introducing the source function $S_\nu = \epsilon_\nu/\kappa_\nu$, one can rewrite Equ. 3.26 to

$$\mu \frac{dI_\nu(\mu, \tau_\nu)}{d\tau_\nu} = I_\nu(\mu, \tau_\nu) - S_\nu(\tau_\nu) \tag{3.27}$$

using $d/ds = \mu\, d/dx$ and $-\kappa_\nu dx = d\tau_\nu$. The solution of this differential equation is

$$I_\nu = I_\nu(0)e^{-\tau_\nu} + S(1 - e^{-\tau_\nu}). \tag{3.28}$$

Replacing the source function with the eqivalent temperature of the atmosphere, and the remaining intensity with the brightness temperature T_{sys}, measured with the telescope, one finds

$$T_{\mathrm{sys}} = T_0 e^{-\tau_{\mathrm{atm}}} + T_{\mathrm{atm}}(1 - e^{-\tau_{\mathrm{atm}}}). \tag{3.29}$$

As the flux from the source containing all other influences (T_0) does not pass the atmosphere, this equation can be rewritten as

$$T_{\mathrm{sys}} = T_0 + T_{\mathrm{atm}}(1 - e^{-\tau_{\mathrm{atm}}}) \tag{3.30}$$

with $T_0 = T_{\mathrm{source}} + T_{\mathrm{dis}}$. It is easier, to express the opacity τ_{atm} as the opacity κ_{z} at the zenith (elevation 90°) multiplied with a factor called the air mass (AM), which gives weight to κ_{z} depending on the elevation: $\tau_{\mathrm{atm}} = \tau_{\mathrm{z}} \cdot \mathrm{AM} = \tau_{\mathrm{z}} \cdot (1/\sin(\mathrm{elv}))$. Hence, Equ. 3.30 turns into

$$T_{\mathrm{sys}} = T_0 + T_{\mathrm{atm}}(1 - e^{-\tau_{\mathrm{z}} \cdot (1/\sin(\mathrm{elv}))}) \overset{\tau \ll 1}{\approx} T_0 + T_{\mathrm{atm}} \tau_{\mathrm{z}} \cdot (1/\sin(\mathrm{elv})). \tag{3.31}$$

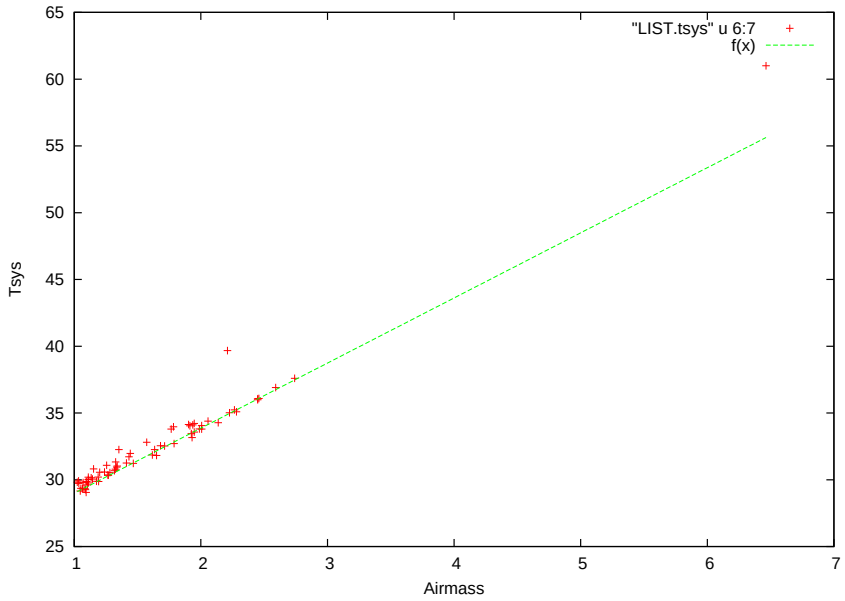

Figure 3.15: *System temperature for one primary calibrator at different elevations and airmasses; the opacity can be derived from the slope of the line fit; here for epoch 14 and a wavelength of* 60 *mm (Fuhrmann, 2004)*

As shown in Fig. 3.15, one can plot T_{sys} of one primary calibrator against the airmass (AM). As the dependence is linear, the slope directly yields τ_{atm}.
Having determined the opacity, the actual system temperature can be corrected for absorption. These three tasks, the Gaussian fit, the diode calibration and at last the opacity correction, are done with the routine `cont2` from the `TOOLBOX` routine collection from the Max Planck Institute for Radio Astronomy in Bonn, which operates the Effelsberg radio telescope. The input of this routine is a `.tot`-file, which contains all necessary parameters in the header:

```
 * ----------------------------
* cont2 command file
* produced automatically by:
* CreateCont2File
* Wed Jul  1 15:17:50 CEST 2009
* receiver 60 mm
* ----------------------------
DEFINE_DATA_TYPE=DATA_ONLY VAX
eachphset
rxn=1
tcal=1.8 648000
* ----------------------------
sig1=a1 a2 a3 a4 b1 b2 b3 b4 -e1 -e2 -e3 -e4 -f1 -f2 -f3 -f4
cal1=-a1 -a2 a3 a4 -b1 -b2 b3 b4 *2
* ----------------------------
baseline=yes
baselinedata=5 10 10 5
gaussfit
punchfit
```

```
* ----------------------------
plot=yes
plotformat=1 2 5
y-length=4
* ----------------------------
switch_to_next_E0i=yes
* ----------------------------
```

Here, one can find the typical and well known diode temperature T_{cal} as "tcal", as well as the parameters for *sig* and *cal*. With "gaussfit", the routine `cont2` will do the fits to the data, and with "plot=yes" it will plot the data including the Gaussian fits. After the header, a source list follows, which tells, which sources have to be treatet.

3.5.5 Pointing correction

If there is a pointing deviation between the maximum source intensity and the maximum of the telescope's beaming pattern, the routine `corr_point` can correct this deviation by knowing the deviations in azimuth and elevation (x_{az}, x_{elv}), as well as the HPBW of each subscan (θ_{az}, θ_{elv}).
The real flux, e.g., for azimuth $S_{\mathrm{az}}^{\mathrm{corr}}$, corrected for its pointing deviation, can be written as a simple two dimensional Gauss:

$$S_{\mathrm{az}}^{\mathrm{corr}} = S_{\mathrm{az}} \exp\left[4 \ln 2 \cdot \left(\frac{x_{\mathrm{az}}^2}{\theta_{\mathrm{az}}^2}\right)\right]$$

After the pointing correction, the corrected fluxes of all subscans belonging to one source are averaged. The pointing deviation falls more into account at higher frequencies, as then the antenna beam gets smaller.

3.5.6 Flux calibration and gain correction

The *primary calibrators* allow to translate the gained antenna temperature to flux units. The conversion of those units is yielded by exactly knowing the flux of so called primary calibrators at the appropriate wavelength. The primary calibrator's well known flux values in Janskys are set in ratio with the measured values in Kelvin for the same sources:

$$S^{\mathrm{obs}}\ [\mathrm{K}] = S^{\mathrm{soll}}\ [\mathrm{Jy}] \cdot x\ \left[\frac{\mathrm{K}}{\mathrm{Jy}}\right] \tag{3.32}$$

For the Effelsberg data this is done using the routine `eff_flux`, which calculates the calibration factor. Based on this factor, the same routine translates the system temperature in Janskys.
Although the telescope will deform while changing elevation due to its huge weight, the parabolic main reflector will remain parabolic in each elevational position thanks to constructional efforts. Therefore, on the one hand the focus has to be adjusted, which is done in the above mentioned focus scan, but on the other hand also the radiation pattern changes due to the changing effective telescope area. So the calculated flux amplitude has to be corrected by a model adapted for the Effelsberg telescope afterwards.

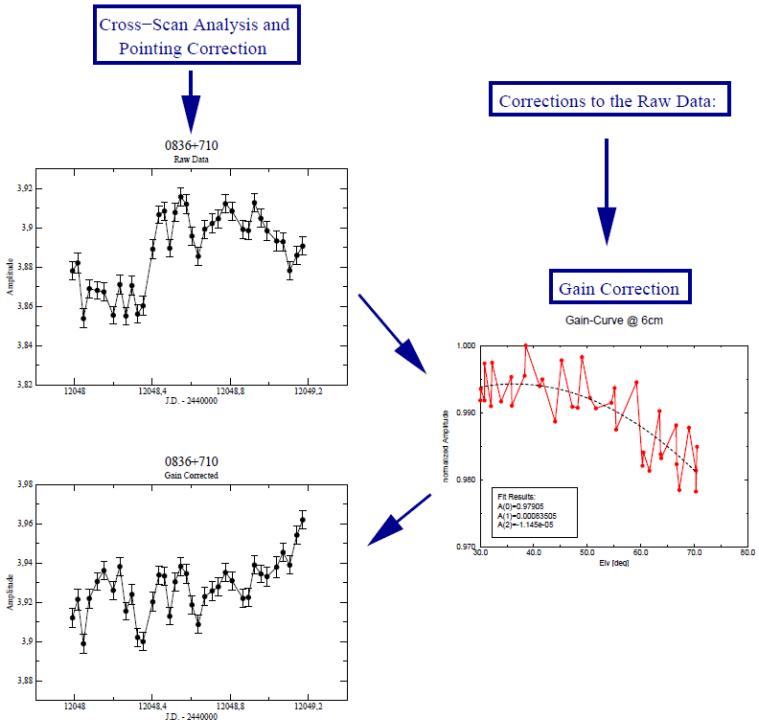

Figure 3.16: *Data reduction scheme (Fuhrmann, 2004)*

This is done by measuring the normalized amplitude of a reference source in dependence of the elevation. One can use a quadratic fit to the data:

$$G = A_0 + A_1 \cdot \mathrm{elv} + A_2 \cdot \mathrm{elv}^2$$

Not taking time dependent corrections into account, the reduction scheme looks like in Fig. 3.16.

3.5.7 Flagging

Especially for higher frequencies, which are more sensitive to changing weather, the measurements yield bad data. Fig. 3.17 shows a comparison between good and bad cross scans for PKS 2155−204. For the data reduction, one has to examine each Gaussian fit and each cross scan individually in order to extract the best scans for calculating the final flux value of one source at one time and wavelength.
The example in Fig. 3.17 is a quite bad one. There are many other cases, where it is less clear from the Gaussian fits, if the scan has to be deleted. One general example of a significant bad scan is bad *pointing*. If one drives a long way with the telescope, the antenna system needs some time to tare itself again. Therefore, as mentioned above, so called pointingscans are done before each normal scan in order to guarantee better measurements for the normal scan. That's why the pointingscans look quite bad, and are nearly all deleted afterwards. But also the "actual" scans can have pointing deviations. The current pointing is compared with the scan-average to

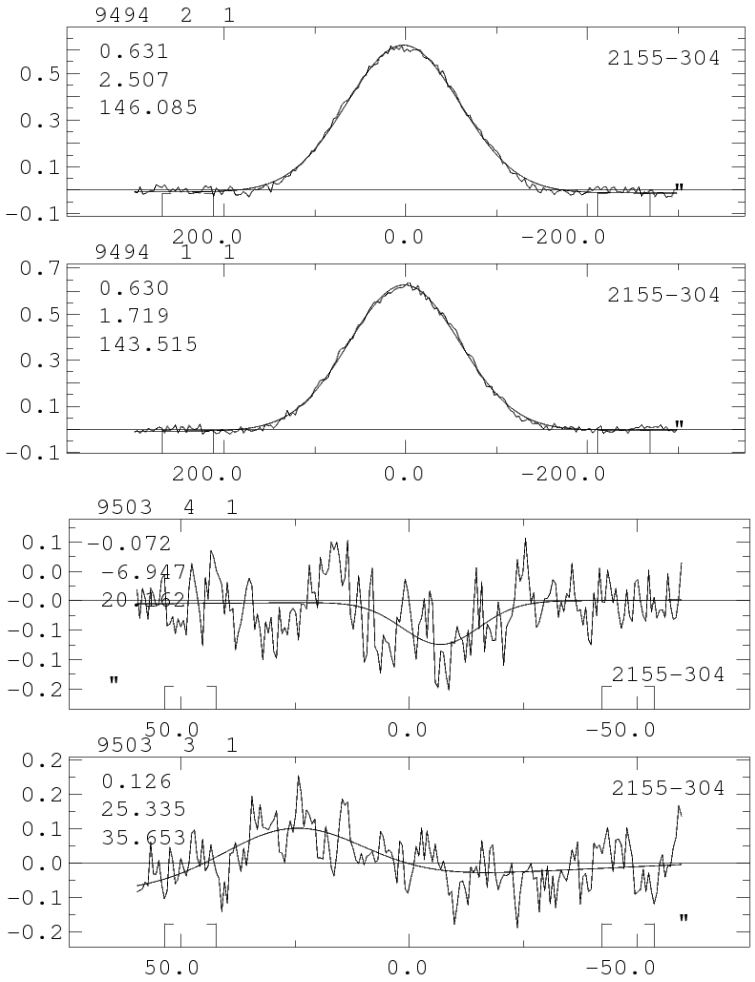

Figure 3.17: *Comparison of good (top) and bad (bottom) cross scans for PKS 2155−304*

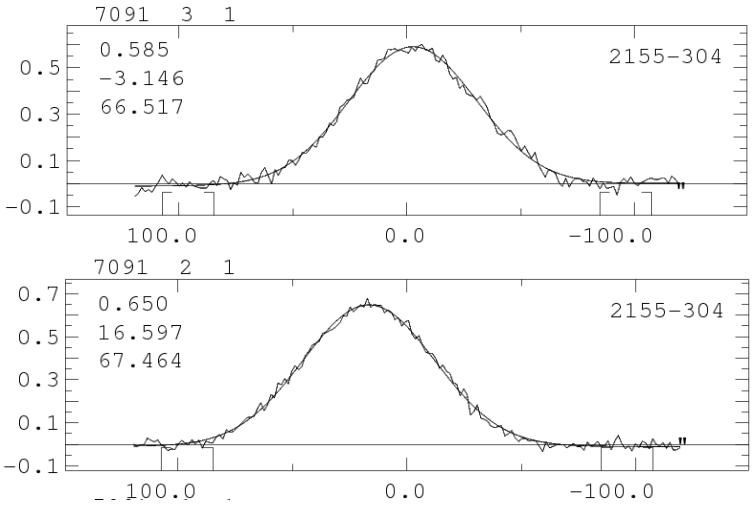

Figure 3.18: *Example for bad pointing in Effelsberg cross scans*

derive a measure for classifying the subscan as good or bad. The final flux error is composed of the error from the Gaussian fit, the pointing correction, the primary calibration factor from K to Jy, and at last the repeatibility. The latter one is a measure for the variability of the source. The error would be large, if it was clear that the source changes its flux heavily shortly after one measurement. But also the pointing correction introduces an error, which is larger for larger pointing deviations. This is shown in Fig. 3.18. Another example is the *HPBW* of the Gaussian, which is very important in assessing a subscan as acceptable or not. The long term mean-value from many scans represents a good estimate for the ideal Gaussian profile of one source at one frequency. Gaussians with high widths, however, tend to have too small amplitudes compared to the actual ones.
This already leads to the third problem, the *amplitudes*. As each source has its individual flux, one can not compare the measured flux with a long term average of all sources. If the amplitude of the subscans varies heavily within one scan, one has no clue how to recognize a good scan. The detected variability in amplitude is mostly not due to source variability, but to changing weather conditions. So, in opposite to bad pointing, varying amplitudes due to changing weather cannot be recalculated to the actual emitted flux value.
At last, the *elevation* has to be token into account. If the telescope is directed to sources near the horizon, the main, and especially the side lobes of the telecope's beaming pattern will catch up radio noise from ground. The threshold in the routines is 20°. However, one should have a look at the horizon, not to delete too much subscans. PKS 2155−304 has around 9 degrees in elevation and 180° in azimuth in average over all reduced epochs. Looking at the Effelsberg horizon (Fig. 3.19), one realizes that these coordinates lie exactly in one small valley. Therefore, the elevation is not a problem here. The routine `readCont` is doing the "flagging", which evaluates each scan due to its quality. The output is a so called `FITLPA`-file, which includes these flags that are indexed by small or capital letters. One excerpt from the `FITLPA` file for 9 mm is shown here:

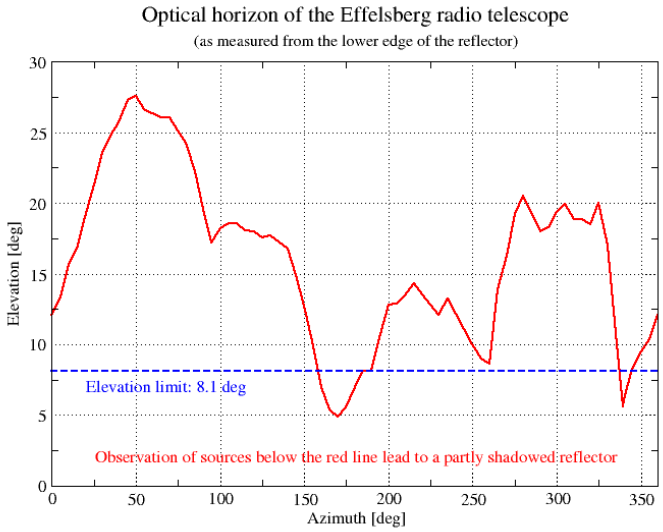

Figure 3.19: *Horizon around the 100m Effelsberg radio telescope*

Table 3.4: *Tolerances for the flagging routine*

amplitude	a	$\geq 10\%$ of the mean amplitude in one scan
	A	$\geq 20\%$
HPBW	h	$\geq 20\%$ of the mean amplitude in one scan
	H	$\geq 30\%$
elevation	E	< 20 deg and ≥ 85 deg
pointing	p	$\geq 10\%$ of the mean amplitude in all scans of one epoch
	P	$\geq 20\%$

```
581   1   1 2155-304      182.4   9.5 ELV  ...  EAP     1
581   2   1 2155-304      182.5   9.5 ELV  ...  E-P     2
581   3   1 2155-304      182.7   9.5 AZI  ...  EAPH    3
581   4   1 2155-304      182.8   9.5 AZI  ...  EAPh    4
```

The descriptions and thresholds of these flaggings are shown in Tab. 3.4. In this `FITLPA`-excerpt, one finds several useful informations. The flagging is denoted by a combination of some letters in the second last column. Additionally, the first column tells the scan number, the second one the subscan number, and the following the source name. As already mentioned, PKS 2155−304 has coordinates in azimuth and elevation of around 9° and 180°, respectively. Exact values are also found in the `FITLPA` excerpt. The abbreviations `ELV` and `AZI` tell, which subscan has been made in elevation, and which in azimuth. Several other entrys are just denoted by "...", for example the flux values, and so on.
This flagging-tool helps to decide, which subscans have to be deleted as early as all the above described reductional procedures are applied, and which not. Of course this also can be done automatically by an other routine. However, in order to save as much data as possile, I did the

deleting by hand.

4 Results

In this chapter I will present the results on analyzing several radio data, especially those from the 100 m Effelsberg radio telescope.

4.1 Radio Observations with HartRAO, ATCA, PKS, UMRAO, and the VLA

The first radio data to be analyzed were provided by M. Aller from the University of Michigan Radio Observatory (UMRAO) through private communication. These data provide a broad coverage in time from 1978 to 2010. As one can clearly see in the according lightcurves in Fig. 4.1, there is a maximum in all three frequencies. The flare in July 2006 is measured with good coverage. The UMRAO observations have been conducted with non-uniform time sampling, so different numbers of measurements were made per month. Therefore it is necessary to calculate the mean value for each month. Therefore I wrote a routine in `ISIS`, which fits a straight line through the flux values y_i of each month with respect to the individual errors σ_i. This is called a χ^2 minimisation. It would be wrong just to calculate the average with an error due to simple Gaussian error propagation, as these flux values are not expected to scatter Gaussian distributed around the average. If one assumes a function $y(x_i, a_1...a_n)$, one has to minimize

$$\chi^2 = \sum_{i=1}^{N} \left(\frac{y_i - y(x_i, a_1 \dots a_n)}{\sigma_i} \right)^2 \tag{4.1}$$

due to the functional parameters $a_1...a_n$. A straight horizontal line, however, can be described by just one parameter $y = a$. Therefore, the minimisation yields

$$a = \frac{\sum_i \frac{y_i}{\sigma_i^2}}{\sum_i \frac{1}{\sigma_i^2}}. \tag{4.2}$$

The uncertainties of the mean value are formed out of the errors of each individual value using the error propagation:

$$\delta a = \sqrt{\left(\frac{\partial a}{\partial y_1}\right)^2 (\delta y_1)^2 + \left(\frac{\partial a}{\partial y_2}\right)^2 (\delta y_2)^2 \left(\frac{\partial a}{\partial y_3}\right)^2 (\delta y_3)^2 + ...} \tag{4.3}$$

$$= \sqrt{\sum_i \delta y_i^2} = \sqrt{\sum_i \sigma_i^2} \tag{4.4}$$

The resulting flux values are plotted in Fig. 4.1. The maximum of the lightcurve lies at ≈ 1.3 Jy.

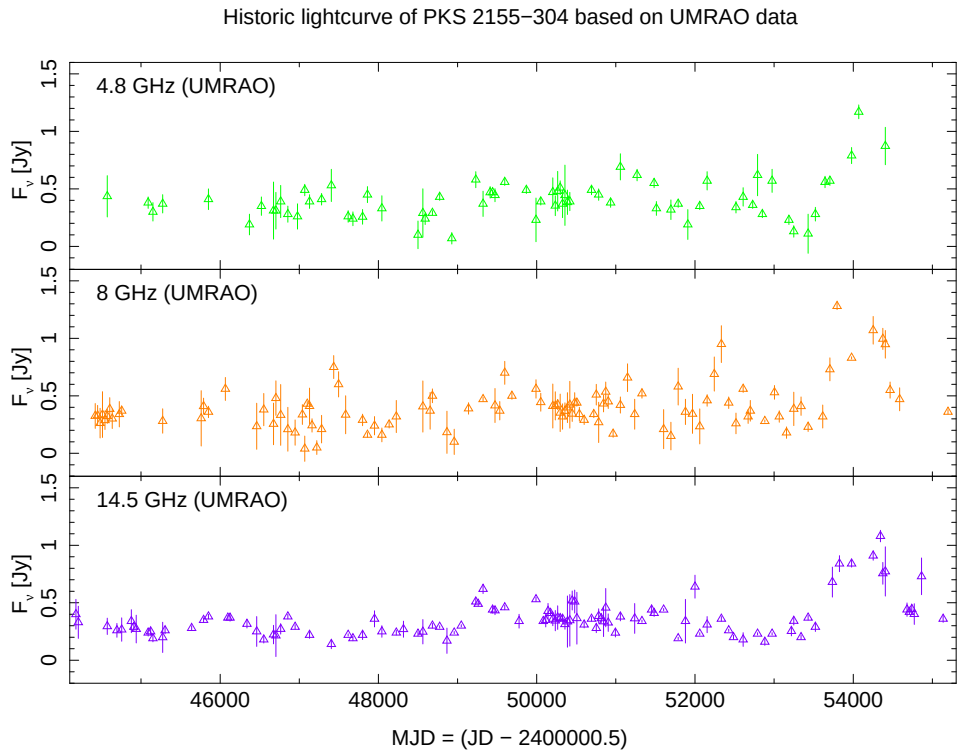

Figure 4.1: *Historic UMRAO lightcurve of PKS 2155−304 at 4.8, 8 and 14.5 GHz from November, 1979 to November, 2010 (data provided by M. Aller, private communication)*

This hostoric lightcurve also demonstrates the extremely variable behaviour of PKS 2155−304, as several maxima can be located before the actual flare in July 2006. Additionally, spectral indices between two adjacent frequencies were calculated (Fig. 4.2). These calculations again were made with a self written routine in `ISIS`, which simply does the following:
A radio spectrum basicly follows a powerlaw,

$$F_\nu \sim \nu^{-\alpha}. \tag{4.5}$$

With

$$F_1 = \nu_1^{-\alpha} \tag{4.6}$$
$$F_2 = \nu_2^{-\alpha} \tag{4.7}$$

one finds the spectral index α between two frequencies ν_1 and ν_2 for a given time to be

$$\alpha = -\frac{log(F_1) - log(F_2)}{log(\nu_1) - log(\nu_2)}. \tag{4.8}$$

Using Equ. 4.3, one finds for the error

$$\delta\alpha = \sqrt{\left(\frac{\partial\alpha}{\partial S_1}\right)^2 (\delta S_1)^2 + \left(\frac{\partial\alpha}{\partial S_2}\right)^2 (\delta S_2)^2}. \tag{4.9}$$

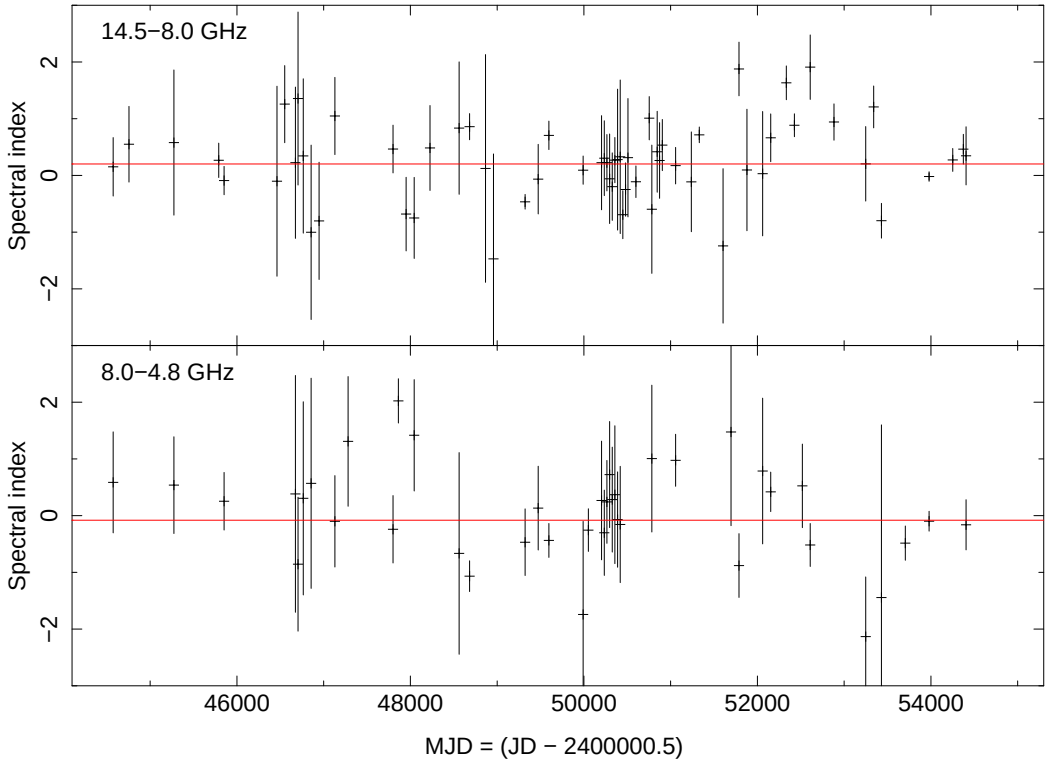

Figure 4.2: *Spectral indices between* 14.5 *and* 8 *GHz plus* 8 *and* 4.8 *GHz for the UMRAO lightcurves; the mean value is marked with a red line.*

These values are plotted in Fig. 4.2. There is no evidence for a flattening or steepening of the spectrum, as the spectral indices are just scattering around the mean value, which is again deriven from a χ^2 minimisation with the same routine used for the lightcurve. The reduced chi-squared

$$\chi^2_{\mathrm{red}} = \frac{\chi^2}{N - F}, \tag{4.10}$$

where N is the number of data points and F the number of free fitting parameters, tells something about the fit quality. $\chi^2 > 1$ means that the fit is not going through the data properly, $\chi^2 < 1$ that the errors or a scattering of the data are leading to an "over fitting" of the data. As the fit of a constant to the powerlawindices between 14.4 and 8.0 GHz leads to $\chi^2_{\mathrm{red}} \approx 0.45$, and between 8.0 and 4.8 GHz to $\chi^2_{\mathrm{red}} \approx 0.19$, the latter case is valid. Therefore, the scattering is not due to source variation, as the high errors permit a too perfect fit for even a horizontal line.
This will be highly improved with the Effelsberg data.

4.2 Radio Observations with the 100m Effelsberg Radio Telescope

In this section, the results of the data reduction from the spectral monitoring of PKS 2155−304 between 7 and 110 mm with the Effelsberg radio telescope are presented. The data reduction

itself is described in Sec. 3.5. As the data for shorter wavelengths than 20 mm were more affected by bad weather, only observations beginning at 13 mm yielded good results. Therefore, the lightcurves in Fig. 4.3 are more complete at wavelengths below. The measurements start in August, 2007 and end in November, 2009 covering the flare from its maximum to the decay. At the end of the data reduction, the dataset has to be further modified, as several times multiple observations were conducted per time. For these, the mean value has to be taken, following the χ^2-procedure. The inserted HartRAO (Hartebeesthoek Radio Astronomy Observatory, South Africa) data are showing good coverage with the Effelsberg data points. At 13 mm the data is interpolated using averaged adjacent values in time at 20 mm, as the lightcurves do not change much from 13 to 20 mm. The same interpolation is done at 36 mm. Using the same `ISIS`-script as for the UMRAO data, the spectral indices are calculated between two frequencies each (Fig. 4.4). Comparing the lightcurves and spectral indices of the UMRAO and Effelsberg data, it is obvious that the Effelsberg instrument is yielding better data due to the much larger collecting area. The spectral indices show a trend from a flat towards a steep spectrum. This can be best seen between $36 - 60$ mm and $60 - 110$ mm, as these wavelengths are less influenced by external factors like bad weather. Quite remarkable is that the two VLBI flux data points from TANAMI lie significantly below the Effelsberg lightcurve at 36 mm. This is due to the fact that the VLBI array is not sensitive to extended structures opposed to a single dish radio telescope. Using the interpolated flux values at 13 and 36 mm, one can calculate compactness ratios of the source with the TANAMI data points. Hence, for 13 mm one finds that $\approx 45 - 53\,\%$ between MJD 54551 and 54686, and for 36 mm, $\approx 30 - 24\,\%$ between MJD 54553 and 54686 of the flux detected by Effelsberg, can't be detected by the TANAMI VLBA. So, for lower frequencies and higher wavelengths, the compactness ratio decays. This is because the VLBA beam also gets wider for higher wavelengths, and one can thus image more large-scale structures with VLBI. This yields that the source, which has diameters of a few milliarcseconds, has to be surrounded by some radiating matter, which in turn is detected by the comparatively large beam size of the Effelsberg radio telescope. This beam width ranges from less than 1' for 13 mm to $\approx$ 15' for 36 mm. For comparison, the TANAMI array yields beam sizes of $0.5 - 1.0$ mas. As shown in Sec. 3.1, PKS 2155−304 is surrounded by four galaxies in a field of a few arcmin^2. These could be responsible for the high compactness ratio of this source.

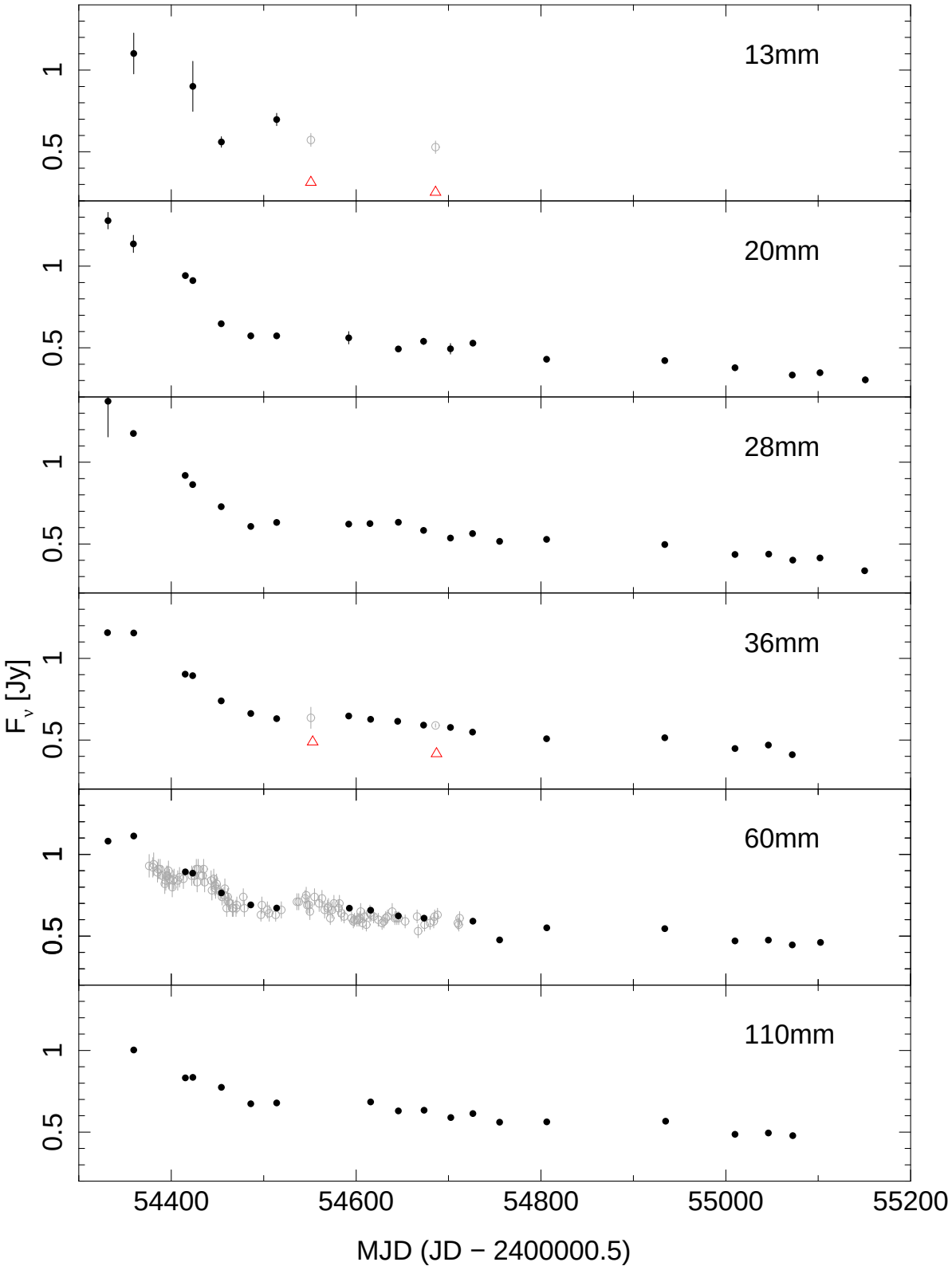

Figure 4.3: *Lightcurves for PKS 2155−394 based on data of the 100m Effelsberg radio telescope at* 13, 20, 28, 36, 60 *and* 110 *mm (filled circles) beginning in August 2007 and ending in November 2009, collected as part of the FGamma project; the red triangles mark flux data points from VLBI observations with TANAMI; at* 60 *mm, additionally data from HartRAO are included (grey circles); at* 13 *and* 36 *mm, the grey circles mark interpolated data points*

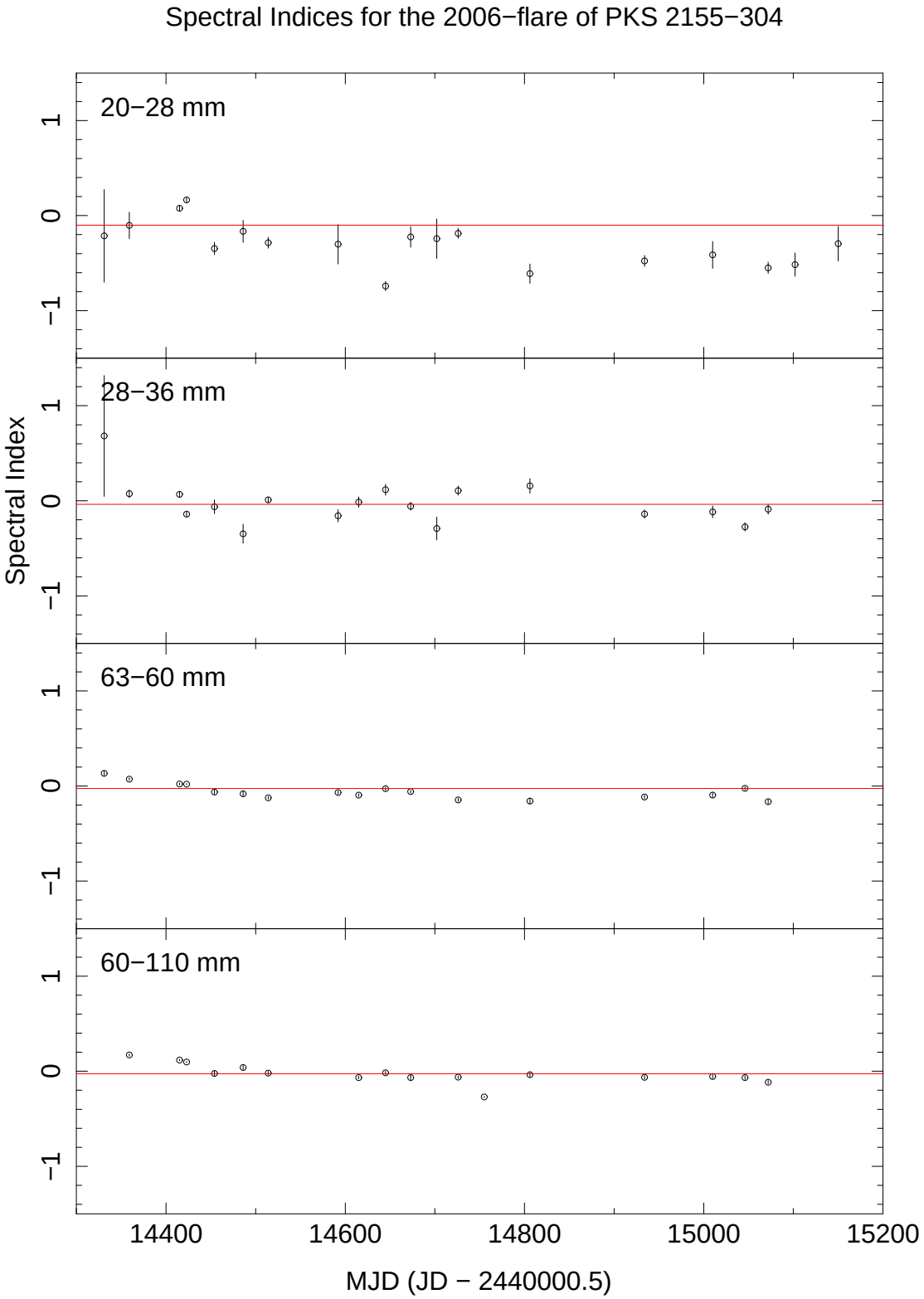

Figure 4.4: *Spectral indices between the lightcurves in Fig. 4.3; the red line corresponds to a χ^2-fit of a constant to the data*

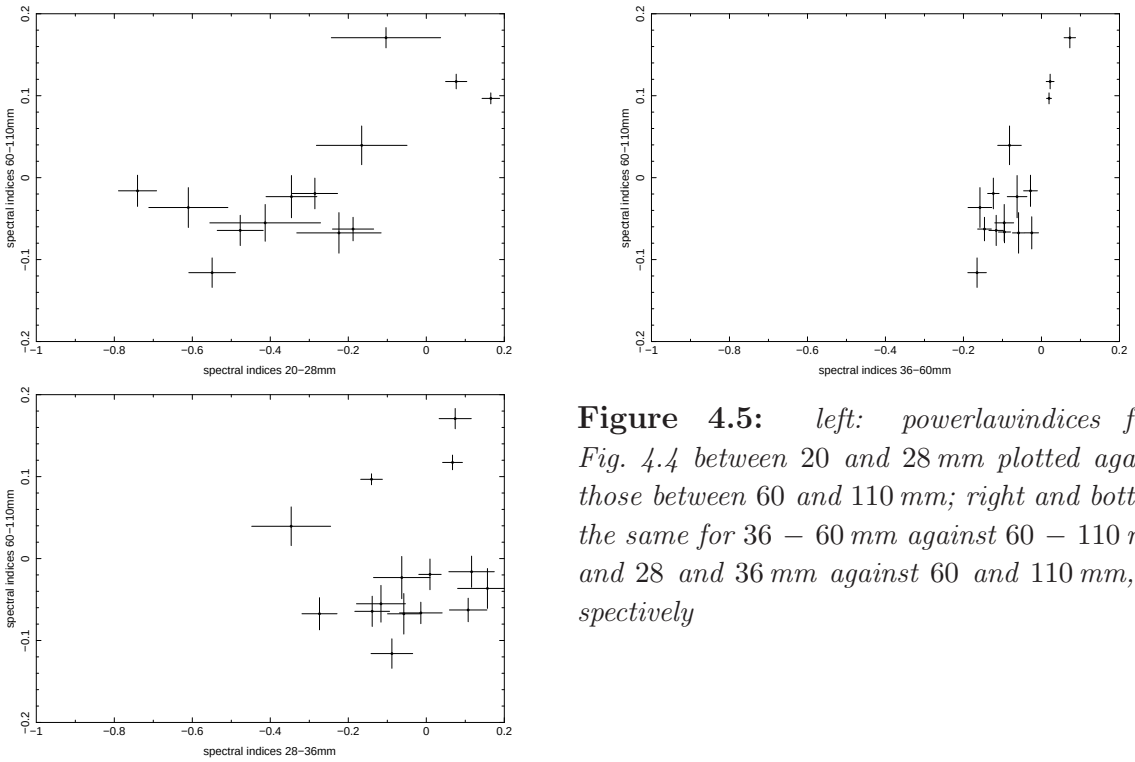

Figure 4.5: *left: powerlawindices from Fig. 4.4 between* 20 *and* 28 *mm plotted against those between* 60 *and* 110 *mm; right and bottom: the same for* 36 − 60 *mm against* 60 − 110 *mm, and* 28 *and* 36 *mm against* 60 *and* 110 *mm, respectively*

In Fig. 4.5, the powerlawindices from Fig. 4.4 are plotted against each other in three combinations. As the ranges are the same for all plots, they show how the calculated indices are distributed at which wavelengths. As the y-axis is the same in all three, one can compare the distributions on the x-axes. The spectral indices between 20 and 28 mm are scattering on a broader x-range, namely between ≈ -0.8 and ≈ 0.2, than those between 36 and 60 mm. This can also be read out from the plots in Fig. 4.4. Also considering the larger errors, this confirms, that the data at lower wavelengths is less precise. However, the error weighted average for $20 - 28$ mm gives some steeper spectra than the one for $36 - 60$ mm. The indices on the right side are concentrated at some higher value of ≈ -0.1. A few data points from the plateau stage of the flare are a little above zero. Considering the indices between 60 and 110 mm, also a concentration at negative values is identifiable. Compared to the information of time in Fig. 4.4, the spectra are quickly steepening in both cases. This makes sense, as the measurements start already at the beginning of the decay stage of the flare. These findings are less significant in the bottom plot for a combination of $28 - 36$ mm and $60 - 110$ mm. Whilst the y-axis is the same again, the scattering around a negative index is less obvious for the data between 28 and 36 mm than in the other cases.

One can also see the steepening with time in the whole frequency spectra. In Fig. 4.6 to Fig. 4.8 several F_ν-spectra are shown from the flare maximum to the decaying stage of the flare. Here, the steepening that did already come out from the spectral indices, which tend towards negative values, can directly be observed with proceeding time. The steepening in the F_ν-spectra gets visible as a flattening in the νF_ν-spectra (Fig. 4.9 to Fig. 4.11). In addition, the overall flux decreases with time in all shown spectra for the decaying shock. These findings are supported by the generalized shock model of Valtaoja et al. (1992), which builds up on the model of Marscher & Gear (1985).

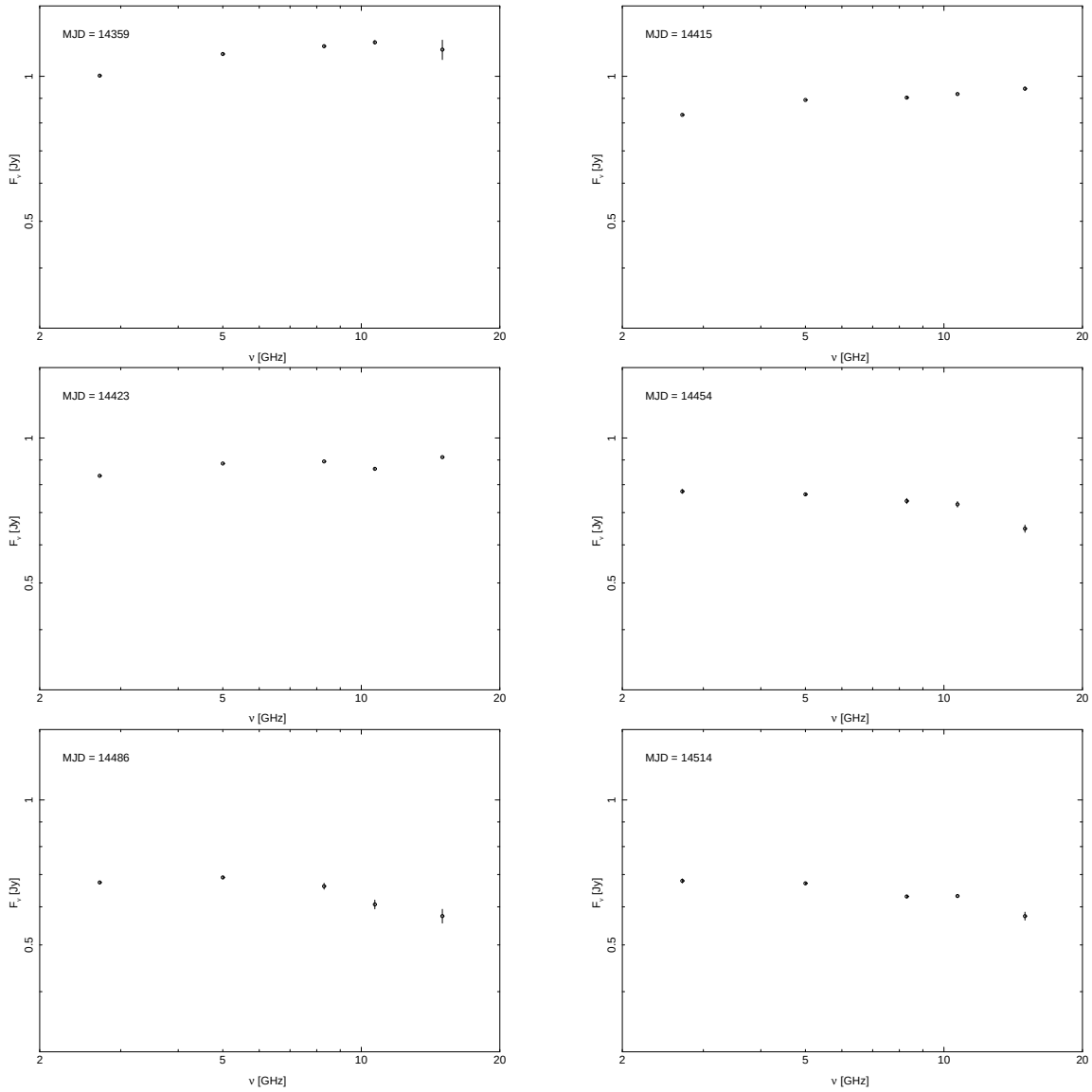

Figure 4.6: *Effelsberg spectra from MJD 14359 to 15072*

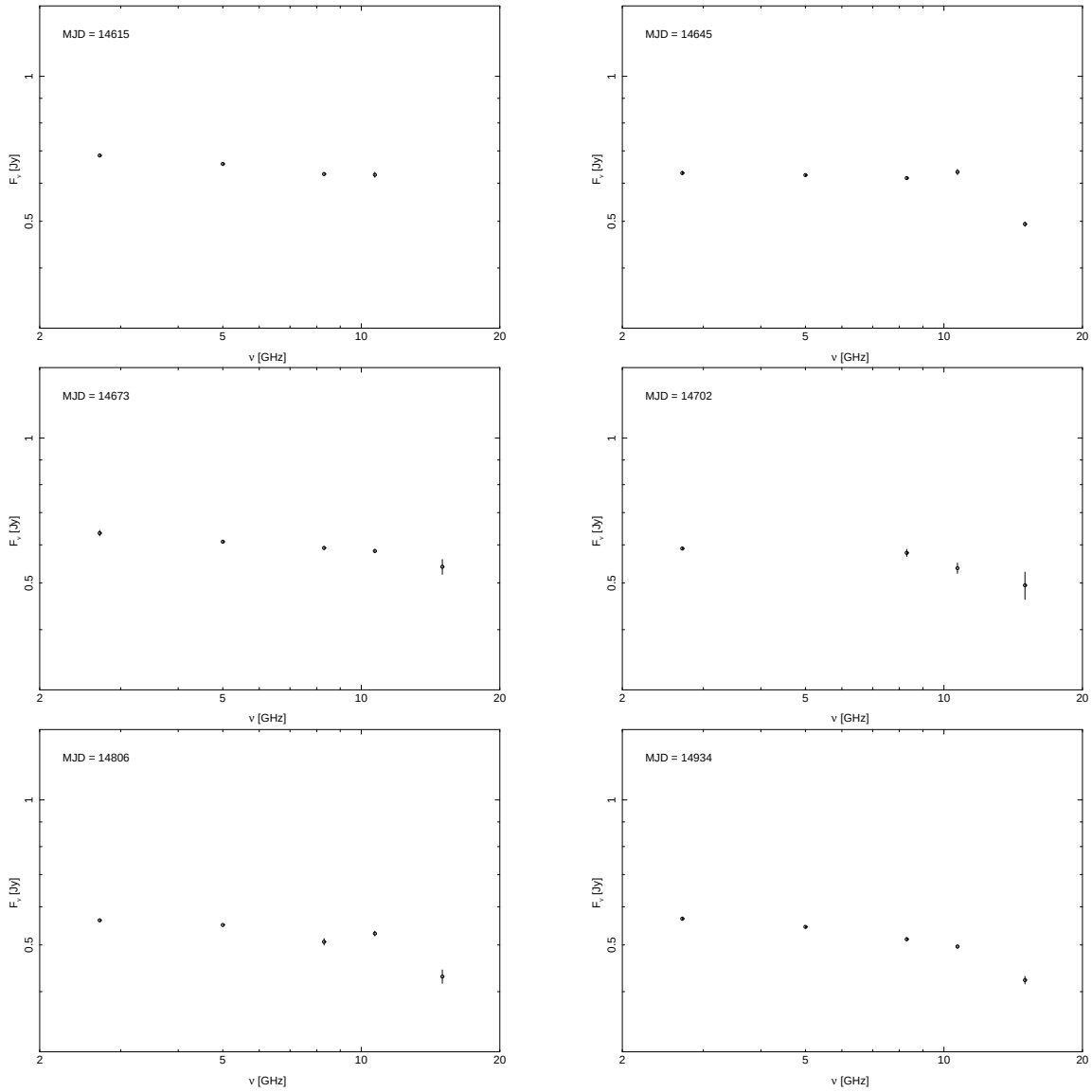

Figure 4.7: *Effelsberg spectra from MJD 14359 to 15072*

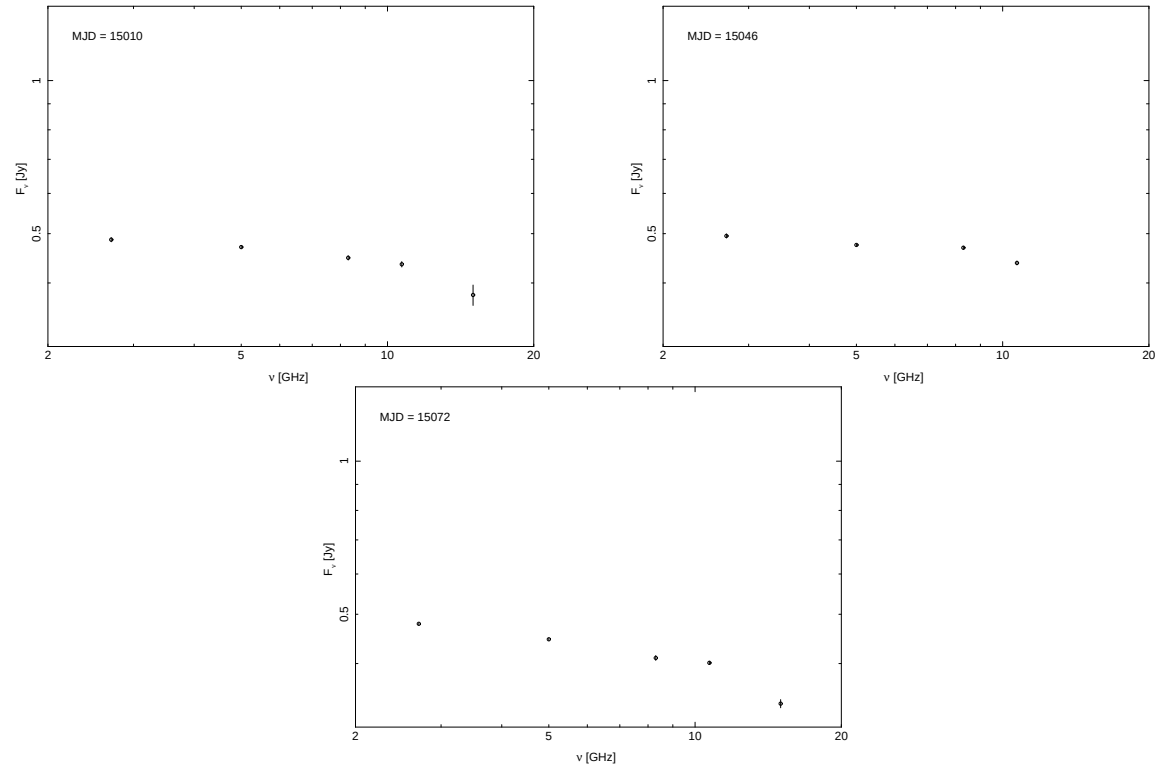

Figure 4.8: *Effelsberg spectra from MJD 14359 to 15072*

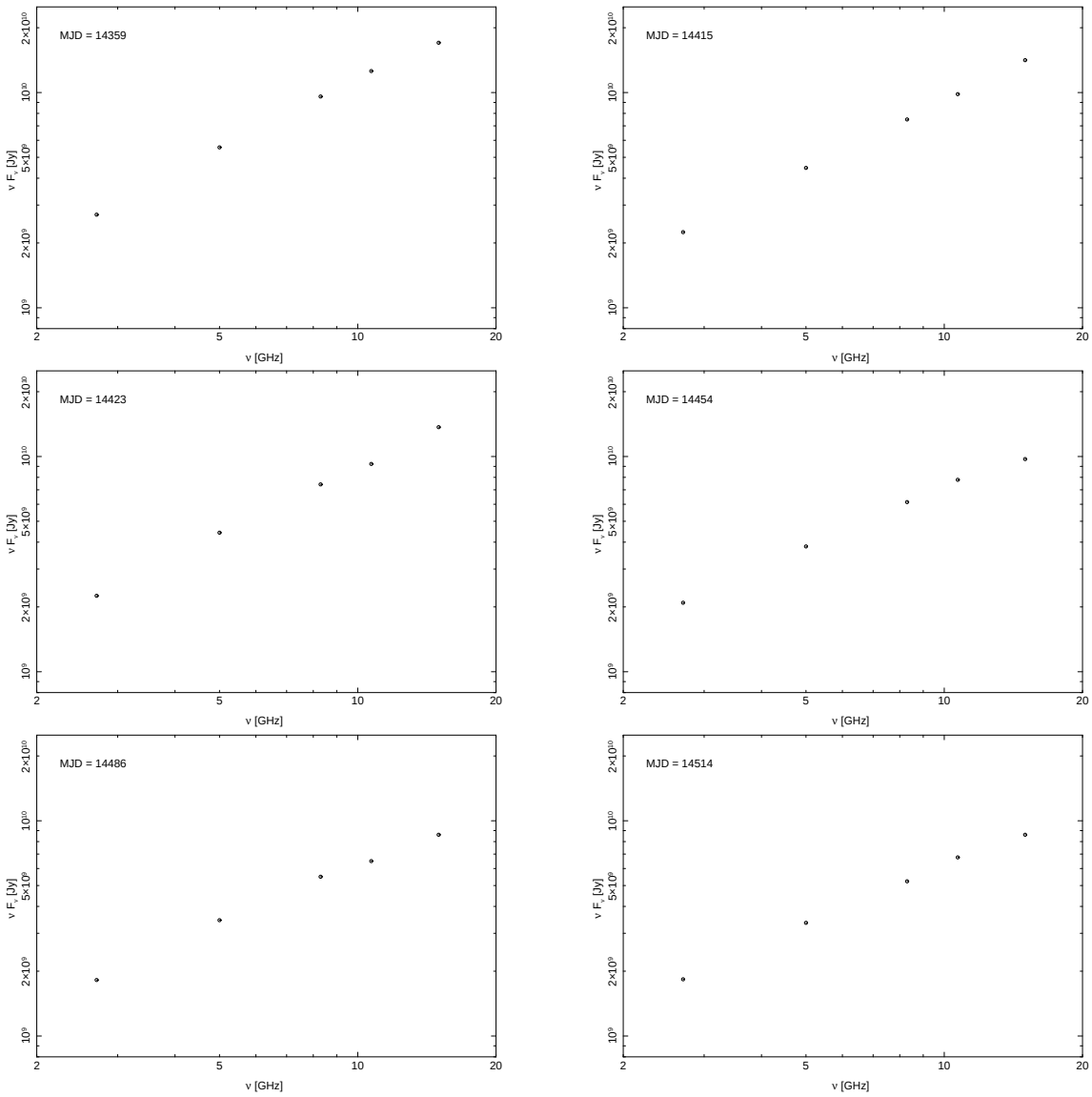

Figure 4.9: *Effelsberg spectra (νF_ν) from MJD 14359 to 15072*

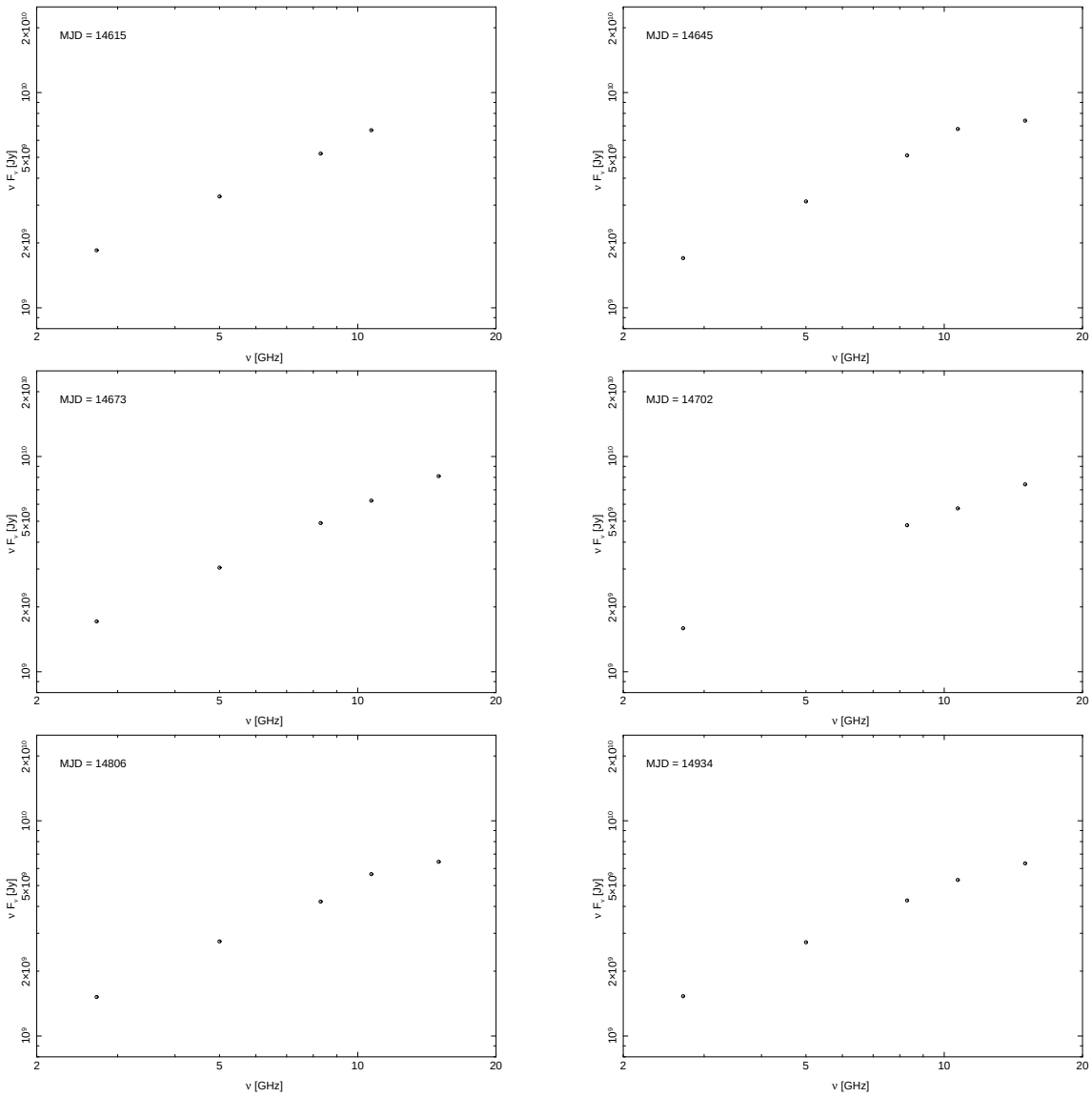

Figure 4.10: *Effelsberg spectra (νF_ν) from MJD 14359 to 15072*

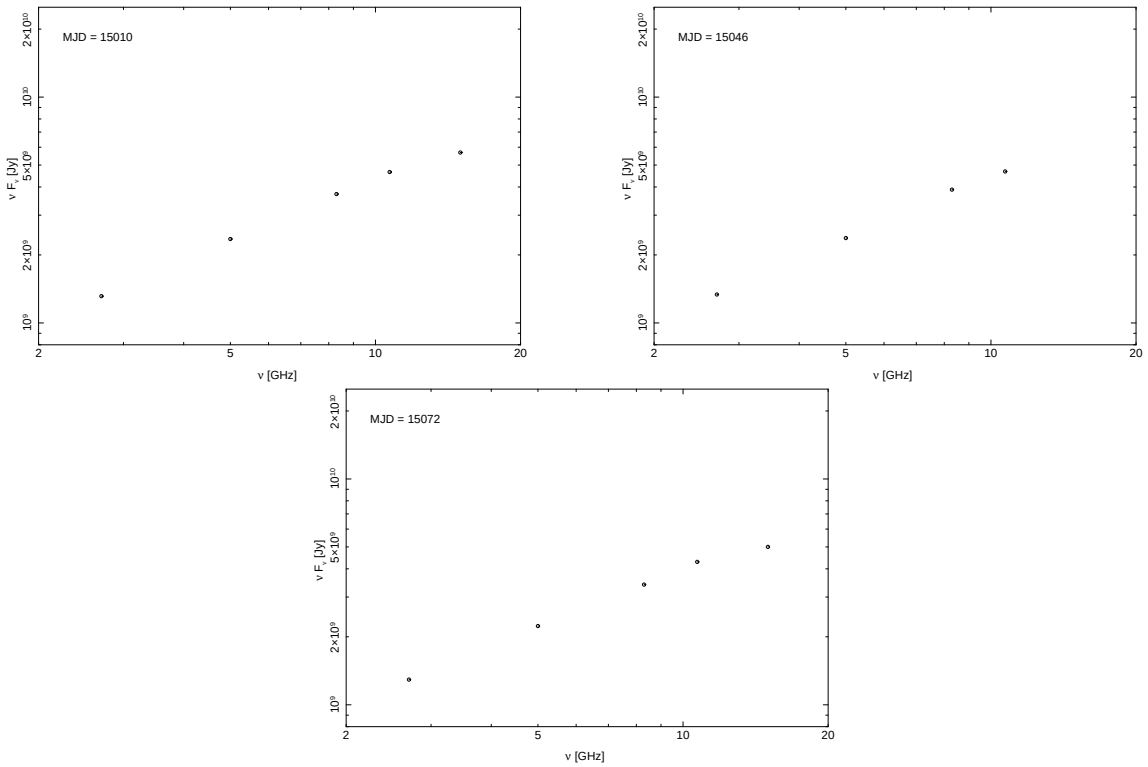

Figure 4.11: *Effelsberg spectra (νF_ν) from MJD 14359 to 15072*

The available HartRAO data, whose decaying part is also plotted in the Effelsberg lightcurve at 36 mm (Fig. 4.3), is shown in two lightcurves at 350 mm and 60 mm, respectively in Fig. 4.12. The data is fitting very good with the available Effelsberg data at 60 mm, as one can see in Fig. 4.3. Unfortunately the maximum of the flare was not observed with HartRAO, although it could be interpolated to some value above 1 Jy.
Finally one can say that the behaviour of the Effelsberg data finds good explanations in the currently well established jet models. It would be more difficult to make this statement with the available UMRAO and HartRAO data just because of the larger errors and the overall scattering of the data. However, the UMRAO lightcurves are essential for an overview on the historic behaviour of PKS 2155−304 before the Effelsberg measurements, which indicates its overall heavy variability. Although the HartRAO data did not cover the flare maximum, they are very helpful in confirming the Effelsberg data, as both well coincide at 60 mm.
In future work, I will perform discrete cross-correlation calculations between the Effelsberg lightcurves in order to yield information about the time shifts between the curves at the available frequencies. This shall give further arguments for the treated shock models by hopefully finding the flare to occur at higher frequencies first.

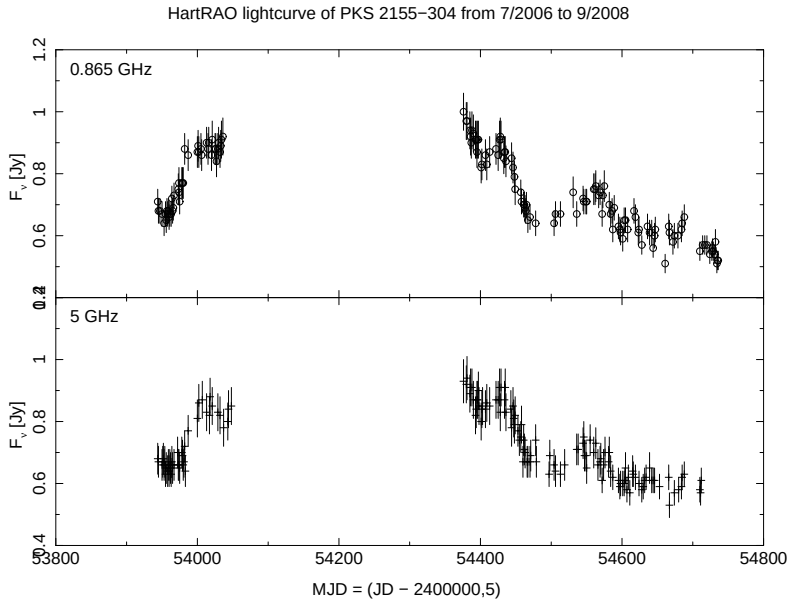

Figure 4.12: *HartRAO lightcurve of PKS 2155−304 at 6 cm (5 GHz) and 35 cm (0.865 GHz); data provided by Andreas Zech*

Bibliography

Technical Characteristics of the Effelsberg 100-m Radio Telescope http://www.mpifr.de/div/effelsberg/antenna/antenna_spec.html

Aharonian F., Akhperjanian A.G., Anton G., et al., 2009, Astronomy and Astrophysics 502, 749

Angelakis E., 2007, Ph.D. thesis, Mathematisch-Naturwissenschaftlichen Fakultaet der Rheinischen Friedrich-Wilhelms-Universitaet Bonn

Angelakis E., Fuhrmann L., Marchili N., et al., 2008, Memorie della Societa Astronomica Italiana 79, 1042

Bai J.M., Lee M.G., 2001, The Astrophysical Journal 558, L19

Blandford R.D., Konigl A., 1979, The Astrophysical Journal 232, 34

Bridle A.H., Hough D.H., Lonsdale C.J., et al., 1994, The Astrophysical Journal 108, 766

Brinkmann W., Maraschi L., Treves A., et al., 1994, Astronomy and Astrophysics 288, 433

Burke B.F., Graham-Smith F., 2009, An Introduction to Radio Astronomy, Cambridge University Press, Cambridge, United Kingdom

Courvoisier T., Blecha A., Bouchet P., et al., 1995, The Astrophysical Journal 438, 108

Curtis H.D., 1918, Publications of Lick Observatory 13, 9

Demtroeder W., 2005, Experimentalphysik 3, Atome, Molekuele und Festkoerper, Springer, Berlin, Heidelberg, New York

Donato D., Ghisellini G., Tagliaferri G., Fossati G., 2001, Astronomy and Astrophysics 375, 739

Edelson R., Krolik J., Madejski G., et al., 1995, The Astrophysical Journal 438, 120

Falcke D.H., , Physics of AGN, article, Max Planck Institute for Radio Astronomy, Bonn

Falomo R., Pesce J.E., Treves A., 1993, The Astrophysical Journal 411, L63

Filippenko A.V., 1993, http://nedwww.ipac.caltech.edu/level5/Cambridge/Cambridge1_1.html

Fossati G., Maraschi L., Celotti A., et al., 1998, Monthly Notices of the Royal Astronomical Society 299, 433

Fuhrmann L., 2004, Ph.D. thesis, Mathematisch-Naturwissenschaftlichen Fakultaet der Rheinischen Friedrich-Wilhelms-Universitaet Bonn

García-Lorenzo B., Mediavilla E., Arribas S., 1999, The Astrophysical Journal 518, 190

Garofalo D., 2009, The Astrophysical Journal 699, 400

George I.M., Fabian A.C., 1991, Monthly Notices of the Royal Astronomical Society 249, 352

Giroletti M., Reimer A., Fuhrmann L., et al., 2010, ArXiv e-prints

Goodrich R.W., 1995, The Astrophysical Journal 440, 141

Gordon K.D., Bailin J., Engelbracht C.W., et al., 2006, The Astrophysical Journal 638, L87

Guetta D., 2002, In: I. Cagnoni (ed.) Inflows, Outflows, and Reprocessing around Black Holes., p.137

Hovatta T., Nieppola E., Tornikoski M., et al., 2008, Astronomy and Astrophysics 485, 51

Kadler M., Ros E., Perucho M., et al., 2008, The Astrophysical Journal 680, 867

Kembhavi A.K., Narlika Jayant V., 1999, Quasars and Active Galactic Nuclei, Cambridge University Press, Cambridge, United Kingdom

King A.R., Lubow S.H., Ogilvie G.I., Pringle J.E., 2005, Monthly Notices of the Royal Astronomical Society 363, 49

Korista K.T., 1993, `http://nedwww.ipac.caltech.edu/level5/Cambridge/Cambridge1_1.html`

Krolik J.H., 1999, Active Galactic Nuclei, Princeton University Press, Princeton, New Jersey, USA

Leahy J.P., 2003, `http://www.jb.man.ac.uk/ATLAS`

Marscher A.P., 1996, In: P. E. Hardee, A. H. Bridle, & J. A. Zensus (ed.) Energy Transport in Radio Galaxies and Quasars, Vol. 100. Astronomical Society of the Pacific Conference Series, p.45

Marscher A.P., 2006a, In: P. A. Hughes & J. N. Bregman (ed.) Relativistic Jets: The Common Physics of AGN, Microquasars, and Gamma-Ray Bursts, Vol. 856. American Institute of Physics Conference Series, p.1

Marscher A.P., 2006b, Astronomische Nachrichten 327, 217

Marscher A.P., Gear W.K., 1985, The Astrophysical Journal 298, 114

Marscher A.P., Jorstad S.G., Gómez J., et al., 2002, Nature 417, 625

Mushotzky R.F., Done C., Pounds K.A., 1993, Annual review of astronomy and astrophysics 31, 717

Ojha R., Kadler M., Böck M., et al., 2010, ArXiv e-prints

Padmanabhan T., 2002, Theoretical Astrophysics, Volume 3, Galaxies and Comoslogy, Cambridge University Press, Cambridge, United Kingdom

Pankratov O., 2008, Theoretische Physik, Elektrodynamik, Lecture WT 2008/2009 University Erlangen-Nürnberg

Peschel U., 2009, Experimentalphysik: Optik, Lecture WT 2008/2009 University Erlangen-Nürnberg

Peterson B.M., 2009, An Introduction to Active Galactic Nuclei, Cambridge University Press, Cambridge, United Kingdom

Przybilla N., Drechsel H., 2009, Sternatmosphären und Strahlungsphänomene, Lecture WT 2009/2010 University Erlangen-Nürnberg

Pushkarev A.B., Kovalev Y.Y., Lister M.L., 2010, ArXiv e-prints

Reynolds C.S., Garofalo D., Begelman M.C., 2006, The Astrophysical Journal 651, 1023

Robson I., 1996, Active Galactic Nuclei, Wiley, Chichester, England

Rybicki G.B., 2004, Radiative Processes in Astrophysics, Wiley-Vch, Weinheim

Schneider P., 2007, Einführung in die Extragalaktische Astronomie und Kosmologie, Springer, Berlin, Germany

Seyfert C.K., 1943, The Astrophysical Journal 97, 28

Türler M., Paltani S., Courvoisier T., et al., 1999, Astronomy and Astrophysics Supplement 134, 89

Urry C.M., Maraschi L., Edelson R., et al., 1993, The Astrophysical Journal 411, 614

Valtaoja E., Teräsranta H., 1996, Astronomy and Astrophysics Supplement 120, C491+

Valtaoja E., Terasranta H., Urpo S., et al., 1992, Astronomy and Astrophysics 254, 71

Weidinger M., Spanier F., 2010, International Journal of Modern Physics D 19, 887

Wilms J., Kadler M., 2010, Active Galactic Nuclei, Lecture ST 2010 University Erlangen-Nürnberg

Woltjer L., 1959, The Astrophysical Journal 130, 38

Acknowledgement

I would like to thank everybody, who gave me support for this thesis in the last month. In particular I give many thanks to

- the VLBI group at the Max Planck Institute of Radio Astronomy in Bonn, especially J.A. Zensus, for the opportunity to learn the Effelsberg data reduction, and to visit the Effelsberg radio telescope, L. Fuhrmann, my supervisor at the institute, who donated much of his time for me, E. Angelakis, who also was a great help in questions belonging the data reduction and offering me a participation in the Single Dish Summer School, and I. Nestoras for further remote-support concerning the data and their reduction. Thanks to all of them for having found a way to provide the data remotely.
- my supervisors M. Kadler and J. Wilms at the Dr. Remeis Observatory, Bamberg for spending much time in giving intellectual and mental support as well as giving me the opportunity for an employment at the observatory as a student assistant
- M. Aller for providing the UMRAO data, through private communication
- A. Zech for providing the HartRAO data, also through private communication
- Ch. Stegmann for his assistance in understanding some details belonging the recent H.E.S.S. publication about the flare of PKS 2155-304 in July 2006
- all "Remeisens" at the Dr. Remeis observatory for offering me a friendly and sincere shelter and for pointing out several locations in Bamberg to eat the best "Schäufele" and drink the best beer. Also great thanks to the `ISIS`-specialists and trouble-shooters M. Böck, M. Hanke, F. Fürst and T. Dauser, the cross-correlation specialist C. Grossberger, the Latex expert F. Fürst and C. Müller for explanations regarding the VLBI techniques
- M. Obst, N. Hell and others for their (nightly) companionship in the office, the nice chats and the good pizza
- my fellows for at least trying to teach me "Schafkopfen" and for the companionship in Erlangen's pubs
- my father for his far-reaching support and my deceased mother still believing in me
- everone, I unfortunately forgot to mention, as the thesis hat to be printed right now

Erklärung

Hiermit erkläre ich, diese Bachelorarbeit in Eigenarbeit angefertigt zu haben, sofern nicht explizit in Text oder Referenzen vermerkt. Diese Arbeit ist der Universität Erlangen-Nürnberg als Vorraussetzung für den Erhalt des Abschlusses "Bachelor of Science" vorgelegt worden. Ich erkläre, dass diese Arbeit weder partiell noch als Ganzes für den Erhalt eines anderweitigen Abschlusses verwendet wurde und wird.

Erlangen, den 30.07.2010

Tobias Beuchert